



Chair of Ferrous Metallurgy

Master's Thesis



Experimental investigation and
thermodynamic assessment of the ternary
system Fe-Mn-S

Robert Littringer, BSc

February 2024



AFFIDAVIT

I declare on oath that I wrote this thesis independently, did not use any sources and aids other than those specified, have fully and truthfully reported the use of generative methods and models of artificial intelligence, and did not otherwise use any other unauthorized aids.

I declare that I have read, understood and complied with the "Good Scientific Practice" of the Montanuniversität Leoben.

Furthermore, I declare that the electronic and printed versions of the submitted thesis are identical in form and content.

Date 02.02.2024

A handwritten signature in black ink, reading 'Robert Littringer'.

Signature Author
Robert Littringer

Acknowledgement

The author gratefully acknowledges financial support within the framework of the COMET program in the K2 Center "Integrated Computational Material, Process and Product Engineering (IC-MPPE)" (project number 886385). This program is funded by the Austrian Federal Ministries for Climate Protection, Environment, Energy, Mobility, Innovation and Technology (BMK) and for Digitalization and Business Location (BMDW), represented by the Austrian Research Promotion Agency (FFG), and the provinces of Styria, Upper Austria and Tyrol.



Many thanks belong to my supervisors **Assoc.-Prof. Dipl.-Ing. Dr.mont. Christian Bernhard, Dipl.-Ing. Dr.mont. Peter Presoly** and **Dipl.-Ing. Dr.mont. Michael Bernhard** for their intensive scientific support during the writing of this thesis. Without their support, motivation and guidance, this work would not have been possible.

My sincerest gratitude belongs to **Prof. Dr. Youn-Bae Kang** for his scientific guidance within this work and for hosting me at the Clean Steel Laboratory at the Pohang University of Science and Technology, Republic of Korea. Furthermore, I would like to express many thanks to **Dipl.-Ing. Dr.mont Michael Bernhard, Won-Bum Park, MSc** and **all members** of the Clean Steel Laboratory for the warm welcome in their team and the truly unforgettable time in Korea.

I would also like to thank **Michael Lammer** and **Ing. Bernd Lederhaas** for their support in the practical part of this work.

Many thanks to my partner **Nadine Plank**, who supported and motivated me in every situation, not only during my studies but also during my time in Korea.

The biggest gratitude belongs to my parents, **Franz and Renate Littringer**. Without their unconditional support, my studies would not have been possible in this form.

Abstract

In modern steelmaking, manganese (Mn) is known as a versatile alloying element for various steel grades. Typical amounts of Mn are up to 1.5 wt.-% in low-alloyed carbon steels, around 3 to 6 wt.-% in medium Mn steels and more than 10 wt.-% in high Mn steels for special purposes. Mn increases strength and enhances toughness, ductility and weldability of steels in certain alloying ranges. In addition, Mn serves the purpose of binding residual sulfur (S) as manganese sulfides (Mn,Fe)S. In contrary, S is in general considered to be harmful in steel. S segregates in interdendritic liquid during the solidification of steel and causes hot tearing. In combination with Mn, sulfur leads to the formation of (Mn,Fe)S during the solidification in the continuous casting process, which is favorable to avoid the hot tear sensitivity. However, in the solid state, the precipitation of (Mn,Fe)S drastically decreases the ductility at elevated temperatures and thereby may induce crack formation at the surface. To assess the quality-related issues, the precise knowledge on thermodynamics of the Fe-Mn-S system and the prediction of (Mn,Fe)S stability in steel is crucial.

The aim of this master's thesis was the experimental investigation and thermodynamic assessment of the ternary system Fe-Mn-S with emphasis on solidification of steel. Alloys with 0.5 wt.-% and 2 wt.-% Mn and up to 0.3 wt.-% S were investigated by Differential Scanning Calorimetry (DSC) regarding high-temperature phase equilibria and (Mn,Fe)S precipitation during cooling. Based on these results and experimental data from literature, thermodynamic modeling according to the CALPHAD (CALculation of PHase Diagrams) approach was carried out in the sub-systems Fe-Mn, Fe-Mn-C and Fe-Mn-S to create a database for the quaternary system Fe-Mn-S-C. For the liquid phase the Modified Quasichemical Model (MQM) in the pair-approximation was applied to formulate the solution's Gibbs energy. The MQM enabled to consider strong short-range-ordering (SRO) in the melt, which is typical for S-containing metal

systems. The Compound Energy Formalism (CEF) was used for the descriptions of the solid solutions, e.g. austenite, ferrite, and various carbides. Several compounds were treated as stoichiometric to simplify the thermodynamic database.

Kurzfassung

In der modernen Stahlerzeugung ist Mangan (Mn) als vielseitiges Legierungselement für verschiedene Stahlsorten bekannt. Typische Mn-Gehalte sind bis zu 1,5 wt.-% in niedrig legierten Kohlenstoffstählen, circa 3 bis 6 wt.-% in Medium-Mn Stählen und mehr als 10 wt.-% in Hoch-Mn Stählen für Sonderanwendungen. Mn erhöht die Festigkeit und verbessert die Zähigkeit, Duktilität und Schweißbarkeit in bestimmten Legierungsbereichen. Darüber hinaus dient Mn dazu, Restschwefel (S) in Form von Mangansulfiden (Mn,Fe)S abzubinden. Im Gegensatz zu Mn wird S im Allgemeinen als Stahlschädling angesehen. S scheidet sich während der Erstarrung in der interdendritischen Restschmelze aus und verursacht Heißrisse. In Kombination mit Mn führt Schwefel während der Erstarrung beim Stranggießen zur Bildung von (Mn,Fe)S, was die Gefahr für Heißrisse vermindern kann. Im erstarrten Produkt führen (Mn,Fe)S jedoch zur drastischen Verringerung der Duktilität bei höheren Temperaturen und begünstigen dadurch Rissbildung an der Oberfläche. Um qualitätsrelevante Probleme zu beurteilen, ist die genaue Kenntnis der Thermodynamik des Fe-Mn-S Systems und die Vorhersage der (Mn,Fe)S-Stabilität im Stahl entscheidend.

Das Ziel dieser Masterarbeit war die experimentelle Untersuchung und thermodynamische Beschreibung des ternären Systems Fe-Mn-S mit Schwerpunkt auf der Erstarrung von Stahl. Legierungen mit 0,5 wt.-% und 2 wt.-% Mn und bis zu 0,3 wt.-% S wurden mittels Differential Scanning Calorimetry (DSC) auf Hochtemperatur-Phasengleichgewichte und (Mn,Fe)S-Ausscheidungen beim Abkühlen untersucht. Auf der Grundlage dieser Ergebnisse und experimenteller Daten aus der Literatur wurde eine thermodynamische Modellierung nach der CALPHAD-Methodik (CALculation of PHase Diagrams) in den Teilsystemen Fe-Mn, Fe-Mn-C und Fe-Mn-S durchgeführt, um eine Datenbank für das quaternäre System Fe-Mn-S-C zu schaffen. Für die Flüssigphase wurde das Modified Quasichemical Model (MQM) in der Pair-

Approximation verwendet, um die Gibbs-Energie Schmelze zu formulieren. Das MQM ermöglichte es, das für S-haltige flüssige Metallsysteme typische Short Range Ordering (SRO) zu berücksichtigen. Der Compound Energy Formalism (CEF) wurde für die Beschreibung der Festphasen, wie zum Beispiel Austenit, Ferrit und Karbide, verwendet. Einige Verbindungen wurden als stöchiometrische Verbindungen angenommen, um die Modellierung zu vereinfachen.

Table of contents

Acknowledgement	II
Abstract	IV
Kurzfassung	VI
Table of contents	VIII
List of figures	X
List of tables	XV
Acronyms	XVII
1 Introduction	1
2 Literature review	3
2.1 Influence of S and (Mn,Fe)S in continuous casting	3
2.2 Experimental studies	8
2.3 Thermodynamic assessments of the Fe-Mn, Fe-Mn-C and Fe-Mn-S systems	12
3 Experimental investigation of the ternary system Fe-Mn-S	14
3.1 Sample preparation and chemical analysis	14
3.2 Differential Scanning Calorimetry (DSC).....	18
3.3 Thermo-optical analysis (TOA)	22
4 Thermodynamic modeling	24
4.1 Liquid phase	27
4.2 Solid solutions	29
4.3 Pure elements and stoichiometric compounds.....	32

5	Results and discussion	33
5.1	Experimental investigation of high temperature phase equilibria.....	33
5.2	Optimizations in the systems Fe-Mn, Fe-Mn-C and Fe-Mn-S.....	38
5.2.1	The binary system Fe-Mn and the ternary system Fe-Mn-C.....	39
5.2.2	The ternary system Fe-Mn-S.....	46
5.3	Derivation of an analytical equilibrium constant for MnS precipitation in liquid and solid phases.....	53
6	Conclusion	57
	Bibliography	61
A	Appendix	A
A.1	Chemical analysis of the sample material	B
A.2	Model parameters.....	C

List of figures

Figure 2-1: Influence of tramp and alloying elements on the activity of S in liquid Fe. [9].....	4
Figure 2-2: Binary Fe-S phase diagram calculated with thermodynamic description of Waldner and Pelton [6]. Calculation performed with FactSage 8.2 [10].....	4
Figure 2-3: Reduced hot ductility related to precipitations in steels. [14]–[16]	6
Figure 2-4: Different types of (Mn,Fe)S inclusions. a) type I b) type II c) type III and d) type X. [19].....	7
Figure 2-5: a) Number and b) volume fraction of sulfide inclusions by type in dependency of the cooling rate. [19].....	7
Figure 3-1: Desired composition of alloys for experimental investigation in the systems a) Fe-0.5%Mn-var%S and b) Fe-2%Mn-var%S up to 0.3 wt.-% S. Calculation performed with the database of Kang [2] using FactSage 8.2. [10]	15
Figure 3-2: Production of laboratory samples by high frequency remelting (HFR), a) input of alloying material in the Al ₂ O ₃ crucible and b) casting chamber with inductive heating and Cu mold. [96]	16
Figure 3-3: Principle of the emergence of a DSC signal during a phase transformation. [99]	19
Figure 3-4: a) Pt-Rh sample holder/sensor and b) sample holder/sensor with sample, reference and Zr getter.....	20

Figure 3-5: Temperature program for the DSC study a) slow heating at 10 °C/min and b) rapid heating. Both cycles are carried out under Ar atmosphere and at a cooling rate of 20 °C/min.	21
Figure 3-6: Schematic evaluation of a DSC measurement in the high temperature range of the alloy Fe-0.5%Mn-0.15%S.	22
Figure 3-7: Observation of the dissolution of (Mn,Fe)S in the HT-LSCM and linking of the thermo-optical analysis with DSC signals.	23
Figure 4-1: Schematic workflow of the CALPHAD approach for thermodynamic modeling and optimizations of multi-component databases. [104]	25
Figure 4-2: Geometrical models for ternary systems, a) Kohler (symmetric) b) Kohler/Toop (asymmetric) c) Muggianu (symmetric) and d) Muggianu/Toop (asymmetric). [92]	29
Figure 4-3: BCC two-sublattice structure with preferred occupation of the atoms in the body center and on the corners. [109]	30
Figure 4-4: Concentration square with end members of a simple solution (A,B) _u (C,D) _v . [109]	30
Figure 5-1: DSC signals of various samples in the system a) Fe-0.5%Mn-var%S between 700 °C and 950 °C and b) Fe-2%Mn-var%S between 700 °C and 900 °C showing Curie-temperature and low-temperature BCC-FCC phase transformation.....	34
Figure 5-2: DSC signals of various samples in the system a) Fe-0.5%Mn-var% between 1370 °C and 1440 °C and b) Fe-2%Mn-var%S between 1400 °C and 1460 °C showing start and end temperature of the high-temperature FCC-BCC phase transformation.	35
Figure 5-3: DSC signals of various samples in the systems a) Fe-0.5%Mn-var%S between 1460 °C and 1550 °C, b) Fe-0.5%Mn-var%S between 1440 °C and 1490 °C and c) Fe-2%Mn-var%S between 1480 °C and 1540 °C showing solidus temperature, dissolution temperature of (Mn,Fe)S and melting temperature.	36
Figure 5-4: Calculated thermodynamic properties in the binary system Fe-Mn compared to the database of Huang [85], Witusiewicz et al. [67], Kim and Kang [3], shown by a) the integral enthalpy of mixing at 1600 °C compared to experimental data from references [50] and [67] and b) the activity of Mn at 1550 °C compared to experimental data from references [57]–[62]. Calculations performed with FactSage 8.2 [10].	40
Figure 5-5: The system Fe-var%Mn-0.017%C a) up to 100 wt.-% Mn and 1700 °C and b) up to 30 wt.-% Mn and 1000 °C compared to the database of Kim and Kang [3] and experimental	

data from Presoly [114] (DTA) and from references [47]–[49],[63],[64]. Calculation performed with FactSage 8.2 [10].	41
Figure 5-6: Phase diagram of the system Fe-Mn-C ^{low} at high temperatures with a trace C content of 0.017 wt.-% C a) up to 100 wt.-% Mn and b) up to 30 wt.-% Mn compared to the calculation of Kim and Kang [3] and experimental data from Presoly [114] (DTA) and reference [48]. Calculation performed with FactSage 8.2 [10].	41
Figure 5-7: Phase diagram of the ternary system Fe-10%Mn-var%C a) up to 10 wt.-% C and b) in the Fe-rich peritectic corner at high temperature compared to the calculation of Kim and Kang [3] and experimental data from Presoly [114] (DTA). Calculation performed with FactSage 8.2 [10].	42
Figure 5-8: Phase diagram of the system Fe-20%Mn-var%C up to 10 wt.-% C compared to the calculation of Kim and Kang [3] and experimental data from Presoly [114] (DTA) and reference [80]. Calculation performed with FactSage 8.2 [10].	43
Figure 5-9: Calculated solubility of C in liquid Fe-Mn-C alloy at various temperatures compared to the calculation of Kim and Kang [3] and experimental data from references [69]–[73],[115]. Calculation performed with FactSage 8.2 [10].	44
Figure 5-10: Calculated solubility of C in liquid Fe-Mn-C alloy in equilibrium with CO in gaseous phase and saturated with solid MnO a) under various partial pressures at 1450 °C and b) at various temperatures, compared to the calculation of Kim and Kang [3] and experimental data from references [69],[116]. Calculation performed with FactSage 8.2 [10].	44
Figure 5-11: Calculated iso-activity lines of Mn in liquid Fe-Mn-C alloy at various temperatures, a) 1463 °C, b) 1500 °C and c) 1550 °C, compared to the calculation of Kim and Kang [3] and experimental data from reference [74]. Calculation performed with FactSage 8.2 [10].	45
Figure 5-12: Calculated phase diagrams in the system Fe-Mn-C at a) 690 °C, b) 910 °C and c) 1050 °C with stable carbide phases, compared to experimental data from reference [75]. Calculation performed with FactSage 8.2 [10].	46
Figure 5-13: Calculated phase diagram of the system Fe-0.5%Mn-var%S-0.0176%C with up to 0.35 wt.-% S compared to the FSstel (2022) database and experimental data from this present study. Calculation performed with FactSage 8.2 [10].	47
Figure 5-14: Calculated phase diagram of the system Fe-2%Mn-var%S-0.0176%C with up to 0.35 wt.-% S compared to the FSstel (2022) database and experimental data from this present study. Calculation performed with FactSage 8.2 [10].	48

- Figure 5-15:** Comparison between calculated and measured FCC-BCC phase transformation temperatures in the systems with a) 0.5 wt.-% Mn and b) 2 wt.-% Mn using the exact chemical composition for every sample and the thermodynamic model of the present study.....49
- Figure 5-16:** Ternary phase diagrams of the system Fe-Mn-S at a) 1300 °C compared to experimental data of reference [41], b) 1300 °C in the Mn-rich corner compared to experimental data of reference [44] and c) 1600 °C compared to experimental data of reference [31]. Calculation performed with FactSage 8.2 [10].49
- Figure 5-17:** Calculated solubility of S in liquid Fe-Mn alloy in equilibrium with S₂ in gas phase at various partial pressures p(S₂) at a temperature of 1600 °C compared to the calculation of Kang [2] and experimental data of reference [34]. Calculation performed with FactSage 8.2 [10].50
- Figure 5-18:** Calculated solubility of (Mn,Fe)S in liquid Fe-Mn-S alloys compared to the calculation of Kang [2] at a) 1550 °C compared to experimental data from references [33],[117], b) 1570 °C compared to experimental data from reference [29], c) 1600 °C compared to experimental data from references [31],[32],[34],[117],[118] and d) 1615 °C compared to experimental data from reference [30]. Calculation performed with FactSage 8.2 [10].51
- Figure 5-19:** Calculated activity of S expressed as ratio p(H₂S)/p(H₂) over Mn in FCC phase at different temperatures compared to the calculation of Kang [2] and experimental data from references [12],[35]. Calculation performed with FactSage 8.2 [10].52
- Figure 5-20:** Calculated solubility of S in FCC phase in equilibrium with (Mn,Fe)S phase at different temperatures compared to the calculation of Kang [2] and experimental data of references [12],[30],[119]. Calculation performed with FactSage 8.2 [10].52
- Figure 5-21:** a) Relation between temperature and solubility product of the Liquid/MnS equilibrium between 1573 K and 1973 K in the range of 0 to 5 wt.-% Mn and 0 to 2 wt.-% S and b) comparison of the calculation using thermochemical software and the derived equation of the solubility product of MnS at 1823 K, compared to references [20],[120]–[123]. Calculations performed with FactSage 8.2 [10].54
- Figure 5-22:** a) Relation between temperature and solubility product of the BCC/MnS equilibrium between 1573 K and 1823 K in the range of 0 to 2 wt.-% Mn and 0 to 0.2 wt.-% S and b) comparison of the calculation using thermochemical software and the derived equation of the solubility product of MnS at 1673 K and 1573 K, compared to the calculation of Ueshima et al. [123]. Calculation performed with FactSage 8.2 [10].56
- Figure 5-23:** a) Relation between temperature and solubility product of the FCC/MnS equilibrium between 1373 K and 1723 K in the range of 0 to 2 wt.-% Mn and 0 to 0.1 wt.-% S

and b) comparison of the calculation using thermochemical software and the derived equation of the solubility product of MnS at 1523 K and 1373 K, compared to the calculation of Ueshima et al. [123]. Calculation performed with FactSage 8.2 [10].....56

List of tables

Table 2-1: Experimental studies conducted in the past in the binary and ternary systems Fe-Mn, Fe-Mn-C and Fe-Mn-S.	8
Table 3-1: specifications of the input materials for high frequency remelting.	16
Table 3-2: Target and actual chemical analysis of the 0.5 wt.-% Mn samples for DSC measurements.	17
Table 3-3: Target and actual chemical analysis of the 2 wt.-% Mn samples for DSC measurements.	17
Table 3-4: Calibration samples for temperature calibration of the DSC.	19
Table 4-1: Crystallographic information of stable phases in the system Fe-Mn-S. [2],[26]....	25
Table 4-2: Crystallographic information of stable phases in the system Fe-Mn-C. [3]	26
Table 5-1: Phase transformation temperatures obtained by DSC for the systems Fe-0.5%Mn-var%S and Fe-2%Mn-var%S (n.p.: no phase transformation according to DSC).	37
Table 5-2: Comparison between previous (start) parameters and optimized parameters. Start parameters are taken from Kim and Kang [3]	39
Table 5-3: Numerical values for the solubility product of MnS in equilibrium with liquid phase taken from the summary of Bernhard [124].	54
Table A-1: complete chemical analysis of the sample alloys	B
Table A-2: thermodynamic model parameters for the system Fe-Mn-C	C
Table A-3: thermodynamic model parameters for the system Fe-Mn-S	E

Table A-4: thermodynamic model parameters for the systems Fe-C-S and S-C F

Acronyms

bal.	balanced
wt.-%	weight percent
var%	varying content
L	Liquid phase
α , δ , BCC	body centered cubic phase
γ , FCC	face centered cubic phase
ϵ , HCP	hexagonal close packed phase
CBCC	Cubic body centered phase
CUB	Cubic phase
a	activity

1 Introduction

In the year 2022, nearly 97 % of the world's produced crude steel is produced via continuous casting process. [1] Continuous casting is an efficient process to produce numerous different steel grades and geometries, such as slabs, thin slabs, billets or blooms. Within the last years, Mn has become one of the most common alloying elements in steels. Typical amounts of Mn are up to 1.5 wt.-% in low-alloyed carbon steels, around 3 to 6 wt.-% in medium Mn steels and more than 10 wt.-% in high Mn steels for special purposes. Mn improves strength and work wear resistance of steels. Further, toughness at ambient temperatures but also at cryogenic temperatures is enhanced and ductility is increased for certain steel grades as for example medium Mn steels. These properties are decisive for many applications, such as TRIP and TWIP steels for automotive applications, high-Mn steels for cryogenic industry, high-Mn steels for heavy industry and many more. In contrary, S causes several severe problems during the processing and especially during the continuous casting of steel. Brought in mainly by coke and coal, S is one of the most critical elements in steelmaking. S segregates in interdendritic liquid and leads to hot tearing and surface defects due to hot shortness in continuously cast products. Furthermore, S decreases sour gas resistance and weldability of steel. In Mn alloyed steels, S and Mn form sulfides. Those sulfides are favorable if they form during solidification, as Mn bonds S and thus avoid strong segregations. However, as the (Mn,Fe)S solubility decreases during cooling, (Mn,Fe)S formation in the solid-state decreases the ductility of steel and favors defect formation during the bending and straightening in the caster. Nowadays, the control of the final sulfur content by means of hot metal desulfurization or desulfurization during ladle treatment is state-of-the-art, even down to only a few parts-per-million (ppm). The future production of for example ultra-low-carbon steel grades via the electric arc furnace (EAF) will

neither provide a desulfurization in steelmaking nor during secondary metallurgical treatment. The system Fe-Mn-C-S will therefore be of highest importance again.

Inner quality and surface quality of semi-finished products are greatly influenced by the correct control of the casting process. To improve the quality of semi-finished steel products and to increase productivity, online quality prediction systems (QPS) are on the rise in steel industry. Online QPS combine process parameters with thermodynamic-kinetic data of the material, giving information about risks and possible failures to operators. In recent decades, the development of self-consistent thermodynamic databases in the field of steelmaking has attracted a great deal of attention. So-called CALPHAD (CALculation of PHase Diagrams) databases are created by considering experimental investigations and atomistic simulations of pure substances and alloying systems. However, many experimental studies on steel systems were carried out several decades ago. As the methods by thermal analysis are continuously improving, the characterization of alloying systems is getting more precise. Hence, it is necessary to re-investigate systems with up-to-date methods to improve the accuracy of thermodynamic databases.

In the present study, the ternary system Fe-Mn-S is investigated using Differential Scanning Calorimetry (DSC), with emphasis on the solidification of steel and the formation of (Mn,Fe)S of Mn-alloyed steels containing a varying amount of S. The Mn contents of the investigated systems are 0.5 wt.-% and 2 wt.-% with S content from 0 up to 0.3 wt.-%, being highly relevant to steel producers. Special remark is given to the formation and dissolution of (Mn,Fe)S.

In the modeling part, a database for the Fe-Mn-S-C system is developed in the framework of the CALPHAD approach. Considering experimental data already measured at the Chair of Ferrous Metallurgy, the Fe-Mn and Fe-Mn-C system were critically reassessed. Then, an already existing description of the Fe-Mn-S system reported by Kang [2] was slightly modified to meet more accurately the DSC measurements in the Fe-Mn-S system. The consistency with extensive data from the literature is still given. Other subsystems (Fe-C, Fe-S, Mn-C, C-S and Fe-C-S) were taken from previous work of Kang and co-workers [2]–[6].

2 Literature review

A proper theoretical study is an important step towards the experimental investigation and the subsequent thermodynamic assessment of binary and ternary systems. A literature review regarding experimental procedures in the past allows a critical evaluation of possible steps and the avoidance of mistakes in terms of the preparation of samples as well as experimental methods. Further, the extraction of quantitative thermodynamic data is necessary for the optimizations in the binary and ternary systems. This chapter provides a background of the technical relevance of (Mn,Fe)S formation in steel and summarizes studies performed for the Fe-Mn, Fe-Mn-C and Fe-Mn-S systems relevant for the present work.

2.1 Influence of S and (Mn,Fe)S in continuous casting

S is usually considered as harmful tramp element detected in almost every steel grade. S is brought into the steelmaking process mainly by coke and coal, minor sources are scrap and iron ore. In general, S usually has a negative effect on the mechanical properties of steels. [7] S decreases the toughness and the hot ductility of steels leading to severe problems during the continuous casting process. Consequences of the high temperature embrittlement are inner as well as surface cracks in the semi-finished product. [8]

Hence, it is necessary to remove S in the ironmaking and steelmaking processes. **Figure 2-1** shows the influence of other elements on the activity of S in liquid Fe. Elements such as C and Si are widely used as alloying elements in steels and increase the activity of S in liquid Fe, resulting in better desulfurization of the steel melt. [9]

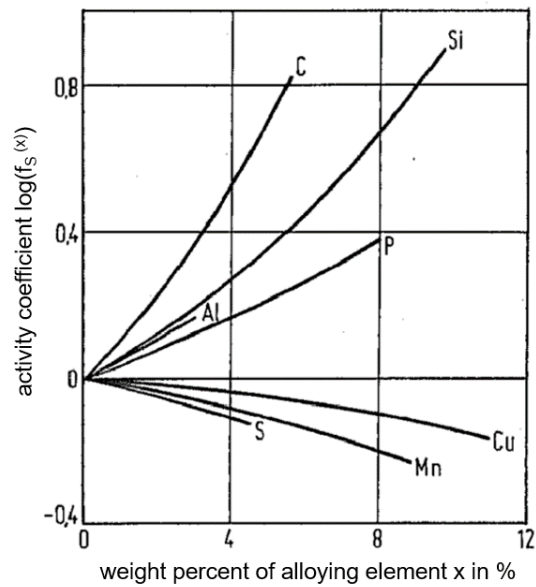


Figure 2-1: Influence of tramp and alloying elements on the activity of S in liquid Fe. [9]

After desulfurization, certain amounts of residual S remain in the melt. This residual S reacts with liquid components in the steel melt, such as Fe and Mn. During solidification, the solubility of S in FCC-Fe (γ -Fe) decreases significantly to 0.046 wt.-% at 1365 °C. The reduction of the solubility of S in solid Fe results in the formation of low melting Fe sulfides with a melting point of 988°C leading to red shortness at certain temperatures above. The binary phase diagram of Fe-S is given by **Figure 2-2**

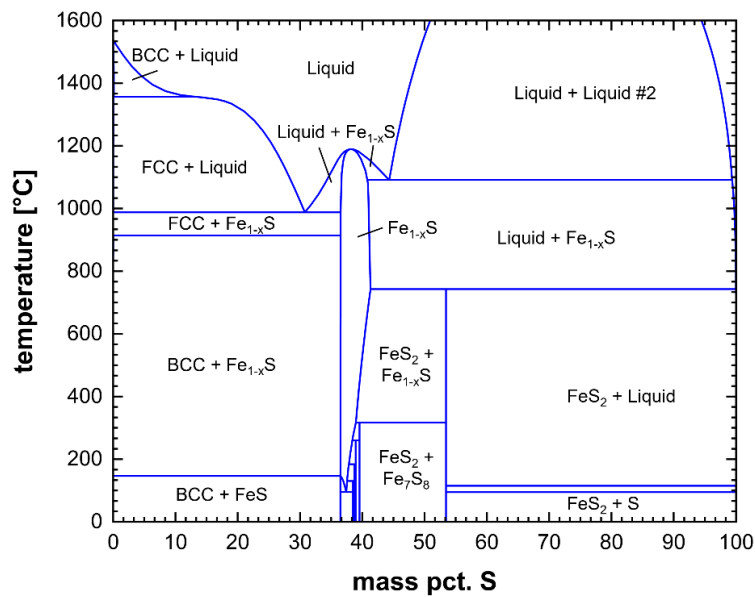


Figure 2-2: Binary Fe-S phase diagram calculated with thermodynamic description of Waldner and Pelton [6]. Calculation performed with FactSage 8.2 [10].

The addition of Mn to the system suppresses the formation of FeS due to higher affinity of S to Mn than Fe. Mn, as shown in **Figure 2-1**, further decreases the activity of S while simultaneously decreasing the solubility in solid FCC-Fe at 1335 °C to 0.0018 wt.-% and enhances the formation of MnS. Small amounts of Fe can dissolve in MnS leading to the formation of (Mn,Fe)S. If sufficient amounts of Mn are added to the steel melt, the occurrence of hot shortness due to FeS is suppressed. [11],[12] Hot shortness leads to surface cracks of the cast steel product under tensile stresses because of the presence of liquid films along grain boundaries. The lower the Mn content, the higher the risk of surface cracking. [13]

The reaction of binding of S with Mn is given by **Equation 2-1**, if S₂ is considered as a reference state [9]:



$$\Delta G^0 = -RT \ln \frac{a_{\text{MnS}}^2}{a_{\text{Mn}}^2 p_{\text{S}_2}} \quad \mathbf{2-2}$$

(Mn,Fe)S influences mechanical properties of steel to a great extent, although it must be mentioned that the formation of (Mn,Fe)S is desirable in some steel grades. (Mn,Fe)S increases the work wear resistance of steels and is therefore desired to be evenly distributed in tools of free cutting or free machining steels. [11]

(Mn,Fe)S are formed due to micro-segregation during solidification of steel in interdendritic regions. In the solid-state, (Mn,Fe)S may precipitate over the whole temperature range, starting from below solidus down the A_{r3}-temperature up to 1200 °C. The precipitation of (Mn,Fe)S inclusions leads to the effect of a shift of the second hot ductility drop to higher temperatures as shown in **Figure 2-3**. The precipitation temperature of (Mn,Fe)S and the second hot ductility trough meet with the straightening temperature range of continuous casting machines between 900 °C and 1080 °C. The hot ductility in this stage of the process is greatly reduced, which leads to surface cracks and deterioration in surface quality while bending and straightening the steel strand in the continuous casting process. [8],[11]

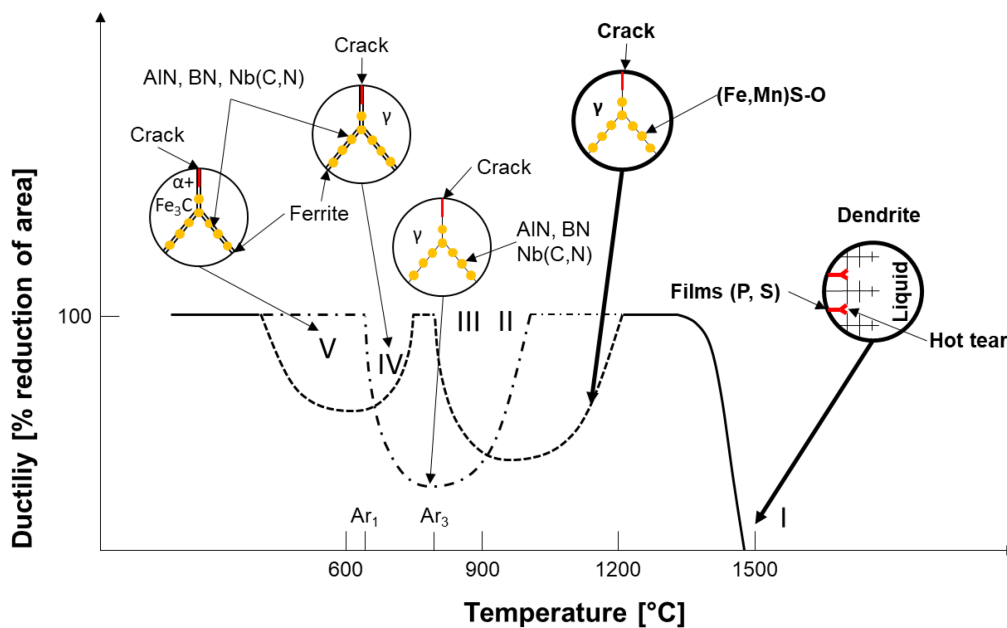


Figure 2-3: Reduced hot ductility related to precipitations in steels. [14]–[16]

The size, morphology, and the distribution of (Mn,Fe)S largely influences the mechanical properties. Therefore, Sims and Dahle [17] proposed a classification of (Mn,Fe)S by their shape. Randomly dispersed globular type I, the rod-like eutectic type II which is usually located at grain boundaries, and the angular type III. Matsubara [18] proposed a classification depending on their stage of formation. Sulfides formed in the liquid state correspond to (Mn,Fe)S inclusions of type I and III whereas sulfides formed on grain boundaries during solidification correspond to type II inclusions. [18],[19] Oikawa [20] later differentiated between 6 types of MnS depending on their changes of morphology after the addition of different alloying elements. [20]

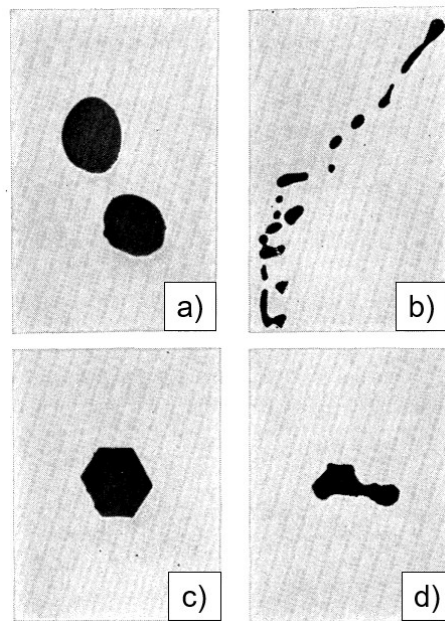


Figure 2-4: Different types of (Mn,Fe)S inclusions. a) type I b) type II c) type III and d) type X. [19]

The number and volume fraction of (Mn,Fe)S strongly depend on the cooling rate of the steel. According to Ito et al. [19], the number of inclusions of all types increase with increasing cooling rate. But, with increasing cooling rate, the volume fraction of type I and III inclusions, which are randomly dispersed in the steel matrix, decreases. In contrary, the type II inclusions formed at the grain boundaries increase in volume fraction with increasing cooling rate. The dependency of number and volume fraction of (Mn,Fe)S of type I, II and III are shown in **Figure 2-5**. [19]

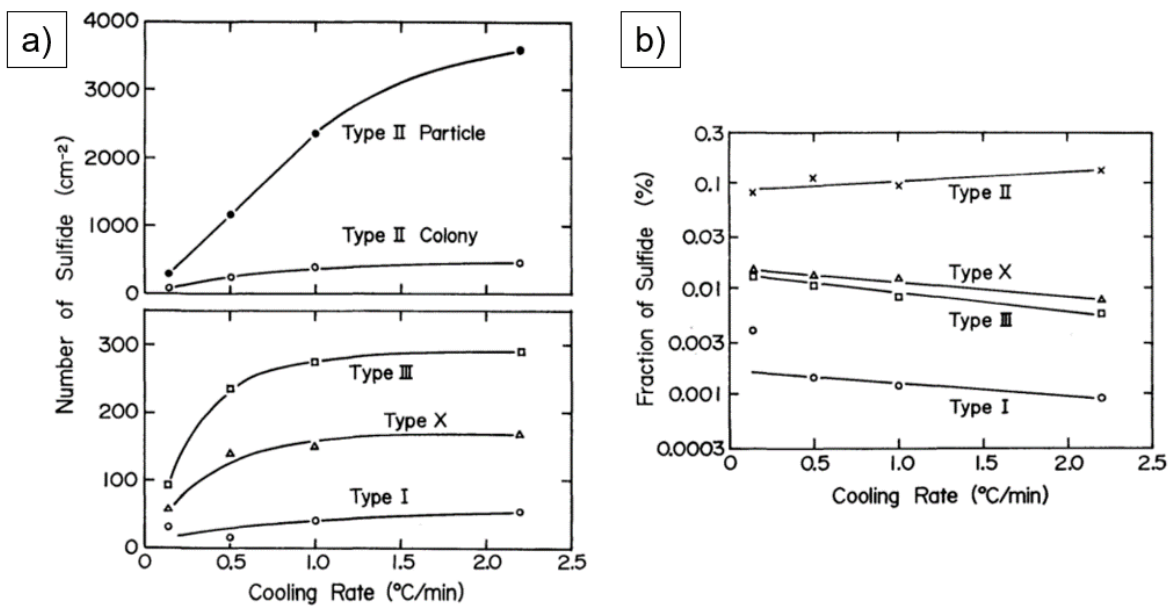


Figure 2-5: a) Number and b) volume fraction of sulfide inclusions by type in dependency of the cooling rate. [19]

2.2 Experimental studies

Research regarding the assessment of thermodynamic data of the binary and ternary systems Fe-Mn, Fe-Mn-C and Fe-Mn-S has been conducted within the last decades. For the experimental investigation of thermodynamics of steels, a great variety of sample preparation methods and experimental procedures were developed. All these experimental methods were used to measure thermodynamic properties and data, which can be used subsequently for more precise descriptions and continuous improvement of CALPHAD databases for steels. Thermodynamic data of pure substances have been carefully investigated in the past and are therefore not subject of this study. A consolidated work regarding thermodynamics of pure substances has been provided by Dinsdale [21] and is used for this work. **Table 2-1** gives an overview of conducted experimental investigations in the systems Fe-Mn, Fe-Mn-S and Fe-Mn-C.

For some binary and ternary systems, comprehensive literature reviews are available. The ternary systems Fe-Mn-S, Fe-Mn-C and Fe-C-S have been summarized by Raghavan [22]–[24] and Fe-C, Mn-S and Fe-Mn have been reviewed by Okamoto [25],[26] and Brandes and Flint [27], respectively.

Table 2-1: Experimental studies conducted in the past in the binary and ternary systems Fe-Mn, Fe-Mn-C and Fe-Mn-S.

Author, year	System	Method of investigation	Purpose of investigation
Turkdogan et al. [12]	Fe-Mn-S	Equilibration of Fe, Mn and S under H ₂ S / H ₂ gas atmosphere	Solubility of S in Fe and Fe-Mn alloys at 1200 °C / 1335 °C
Lin et al. [28]	Fe-Mn-S	Melting and equilibration of Fe, Mn and S at 1600 °C for 5 minutes	Effect of S and alloying elements on the morphology of MnS
Lu et al. [29]	Fe-Mn-S	Melting and equilibration of Fe, Mn and S at 1570 °C for 4 hours	Phase equilibria relations and activities
Sano et al. [30]	Fe-Mn-S	Equilibration of Fe, Mn and S at 1600 °C and 1615 °C	Phase relations of Fe, Mn and S
Vogel et al. [31]	Fe-Mn-S	Melting and equilibration of Fe, Mn and S for 4 to 5 minutes	Phase diagram and phase equilibria
Meyer et al. [32]	Fe-Mn-S	Melting and equilibration of Fe, Mn and S	Equilibrium and equilibrium constants between Fe, MnS and FeS
Ban-ya et al. [33]	Fe-Mn-S	Equilibration of Fe, FeS and Mn at 1550 °C under H ₂ S atmosphere	Effect of alloying elements on S activity

Sherman et al. [34]	Fe-Mn-S	Melting and equilibration of Fe, Mn and S at 1600 °C under H ₂ S / H ₂ gas atmosphere	Equilibrium data of S in Fe-Mn alloys
Fischer et al. [35]	Fe-Mn-S	Equilibration of Fe, Mn and S under H ₂ S / H ₂ gas mixture	Free energy data and activities
Mann et al. [36]	Fe-Mn-S	Equilibration of Fe, Mn and S	Phase relations of FeS and MnS
Ito et al. [37]	Fe-Mn-S	Equilibration of Fe, Mn and S at 1000 °C to 1500 °C for several hours	Kinetics of sulfide formation
Schürmann et al. [38]	Fe-Mn-S	Melting and equilibration of Fe, Mn and S at 1055 °C to 1457 °C	Equilibrium between Fe-FeS-Mn-MnS and on the phase diagram of the system Fe-Mn-S
Nakao [39]	Fe-Mn-S	Melting and diffusion annealing of Fe, FeS and MnS at 1300 °C for 6 minutes to 36 hours	Thermodynamics and kinetics of the system at 1300 °C
Smith [40]	Fe-Mn-S	Melting and diffusion annealing of Fe, FeS and MnS at 1200 °C to 1600 °C	Equilibrium and kinetic data for the Fe-Mn-S system
Kirkaldy et al. [41]	Fe-Mn-S	Melting and diffusion annealing of Fe, FeS and MnS at 1300 °C	Phase diagram of the system Fe-Mn-S at 1300 °C
Coughlin [42]	FeS-MnS	Heating of FeS and MnS for calorimetric study	Heat capacity of FeS, MnS and Pyrite
Kiessling et al. [43]	Fe-Me-S (Me = Ti, V, Cr, Fe, Co, Ni)	Equilibration of Fe, Mn, S at 1150 °C	Solid solubility limit for Mn in the system Fe-Mn-S
Dashevsky et al. [44]	Fe-Mn-S	Melting and equilibration of Fe, Mn, S	Solubility of S in Fe-Mn-S alloys at 1300 °C
Mann [45]	Fe-Mn-S	DTA and EPMA measurements of Fe-Mn-S alloys	Sub-solidus phase equilibria and phase diagram of Fe-Mn-S alloys and sulfide inclusions in the presence of Fe
Wada et al. [46]	Fe-S, Mn-S	Heating the samples to sulfidation temperature in a DTA	Thermochemical data of the sulfidation of Fe and Mn
Troiano et al. [47]	Fe-Mn	Melting and equilibration of Fe and Mn 20 °C under solidus temperature	FCC-BCC phase transition relations
Hellawell et al. [48]	Fe-Mn	Determination of heating and cooling curves for Fe-Mn alloys	Phase constitution of Fe and Mn
Hume-Rothery et al. [49]	Fe-Mn	Determination of heating and cooling curves for Fe-Mn alloys	Reassessment on the phase constitution of Fe and Mn
Batalin et al. [50]	Fe-Mn	Melting of Fe and Mn in an isothermal calorimeter	Mixing enthalpies of Fe-Mn alloys
Butler et al. [51]	Fe-Mn and Fe-Mn-C	Heating of Fe-Mn alloys to 1200 °C to 1270 °C and effusing Mn	Vapor pressure and activity of Mn in Fe-Mn alloys

Endoh et al. [52]	Fe-Mn	Melting and equilibration of Fe and Mn at 1000 °C for 60 hours	Magnetic properties of Fe-Mn alloys
Ishikawa et al. [53]	Fe-Mn	Melting and equilibration of Fe and Mn at 1050 °C and 1100 °C for one week	Antiferromagnetism and magnetic properties of FCC-Fe-Mn alloys
Ishikawa et al. [54]	Fe-Mn	Melting and equilibration of Fe and Mn at 1000 °C	Antiferromagnetism of FCC Fe-Mn alloys
Umebayashi et al. [55]	Fe-Mn	Melting and equilibration of Fe and Mn at 1040 °C for 40 / 48 hours	Antiferromagnetism of FCC-Fe-Mn alloys and the relation between magnetic and crystallographic transformation
Hillert et al. [56]	Fe-Mn	Melting and equilibrating of Fe and Mn at 850 °C	BCC-FCC phase relationship in Fe-Mn alloys
Sanbongi et al. [57]	Fe-Mn	Electrolytic cell of liquid Fe-Mn and Mn electrodes and slag for EMF measurement	Activity of Mn in Fe-Mn alloys
Schultz et al. [58]	Fe-Mn	Melting of Fe and Mn and evaporation of Mn	Activity of Mn in liquid Fe-Mn alloys
Schwerdtfeger [59]	Fe-Mn	Liquid Fe-Mn alloy as electrolyte and air / CO ₂ -CO / H ₂ -CO ₂ gas in Pt or Mo electrodes in a galvanic cell for EMF measurements	Oxygen activity under steelmaking process conditions
Steiler et al. [60]	Fe-Mn	Melting of Fe and Mn and evaporation of Mn	Correlation between Fe-Mn alloys and Raoult's law
Sudavtsova et al. [61]	Fe-Mn	Electrolytic cell of liquid Mn and Fe-Mn	Activity of Mn in liquid Fe-Mn alloys and deviation from Raoult's law
Jacob et al. [62]	Fe-Mn	Galvanic cells of solid and liquid Fe-Mn alloys for EMF measurements	Activity of Mn in solid and liquid Fe-Mn alloys
Predel et al. [63]	Fe-Mn	Melting and equilibrating of Fe and Mn at 1050 °C for 88 hours	Equilibrium relations and precipitation kinetics between Fe and Mn
Srivastava et al. [64]	Fe-Mn	Melting and equilibration of Fe and Mn at 1300 °C and 980 °C for 30 minutes	Tie lines between BCC and FCC in the phase diagram of the Fe-Mn system
Kubitz et al. [65]	Fe-Mn	Calorimetry of Fe and Mn	Mixing enthalpies of solid Fe-Mn alloys
Cotes et al. [66]	Fe-Mn	Melting and equilibration of Fe and Mn at 1000 °C for 1 to 48 hours	FCC / HCP martensitic phase transformation in the Fe-Mn system
Witusiewicz et al. [67]	Fe-Mn	Melting and calorimetry of Fe-Mn alloys	Formation enthalpy and heat capacity of liquid Fe-Mn alloys
Benz [68]	Fe-Mn	Electrolytic cell of Mn and Fe-Mn for EMF measurements	Study on solid-state Fe-Mn alloys
Kim et al. [69]	Fe-Mn-C	Melting of Fe-Mn-C alloys and equilibration with CO gas	Thermodynamic data of C in liquid Mn and Fe-Mn alloys with emphasis on decarburization

Chipman et al. [70]	Fe-Mn-C	Melting of Fe-Mn alloys in graphite crucibles and equilibration with the C containment	Solubility of C in liquid Fe-Mn alloys
Turkdogan et al. [71]	Fe-Mn-C	Melting of Fe-Mn alloys in graphite crucibles and equilibration with the C containment	Solubility of C in liquid Fe-Mn alloys
Ni et al. [72]	Fe-Mn-C	Melting of Fe-Mn-C alloys and equilibration with graphite	Solubility of C in liquid Fe-Mn alloys
Paek et al. [73]	Fe-Mn-C	Melting of Fe-Mn alloys in graphite crucibles	Thermodynamics of C in liquid Fe-Mn alloys
Enokido et al. [74]	Fe-Mn-C	Melting and equilibration between liquid Fe-Mn-C and Ag-Mn alloys	Activity of Mn in liquid Fe-Mn-C alloys
Kuo and Persson [75]	Fe-Mn-C	Equilibration of Fe-Mn-C powder mixtures at 690 °C (500 hours), 910 °C (100 hours) and 1050 °C (24 hours)	Phase equilibria of solid Fe-Mn-C alloys at different temperatures
Koch and Keller [76]	Fe-Mn-C	Equilibration of Fe-Mn-C alloys at 600 °C to 700 °C for several hundred hours	Mn distribution between phases of solid Fe-Mn-C alloys
Nishizawa [77]	Fe-Mn-C	Melting and homogenizing of Fe-Mn-C alloys and equilibrating at 1000 °C for 100 hours	Mn distribution between phases of solid Fe-Mn-C alloys
Benz et al. [78]	Fe-Mn-C	Carburization of Fe-Mn alloys in a H ₂ / CH ₄ gas at higher temperatures or annealing Fe-Mn-C samples at lower temperatures	Equilibrium phase relations of solid Fe-Mn-C alloys
Gurry et al. [79]	Fe-Mn-C	Equilibration of specimens from 15 minutes to 6 weeks at 371 °C to 693 °C and electrolytic extraction of carbides	Curie temperature, carbides and carbide distribution in Mn alloyed steels
Schürmann and Geissler [80]	Fe-Mn-C	Melting, equilibration and temperature measurement and quenching of Fe-Mn-C alloys	Phase equilibria in the ternary system Fe-Mn-C up to high Mn contents
Chen and Wang [81]	Fe-Mn-C	Melting and equilibration of Fe-Mn alloys in C-crucible at 1350 °C, 1425 °C and 1450 °C	Solubility and thermodynamic properties of C in liquid Fe-Mn alloys
Sil'man [82]	Fe-Mn-C	Melting and casting of Fe-Mn-C alloys with subsequent mechanical and heat treatment	Interphase distribution of Mn in carbides and austenite of cast iron
Tanaka [83]	Fe-Mn-C	Melting of Fe-Mn-C melts and measurement of the Mn vapor pressure over several hours	Activity of Mn in liquid Fe-Mn-C alloys

Wada et al. [84]	Fe-Mn-C	Melting, cooling and equilibration for several hours of Fe-Mn-C alloys between 848 °C to 1147 °C	Activity of C in Fe-Mn-C alloys in FCC phase
------------------	---------	--	--

2.3 Thermodynamic assessments of the Fe-Mn, Fe-Mn-C and Fe-Mn-S systems

In the past years, several thermodynamic assessments have been conducted in the systems Fe-Mn, Fe-Mn-C and Fe-Mn-S. For the present study, several publications served as initial sources for obtaining thermodynamic data from literature. Huang [85] modeled the system Fe-Mn based on experimental data of the past years using Bragg-Williams regular solution model. Witusiewicz et al. [86] re-assessed the Fe-Mn binary system using the same regular solution model. Both publications use similar primary literature for their studies. Starting from these publications, thermodynamic data gained from experiments in the Fe-Mn system were collected.

The system Fe-Mn-C was described by multiple authors. Huang [87] proposed a model of the system based on a substitutional model for the liquid phase and a two-sublattice model for solid solutions. Later, Djurovic et al. [88] published their study on this system. The thermodynamic model for this work was the Compound Energy Formalism (CEF) for all solid phases. Kim and Kang [3] published a thermodynamic re-assessment of the Fe-Mn-C ternary system using Modified Quasichemical Model (MQM) for liquid phase and the CEF for solid solutions. In this study, the authors proposed a description for the liquid Fe-Mn binary system based on MQM as well, while other phase were kept mainly unchanged from previous studies.

A very early thermodynamic assessment of the system Fe-Mn-S was conducted by Miettinen and Hallstedt [89] using a two-sublattice random mixing model for liquid phase and a substitutional model for solid solutions. Kang [2] re-assessed the Mn-S and Fe-Mn-S system using experimental data from past publications. Kang proposed a description based on MQM for the liquid phase with exception of the Fe-Mn system, which are modeled using the Bragg-Williams random mixing model and CEF for solid solutions. Several years later, Dilner et al. [90] published a thermodynamic assessment of the Mn-S and Fe-Mn-S systems. The description of Dilner et al. is based on the ionic two-sublattice model for the liquid phase and CEF for (Mn,Fe)S, Fe_{1-x}S and FeS₂ while metallic phases in the Fe-Mn system were adopted from Huang [85] and modeled using a substitutional model.

When it comes to the choice of thermodynamic models, real physical phenomena should be considered. A binary solution of liquid Fe and Mn is thermodynamically close to an ideal solution, which is the reason why the binary system can be modeled using a Bragg-Williams regular solution model. By adding compounds as C or S to the solution, the tendency of Short Range Ordering (SRO) in the melt may become stronger. For solutions with SRO, a physically more relevant model is needed to obtain better thermodynamic. The MQM was developed to provide a physically more realistic model for those solutions and was used in several thermodynamic assessments for the liquid phase. [91]–[93] Detailed information on the MQM will be given in **Chapter 4.1**.

3 Experimental investigation of the ternary system Fe-Mn-S

The following chapters provide an overview of the experimental procedure to characterize the system Fe-Mn-S in the present study. Preparation of the samples and the experimental procedure using Differential Scanning Calorimetry (DSC) are described in detail. The data obtained from the experimental investigation are considered for optimizations in the system Fe-Mn-S.

3.1 Sample preparation and chemical analysis

For the DSC studies, a total of 16 alloys are prepared. Two systems, Fe-0.5%Mn-var%S and Fe-2%Mn-var%S with varying (var) S contents up to 0.3 wt.-% are examined. For this study, it is of great importance to experimentally investigate the systems in a proper way, meaning that the alloys should cover a broad S concentration range of the phase diagram. The position of the alloys for DSC measurements in the phase diagrams of Fe-0.5%Mn-var%S and Fe-2%Mn-var%S alloys are shown in **Figure 3-1 a)** and **b)**. Alloys A-I to A-IV and B-I to B-III should cover the region where (Mn,Fe)S is not a stable phase in order to compare DSC signals with and without (Mn,Fe)S.

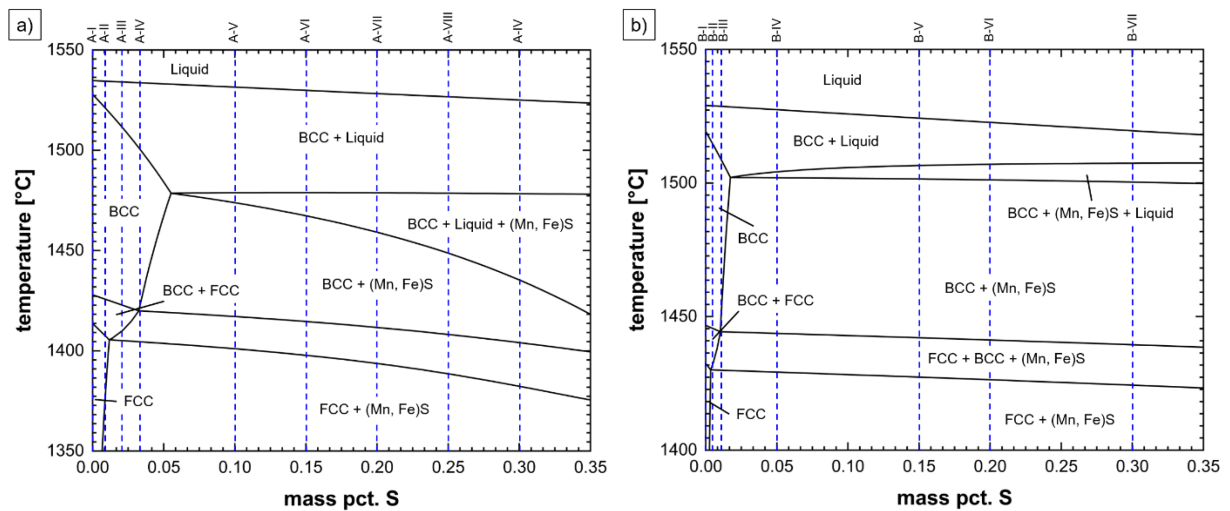


Figure 3-1: Desired composition of alloys for experimental investigation in the systems a) Fe-0.5%Mn-var%S and b) Fe-2%Mn-var%S up to 0.3 wt.-% S. Calculation performed with the database of Kang [2] using FactSage 8.2. [10]

The samples are prepared by weighing and placing the input materials as specified into an Fe crucible, which is sealed with a Fe lid. The total weight of the input materials mixture is between 60 and 68 grams. For all samples, 0.03 wt.-% Al is added to the alloy for de-oxidation of the steel melt. The actual Al content is measured between 0.02 and 0.037 wt.-% and the exact chemical composition is given in the appendix. Alloys are melted in the high frequency remelting furnace (HFR), allowing flexible production of laboratory samples. Input materials are placed in an alumina crucible located in a melting chamber which is closed and purged with protective Ar gas to prevent the melt from oxidation. The materials are melted via induction heating. Continuous stirring of the liquid by induction flow enables good mixing of the steel melt. After the alloy is melted completely, the steel is cast into a copper mold via centrifugal spinning of the melting chamber. Casting into a copper mold ensures rapid solidification and a homogenous sample which is desired for further investigations. **Figure 3-2** shows schematically the production of HFR samples. The Fe crucibles containing the alloy materials is turned upside down to prevent the evaporation of S and other volatile elements. The melting procedure has been adapted from Bernhard et al. [94],[95].

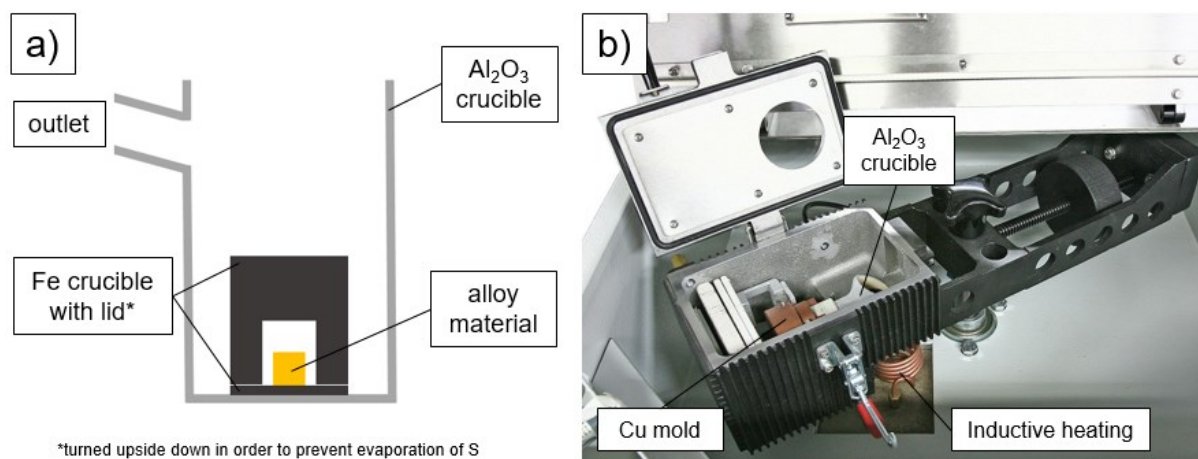


Figure 3-2: Production of laboratory samples by high frequency remelting (HFR), a) input of alloying material in the Al_2O_3 crucible and b) casting chamber with inductive heating and Cu mold. [96]

Table 3-1 shows detailed specifications of the input materials. Al, Mn and S are high purity materials, while the Fe crucible is an ultra-low carbon steel grade.

Table 3-1: specifications of the input materials for high frequency remelting.

Input material	Producer	LOT	Purity [wt.-%]
Fe crucible	Blyth Metals	/	Ultra-low carbon [%C = 0.00643]
Al wire	Alfa Aesar	36076	99.999
Mn granules	Alfa Aesar	N13E056	99.98
S pieces	Alfa Aesar	H12W026	99.99

After melting and solidification, the alloys are analyzed by OES at *voestalpine Stahl Linz GmbH*. In addition, combustion analysis (C/S LECO) is carried out for C and S at the *Graduate Institute of Ferrous and Eco Materials Technology* at *Pohang University of Science and Technology*. DSC samples of 2.1 x 2.1 x 1.5 mm are cut out of the HFR samples. The specimen must be grinded properly that the sample is in perfect contact with the bottom of the alumina crucible used in the DSC. Samples are cleaned in ethanol, acetone and again ethanol before weighing three times and taking the average weight.

The target composition and the actual composition of the alloys with 0.5 wt.-% and 2 wt.-% Mn are given in **Table 3-2** and **Table 3-3**. Any C content may originate from the Fe crucible which

is made from ultra-low C steel grade. A detailed chemical composition is shown in the appendix.

Table 3-2: Target and actual chemical analysis of the 0.5 wt.-% Mn samples for DSC measurements.

sample	target composition [wt.-%]			actual composition [wt.-%]		
	Fe	Mn	S	Mn ^(a)	S ^(b)	C ^(b)
A-I	bal.	0.50	0.000	0.52	0.0021	0.0197
A-II			0.010	0.52	0.0121	0.0148
A-III			0.025	0.51	0.0261	0.0132
A-IV			0.040	0.51	0.0417	0.0195
A-V			0.100	0.51	0.0944	0.0203
A-VI			0.150	0.50	0.1523	0.0130
A-VII			0.200	0.48	0.1930	0.0175
A-VIII			0.250	0.47	0.2370	0.0162
A-IX			0.300	0.47	0.3047	0.0125

^(a) Optical Emission Spectroscopy; ^(b) C/S combustion Analysis

Table 3-3: Target and actual chemical analysis of the 2 wt.-% Mn samples for DSC measurements.

sample	target composition [wt.-%]			actual composition [wt.-%]		
	Fe	Mn	S	Mn ^(a)	S ^(b)	C ^(b)
B-I	bal.	2.00	0.000	1.98	0.0025	0.0191
B-II			0.006	1.97	0.0082	0.0190
B-III			0.012	1.97	0.0145	0.0201
B-IV			0.050	1.94	0.0514	0.0155
B-V			0.150	1.93	0.1487	0.0178
B-VI			0.200	1.90	0.2053	0.0219
B-VII			0.300	1.88	0.3077	0.0209

^(a) Optical Emission Spectroscopy; ^(b) C/S combustion Analysis

3.2 Differential Scanning Calorimetry (DSC)

Phase transition temperatures of the alloys listed in **Table 3-2** and **Table 3-3** are investigated by Differential Scanning Calorimetry (DSC). The principle of DSC lies in the measurement of the temperature difference between a sample and a reference. A steel sample with defined geometry is placed in an inert crucible. A second empty crucible acts as the reference. Sample and reference are placed on a disk (typically Pt/Rh) with high thermal conductivity connecting the sample and the reference. Flat-type thermocouples are integrated in the disk below sample and reference. Both, sample, and reference, are heated up in the furnace with a pre-defined temperature program. The heat is transferred from the furnace to the sample and reference. When no phase transformation occurs, the temperature of both crucibles is identical. Phase transformations in steels are endothermic processes while heating. During a phase transformation, the heat flux into the sample is converted into transformation energy. The temperature of the reference steadily increases according to the temperature program while the temperature in the sample remains constant. At the end of a phase transformation, the temperature of the sample increases again and aligns with the temperature of the reference. [97],[98]

If no phase transformations occur, the DSC signal, typically given in mW/mg or μV , runs along a baseline. At the starting temperature of a transformation, the signal deviates from the baseline and appears as a curve-type signal while at the end of a transformation the signal re-aligns with the baseline. The area under the curve, measured in J/mg is proportional to the reaction enthalpy of the phase transformation. **Figure 3-3** shows the principle of the emergence of a DSC signal. [97]

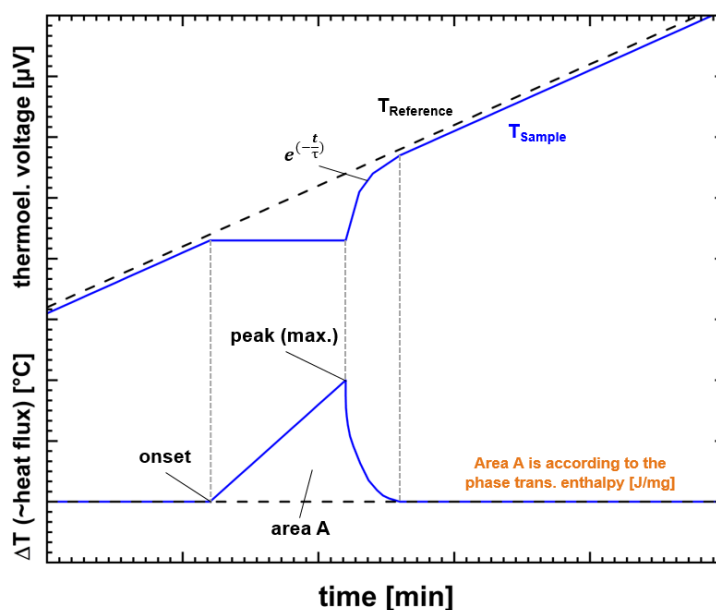


Figure 3-3: Principle of the emergence of a DSC signal during a phase transformation. [99]

The standard calibration of the DSC, adapted from Presoly et al. [100] and Bernhard et al. [94], is periodically checked with two different pure samples after approximately every 15 to 20 experimental cycles. For the check in the low temperature range, an Ag sample and for the high temperature range, a Co calibration sample is used. The melting point of Co at 1495 °C is similar to the FCC-BCC transition temperature of steel. The specifications of the calibration samples are listed in **Table 3-4**.

Table 3-4: Calibration samples for temperature calibration of the DSC.

Input material	Producer	LOT	Purity [wt.-%]
Au wire	Netzsch Gerätebau GmbH (Calibration set DTA/DSC)	/	99.999
Co wire	Alfa Aesar	I15T004	99.995

For the experimental investigation, the *DSC 404 F1 "Pegasus"* (Netzsch Gerätebau GmbH) [99] is used. The DSC consists of a high temperature rhodium furnace with a maximum temperature of 1570 °C. The atmosphere in the furnace is continuously purged with technically pure Ar gas to reduce the risk of residual oxygen to a minimum. Residual oxygen is minimized by a thermally active Zr getter placed below the sensor which is changed for every experiment. The sample holder and sensor are equipped with a radiation shield and hold an empty

reference crucible and a crucible with the specimen. The crucibles are made of Al_2O_3 and the sample is protected by an Al_2O_3 lid that is placed on top. The temperature is measured via flat Pt/Rh thermocouple integrated in the sample holder. Sample and reference are placed onto the high thermal conductivity sensor with thermocouples underneath. The sample holder, Pt/Rh sensor and crucibles are shown in **Figure 3-4**.

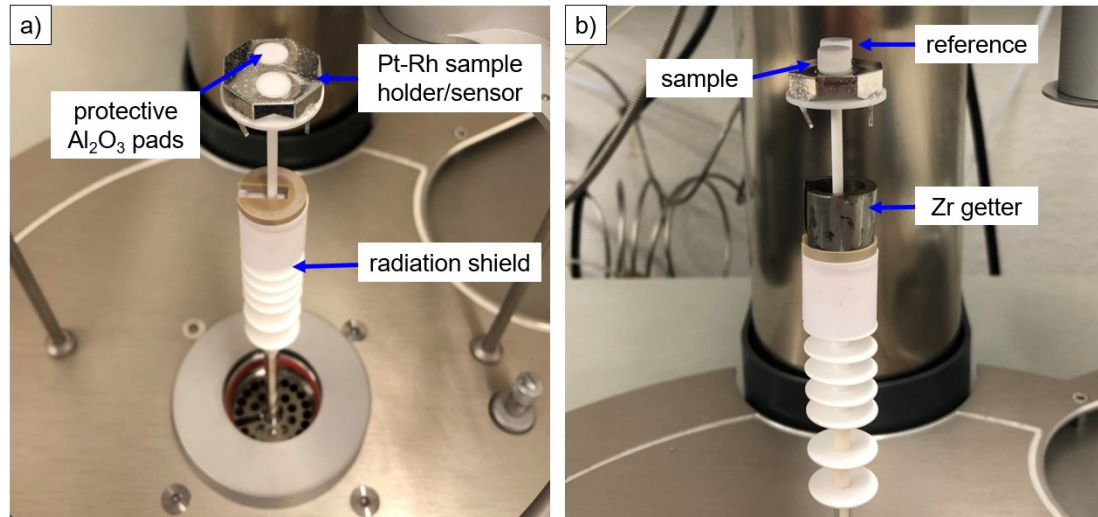


Figure 3-4: a) Pt-Rh sample holder/sensor and b) sample holder/sensor with sample, reference and Zr getter.

The experimental procedure for the DSC study is adapted and slightly adjusted from Bernhard et al. [94]. Usually, every alloy is investigated at least twice using new samples in each trial. The sample mass is very low to suppress temperature gradients and ensure uniform heating and melting. Before the beginning of a DSC measurement, the Rh furnace is evacuated and filled with Ar gas three times to decrease the oxygen content in the furnace to a minimum. The first run is the “slow heating” cycle as exemplary shown in **Figure 3-5 a)**. Slow heating serves the purpose of carrying out measurements near equilibrium state. The steel sample is heated under Ar atmosphere with a heating rate of $10\text{ }^\circ\text{C}/\text{min}$ until a temperature T_m of approximately $20\text{ }^\circ\text{C}$ above the computationally calculated melting temperature [10] is reached. After melting, the specimen is cooled to room temperature under Ar atmosphere with a cooling rate of $20\text{ }^\circ\text{C}/\text{min}$. The second run is carried out using a new sample. This cycle represents the “rapid heating” cycle, shown in **Figure 3-5 b)**, and serves the purpose of checking the reproducibility of measurements. The sample is heated up at a rate of $20\text{ }^\circ\text{C}/\text{min}$ to the start temperature of the low temperature range, which is about $125\text{ }^\circ\text{C}$ lower than the obtained Curie temperature of the alloy from the first run. The sample is held at this temperature, $T_{LT,start}$, for 15 minutes for equilibration. Starting from $T_{LT,start}$, the furnace is heated at a rate of $10\text{ }^\circ\text{C}/\text{min}$ to a temperature of about $25\text{ }^\circ\text{C}$ above the BCC-FCC phase transformation, which is referred to as $T_{LT,end}$. The

high-temperature range begins at approximately 125 °C below the FCC-BCC phase transition. This temperature is designated as $T_{HT,start}$. The sample is held at this temperature for another 15 minutes. Subsequently, the melting cycle begins. The specimen is heated up to a temperature, T_m , of approximately 10 °C above melting temperature measured in the first run. Just after melting, the sample is cooled to $T_{HT,start}$ and heated up to T_m again, followed by cooling the sample to room temperature. [94]

Measured phase transformation temperatures must be similar in the first and second run to count as a valid experiment. Heating cycles must be developed for each alloy based on the investigated melting and phase transformation temperatures of the “slow heating” cycle.

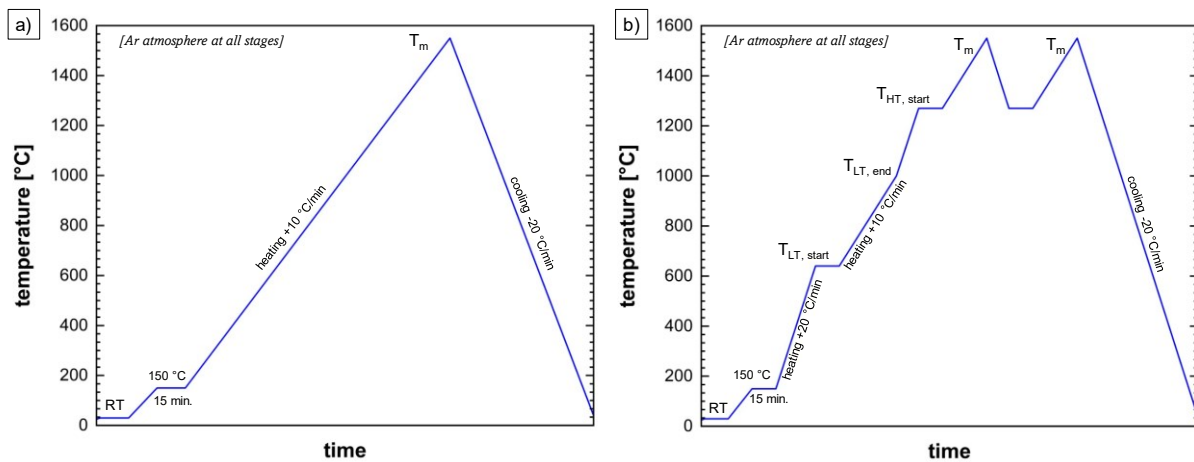


Figure 3-5: Temperature program for the DSC study a) slow heating at 10 °C/min and b) rapid heating. Both cycles are carried out under Ar atmosphere and at a cooling rate of 20 °C/min.

During the heating and cooling cycles, the DSC signal and the temperature are continuously recorded by the sensor and the thermocouples. At the end of the investigation of a sample, the results can be evaluated by a commercial software. In DSC studies, the influence of the furnace and the sample on the investigated phase transition temperatures are significant. The heating rate of the furnace does not affect the measured onset of phase transformations, but shifts the measured end temperature of phase transformations. [95] The higher the heating rate, the greater the influence on measurements. To correct this influence, the measurements have to be extrapolated to a heating rate of 0 °C/min, which is considered equilibrium state. For this study, the signals have been corrected by the *TauR*-method provided by the analysis software and manual extrapolation to equilibrium state can be omitted. This mathematical model automatically corrects the influence of heating rate, thermal resistivity R and the time constant τ . Additionally, the DSC signal is corrected to a manual offset, meaning that the baseline of the signal is manually set to a value of 0. **Figure 3-6** displays an offset-corrected evaluation of a measurement with and without application of *TauR*-method. It is clearly visible

that the measured liquidus temperature is higher than the actual, *TauR*-corrected measurement. Bernhard et al. [94] studied and compared manual correction of measurements by extrapolation to equilibrium state with *TauR*-method and obtained excellent correlation of the results. [94],[99]

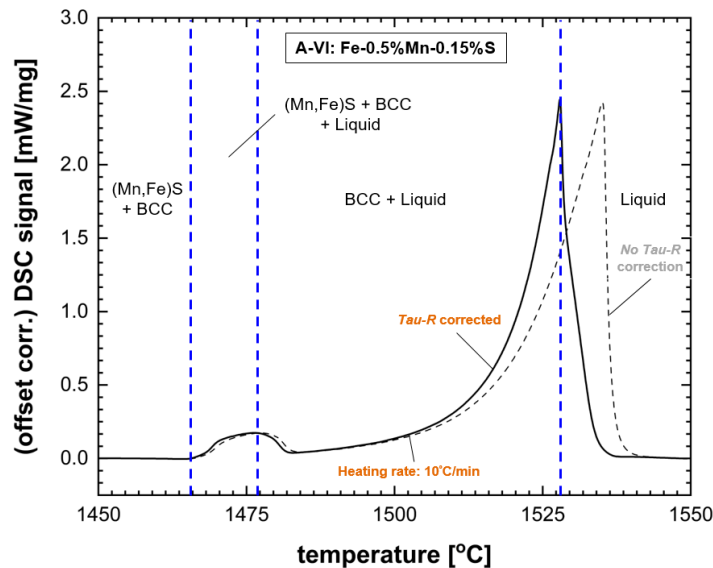


Figure 3-6: Schematic evaluation of a DSC measurement in the high temperature range of the alloy Fe-0.5%Mn-0.15%S.

3.3 Thermo-optical analysis (TOA)

Temperature-dependent microstructural changes in a specimen, such as phase transformation or the formation and dissolving of inclusions can be optically determined by TOA. In the present study, selected specimens are investigated using the high temperature laser scanning confocal microscope (HT-LSCM) of the type *Yonekura VL 2000DX*. HT-LSCM allows rapid heating up to high temperatures and promises high resolution due to the use of a blue laser which is, in contrary to other optical methods, not in the spectrum of steel samples. Detailed information about using HT-LSCM along with DSC can be found in other references. [94],[95],[100]–[102]

During the production of the HFR samples, the rapid cooling rate may lead to the formation of (Mn,Fe)S far away from the thermodynamic equilibrium. Hence, it is required to check the DSC measurements with optical methods to verify that (Mn,Fe)S fully dissolves during heating according to the DSC chart. The dissolving of (Mn,Fe)S in the sample A-IV (Fe-0.5%Mn-0.15%S) is clearly visible by HT-LSCM trials, see **Figure 3-7**. The temperature range below and above the three-phase field (Mn,Fe)S + BCC + Liquid is from prior interest. The evaluation

of TOA shows very satisfying results. As can be seen in the lower left-hand picture in **Figure 3-7**, (Mn,Fe)S inclusions appear as small dark-grey spheres and are stable below the solidus temperature. When the solidus temperature is exceeded, (Mn,Fe)S begin to dissolve and finally disappear at a certain temperature in the solid state below the liquidus temperature, as can be seen on the lower right-hand picture. The obtained temperatures of stability and dissolution of (Mn,Fe)S by TOA are in very good accordance with the DSC signal and can therefore be clearly allocated to evaluated phase fields in DSC.

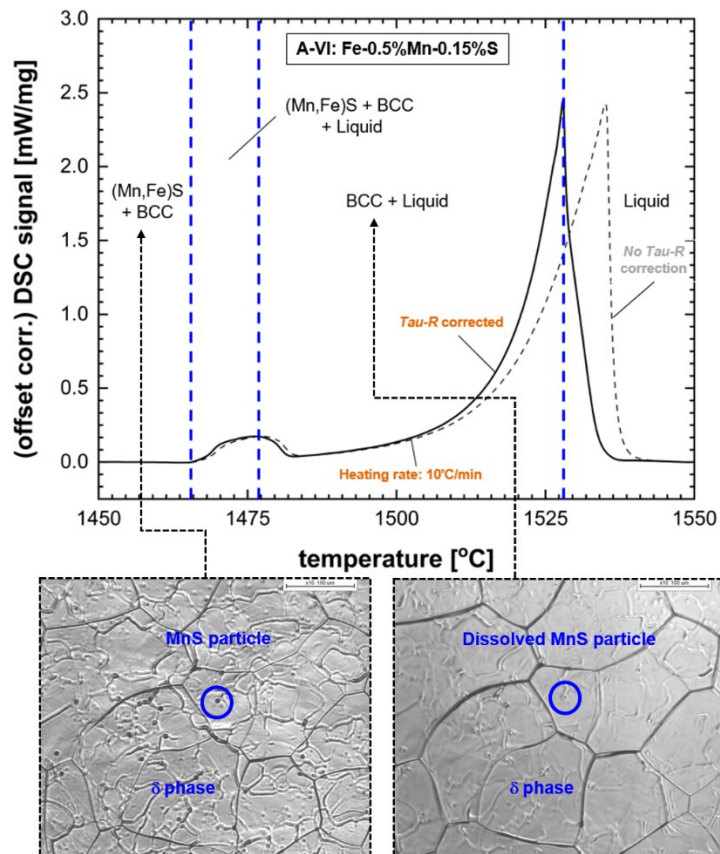


Figure 3-7: Observation of the dissolution of (Mn,Fe)S in the HT-LSCM and linking of the thermo-optical analysis with DSC signals.

4 Thermodynamic modeling

This chapter provides a detailed theoretical background and mathematical explanations of applied thermodynamic models for the optimization of the systems Fe-Mn, Fe-Mn-C and Fe-Mn-S. The Liquid phase is described by the Modified Quasichemical Model (MQM), solid solutions of Fe and Mn as well as (Mn,Fe)S (Alabandite) and (Fe,Mn)S (Pyrrhotite) are described by Compound Energy Formalism (CEF). The properties of stoichiometric compounds are taken directly from literature.

Thermodynamic databases are important tools for the steel industry. Therefore, the investigation of thermodynamic data and the processing of those data is a crucial step. For thermodynamic modeling of multi-component systems like steels, the CALPHAD method poses a consistent. The general workflow of the CALPHAD approach is shown in **Figure 4-1**. In the first step, input data has to be obtained experimentally or taken from literature. For the present work, DSC (Fe-Mn-S) and DTA (Fe-Mn, Fe-Mn-C) measurements have been prepared for input as well as all data obtained from literature. Also, suitable thermodynamic models must be selected. The choice of the model depends on the components and the complexity of the system. Thermodynamic models used for this study are explained in **Chapter 4.1** to **4.3**. In the second step, model parameters are optimized according to literature or experimentally obtained data. The optimization is carried out by varying the parameters until errors in calculations are minimized. The CALPHAD approach has been well discussed in literature, see [92],[103]

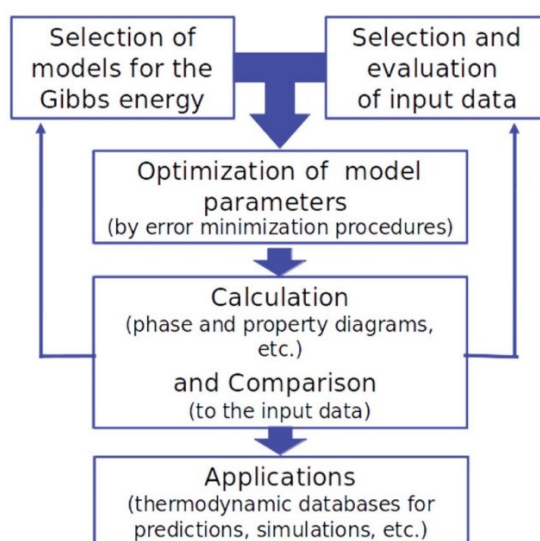


Figure 4-1: Schematic workflow of the CALPHAD approach for thermodynamic modeling and optimizations of multi-component databases. [104]

Table 4-1 and **Table 4-2** give an overview of the stable phases which can be found in the systems Fe-Mn-S and Fe-Mn-C along with crystallographic information, such as prototype, Pearson symbol, space group and Strukturbericht. For easier readability, both systems are listed separately. It has to be noted that reliable data about crystallographic properties are not available for all phases. Some data can be obtained by online databases. For this study, only data given in reviewed literature is shown.

Table 4-1: Crystallographic information of stable phases in the system Fe-Mn-S. [2],[26]

Phase		Pearson symbol	Space group	Strukturbericht	Prototype	Thermodynamic model
L	Liquid	/	/	/	/	MQM
α -Fe, α -Mn	BCC	<i>cI2</i>	<i>Im$\bar{3}m$</i>	A2	<i>W</i>	CEF
γ -Fe, γ -Mn	FCC	<i>cF4</i>	<i>Fm$\bar{3}m$</i>	A1	<i>Cu</i>	CEF
δ -Fe, δ -Mn	BCC	<i>cI2</i>	<i>Im$\bar{3}m$</i>	A2	<i>W</i>	CEF
α -Mn	CBCC	<i>cI58</i>	<i>I$\bar{4}3m$</i>	A12	<i>α-Mn</i>	CEF
β -Mn	CUB	<i>cP20</i>	<i>P4$_1$32</i>	A13	<i>β-Mn</i>	CEF
α -S	orthorhombic	<i>oF20</i>	<i>Fddd</i>	A16	<i>α-S</i>	STC
β -S	monoclinic	<i>mP64</i>	<i>P2$_1$/c</i>	/	<i>β-S</i>	STC
(Mn,Fe)S	MS	<i>cF8</i>	<i>Fm$\bar{3}m$</i>	B1	<i>NaCl</i>	CEF

MnS ₂	MS ₂	<i>cP12</i>	<i>Pa</i> $\bar{3}$	<i>C2</i>	FeS ₂	STC
(Fe,Mn)S	MS	<i>hP4</i>	<i>P6</i> ₃ / <i>mmc</i>	/	NiAs	CEF
FeS	MS	<i>hP24</i>	<i>P</i> $\bar{6}$ 2 <i>c</i>	/	FeS	STC
Fe ₁₁ S ₁₂	M ₁₁ S ₁₂	/	/	/	/	STC
Fe ₁₀ S ₁₁	M ₁₀ S ₁₁	/	/	/	/	STC
Fe ₉ S ₁₀	M ₉ S ₁₀	/	/	/	/	STC
Fe ₇ S ₈	M ₇ S ₈	<i>hP45</i>	<i>P3</i> ₁ 21	/	Fe ₇ S ₈	STC
FeS ₂	MS ₂	<i>cP12</i>	<i>Pa</i> $\bar{3}$	/	FeS ₂	STC

MQM: Modified Quasichemical Model; CEF: Compound Energy Formalism; STC: Stoichiometric Compound

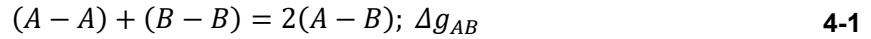
Table 4-2: Crystallographic information of stable phases in the system Fe-Mn-C. [3]

Phase		Pearson symbol	Space group	Strukturbericht	Prototype	Thermodynamic model
L	Liquid	/	/	/	/	MQM
α -Fe, α -Mn	BCC	<i>cI2</i>	<i>Im</i> $\bar{3}m$	<i>A2</i>	<i>W</i>	CEF
γ -Fe, γ -Mn	FCC	<i>cF4</i>	<i>Fm</i> $\bar{3}m$	<i>A1</i>	<i>Cu</i>	CEF
δ -Fe, δ -Mn	BCC	<i>cI2</i>	<i>Im</i> $\bar{3}m$	<i>A2</i>	<i>W</i>	CEF
α -Mn	CBCC	<i>cI58</i>	<i>I</i> $\bar{4}$ 3 <i>m</i>	<i>A12</i>	<i>α-Mn</i>	CEF
β -Mn	cub	<i>cP20</i>	<i>P4</i> ₁ 32	<i>A13</i>	<i>β-Mn</i>	CEF
ϵ -Mn	HCP	<i>hP2</i>	<i>P6</i> ₃ / <i>mmc</i>	<i>A3</i>	<i>Mg</i>	CEF
(Mn,Fe) ₃ C	M ₃ C	<i>oP16</i>	<i>Pnma</i>	<i>D0</i> ₁₁	<i>Fe</i> ₃ <i>C</i>	CEF
(Mn,Fe) ₅ C ₂	M ₅ C ₂	<i>mC28</i>	<i>C2/c</i>	/	<i>Pd</i> ₅ <i>B</i> ₂	CEF
(Mn,Fe) ₇ C ₃	M ₇ C ₃	<i>oP40</i>	<i>Pnma</i>	<i>D10</i> ₁	<i>Cr</i> ₇ <i>C</i> ₃	CEF
(Mn,Fe) ₂₃ C ₆	M ₂₃ C ₆	<i>cF116</i>	<i>Fm</i> $\bar{3}m$	<i>D8</i> ₄	<i>Cr</i> ₂₃ <i>C</i> ₆	CEF
C	graphite	<i>hP4</i>	<i>P6</i> ₃ / <i>mmc</i>	<i>A9</i>	<i>C</i>	STC

MQM: Modified Quasichemical Model; CEF: Compound Energy Formalism; STC: Stoichiometric Compound

4.1 Liquid phase

The liquid phase is described by the Modified Quasichemical Model (MQM). [92],[93] The MQM represents a more realistic model of solutions with Short Range Ordering (SRO) tendency, such as metallic melts containing non-metallic elements [4],[6],[94],[105] In the pair approximation for a binary solution consisting of A and B atoms, the following pair exchange reaction on the sites of a quasi-lattice considered (**Equation 4-1**):



Δg_{AB} describes the change of the non-configurational Gibbs energy for the formation of two moles of (A - B) pairs. The first nearest neighbor (FNN) coordination numbers Z_A and Z_B of A and B are described by **Equation 4-2** and **4-3**. n_A and n_B are the number of moles of A and B and n_{ij} is the number of moles of pairs. For solid solutions, it is necessary that $Z_A = Z_B$.

$$Z_A n_A = 2n_{AA} + n_{AB} \quad 4-2$$

$$Z_B n_B = 2n_{BB} + n_{AB} \quad 4-3$$

It is further necessary to introduce pair fractions, given by **Equation 4-4**,

$$X_{ij} = \frac{n_{ij}}{n_{AA} + n_{BB} + n_{AB}} \quad 4-4$$

and overall site fractions which are also referred to as overall mole fractions, given by **Equation 4-5**.

$$X_A = \frac{n_A}{n_A + n_B} = 1 - X_B \quad 4-5$$

Coordination-equivalent fractions are defined through **Equation 4-6**.

$$Y_A = \frac{Z_A n_A}{Z_A n_A + Z_B n_B} = \frac{Z_A X_A}{Z_A X_A + Z_B X_B} = 1 - Y_B \quad 4-6$$

If $Z_A = Z_B$, it can be formulated that $Y_A = X_A$ and $Y_B = X_B$. With the **Equations** above, it follows that

$$Y_A = X_{AA} + \frac{X_{AB}}{2} \quad 4-7$$

$$Y_B = X_{BB} + \frac{X_{AB}}{2} \quad 4-8$$

The Gibbs energy of a solution of A and B is given by **Equation 4-9**. Δg_A^0 and Δg_B^0 are molar Gibbs energies of the pure substances A and B .

$$G = (n_A g_A^0 + n_B g_B^0) - T \Delta S^{config} + \left(\frac{n_{AB}}{2}\right) \Delta g_{AB} \quad 4-9$$

ΔS^{config} describes the configurational entropy of mixing when the pairs $(A - A)$, $(B - B)$ and $(A - B)$ are randomly distributed. ΔS^{config} is described by **Equation 4-10**.

$$\Delta S^{config} = -R(n_{AA} \ln X_{AA} + n_{BB} \ln X_{BB} + n_{AB} \ln X_{AB}) + R(n_{AA} \ln Y_A^2 + n_{BB} \ln Y_B^2 + n_{AB} \ln 2Y_A Y_B) - R(n_A \ln X_A + n_B \ln X_B) \quad 4-10$$

Equation 4-10 is an approximation due to the lack of a mathematical description for the entropy of distribution in three dimensions. [92]

Δg_{AB} is a model parameter and can be described as **Equation 4-11**

$$\Delta g_{AB} = \Delta g_{AB}^0 + \sum_{i \geq 1} g_{AB}^{i0} X_{AA}^i + \sum_{j \geq 1} g_{AB}^{0j} X_{BB}^j \quad 4-11$$

with Δg_{AB}^0 , g_{AB}^{i0} and g_{AB}^{0j} being parameters as a function of temperature. These terms represent thermodynamic model parameters. [2],[92]

For ternary systems in the liquid phase, additional geometric models are required. Four of these models, which are widely used in thermodynamic databases, are shown in **Figure 4-2**. The Kohler and Muggianu models are symmetric models, whereas the Kohler/Toop and Muggianu/Toop models are asymmetric models. In asymmetric models, one component is singled out as the asymmetric component, e.g., component 1 in **Figure 4-2 (b)** and **(d)**. This procedure is physically relevant when components 2 and 3 are chemically similar while component 1 is chemically different. Examples are S-Fe-Cu or S-Fe-Mn, where S is chemically different from the other two components. [92],[106]

In the present study, the Kohler/Toop model is used as asymmetric geometric model for chemically indifferent ternary systems. One component in the ternary system is set as the asymmetric component. The expression “*Toop-like*” interpolation refers to this geometric model.

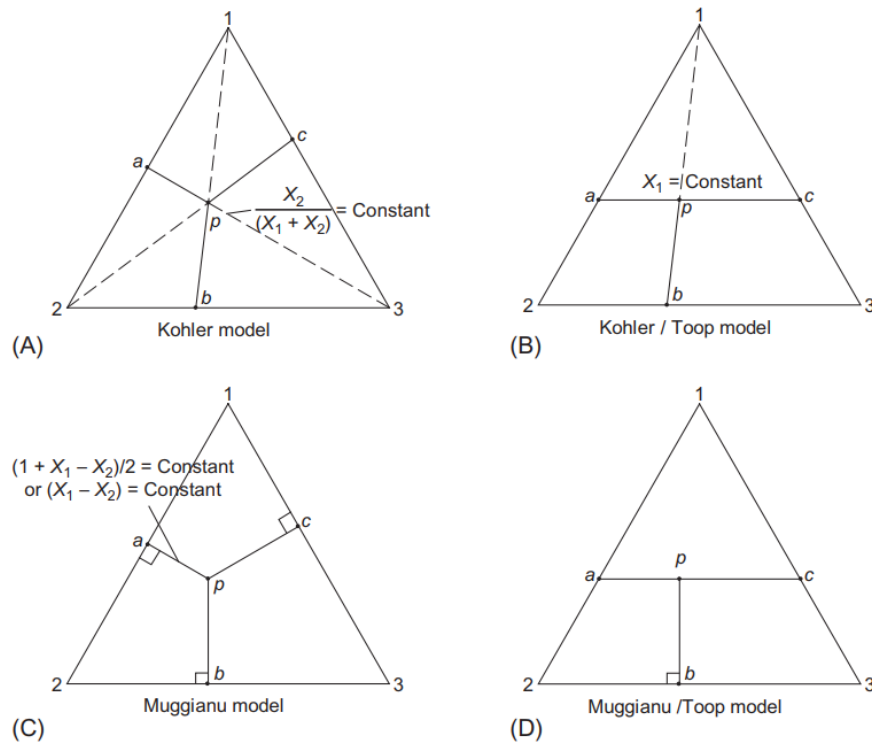


Figure 4-2: Geometrical models for ternary systems, a) Kohler (symmetric) b) Kohler/Toop (asymmetric) c) Muggianu (symmetric) and d) Muggianu/Toop (asymmetric). [92]

4.2 Solid solutions

The solid solutions of Fe and Mn, (Fe,Mn)S (Pyrrhotite) and (Mn,Fe)S (Alabandite) phase as well as M_3C , M_5C_2 , M_7C_3 and $M_{23}C_6$ ($M = Fe, Mn$) carbide phases are described by the Compound Energy Formalism (CEF) [107]. Two-sublattice models seem to be sufficient for the present work with exception of the $M_{23}C_6$ carbide phase, where a three-sublattice model was proposed in literature. Depending on temperature and pressure, Fe has three allotropic states, α -Fe (BCC), γ -Fe (FCC) and δ -Fe (BCC) while Mn has four allotropic states, α -Mn (BCC), β -Mn (FCC), γ -Mn (BCC) and ε -Mn (HCP). [2]

The CEF is a random mixing model, where multiple sublattices can be assumed, occupied by selected components in the system. Depending on the number of species in a multi-component system, the number of sublattices can vary. The multi-sublattice model has been proposed by Sundman and Agren [108] and was developed subsequently to two-sublattice models, which have been proposed already earlier. **Figure 4-3** shows a simple BCC structure with 2

sublattices. The preferred occupation of the atoms is in the center of the body and on corners of the lattice. [108],[109]

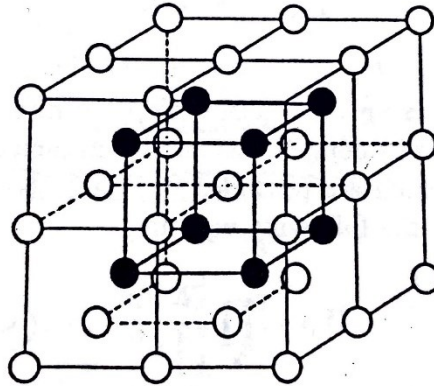


Figure 4-3: BCC two-sublattice structure with preferred occupation of the atoms in the body center and on the corners. [109]

In CEF, an endmember is a metastable, unstable or hypothetical compound in a multi-component system. Endmembers are defined as compounds, where every sublattice is fully occupied by only a single species. The Gibbs energy of endmembers is part of the formalism, whereas the combination of the energies of these endmembers build the model parameters for thermodynamic approach. **Figure 4-4** shows a concentration square with all endmembers located at the corners. In this regions, only one end member occupies the lattice. [92],[109]

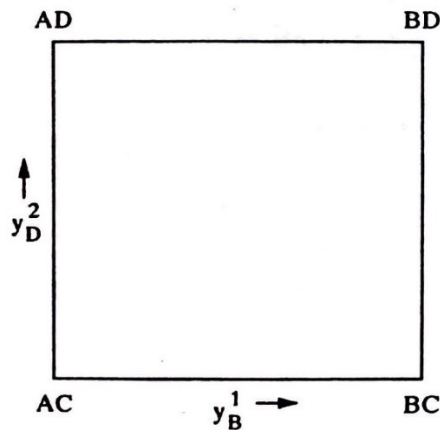


Figure 4-4: Concentration square with end members of a simple solution $(A,B)_u(C,D)_v$. [109]

The Gibbs energy of an interstitial solution of $(A,B)_u(C,D)_w$, where A and B are randomly distributed on the first lattice (y'_A and y'_B), C and D randomly on the second lattice (y''_C and y''_D) and u and w are stoichiometric values, is described by

$$\begin{aligned}
 G &= y'_A y''_C G_{A:C} + y'_A y''_D G_{A:D} + y'_B y''_C G_{B:C} + y'_B y''_D G_{B:D} \\
 &+ RT(u(y'_A \ln y'_A + y'_B \ln y'_B) + w(y''_C \ln y''_C + y''_D \ln y''_D)) \\
 &+ \sum_{A,B,C} y'_A y'_B y''_C L_{A,B:C} + \sum_{A,B,C} y'_C y'_A y'_B L_{C:A,B} + \sum_{A,B,C,D} y'_A y'_B y''_C y''_D L_{A,B:C,D} + G_m^{magn}
 \end{aligned} \tag{4-12}$$

where y' and y'' are site fractions of the first and second sublattice, respectively. The values for u and v depend on the crystal structure. For FCC phase, $u = w = 1$, whereas for BCC, $u = 1$ and $w = 3$. **Equation 4-12** has to be adapted if A, B, C or D can change their position within the two sublattices. [92],[109],[110]

The “L-parameters” are model parameters and are optimized during thermodynamic modeling. Those parameters are typically expressed by Redlich-Kister polynomials. [111] For binary systems, the L-parameter in the form of Redlich-Kister polynomial can be written as [16]

$$L_{ij} = \sum_{v=0}^n (x_i - x_j)^v {}^v L_{ij} \tag{4-13}$$

where ${}^a L_{ij}$ is temperature-dependent and formulated as [16]

$${}^v L_{ij} = {}^v a_{ij} + {}^v b_{ij} T \tag{4-14}$$

Interaction terms in ternary system, as proposed by Hillert [112], can be expressed as [16]

$$L_{ijk} = \omega_i {}^i L_{ijk} + \omega_j {}^j L_{ijk} + \omega_k {}^k L_{ijk} \tag{4-15}$$

and $\omega_{i,j,k}$ is given by [16]

$$\omega_{i,j,k} = x_{i,j,k} + \frac{(1 - x_i - x_j - x_k)}{3} \tag{4-16}$$

G_m^{magn} describes the magnetic contribution to the Gibbs Energy. G_m^{magn} can be described by

$$G_m^{magn} = RT \ln(\beta_0 + 1) g(\tau) \tag{4-17}$$

where β_0 is the magnetic momentum of the material. $g(\tau)$ is a temperature-dependent term and τ is expressed by

$$\tau = \frac{T}{T_{Cr}} \tag{4-18}$$

T_{Cr} is the Curie or Néel temperature of the material. [113]

4.3 Pure elements and stoichiometric compounds

Pure elements and stoichiometric compounds (STC) have a fixed chemical composition over their stability range. Therefore, their Gibbs energy is not composition-dependent, but depending on pressure and temperature. Pressure is usually considered to be atmospheric and is therefore kept constant at 1 atm. The Gibbs energy can be formulated as power series in temperature as follows.

$$G_m^\theta - \sum_i b_i H_i^{SER} = a_0 + a_1 T + a_2 T \ln(T) + a_3 T^2 + a_4 T^{-2} + a_5 T^3 + \dots \quad 4-19$$

b_i is a stoichiometric coefficient of the element i in the θ -phase and $\sum_i b_i H_i^{SER}$ is the sum of the enthalpies of the elements. *SER* denotes that elements are in standard element reference state at 298.15 K and 1 bar. The energies of pure elements can be found in the literature. [21],[103]

An alternative form of the Gibbs free energy of STC is given by

$$G = \Delta H_{298.15}^f + \int_{298.15}^T c_p dT - T[S_{298.15} + \int_{298.15}^T \frac{c_p}{T} dT] \quad 4-20$$

where $\Delta H_{298.15}^f$ is the standard enthalpy of formation and $S_{298.15}$ the standard entropy. Standard state is assumed to be 298.15 K. c_p is the heat capacity as a function of temperature. [110]

Properties of pure elements in this study are taken from Dinsdale [21] and the properties of binary iron-sulfides are directly taken from Waldner and Pelton [6]. As some slight changes in the model of MnS_2 phase were made, properties of this phase were taken from the work of Kang [2].

5 Results and discussion

The first part of this chapter deals with the interpretation of the experimental analysis performed by DSC. In the second part, the results of the thermodynamic optimization for Fe-Mn, Fe-C-Mn and Fe-Mn-S are discussed. Note that other assessments (Fe-C, Fe-S, Mn-C, C-S and Fe-Mn-C) were taken from available literature only.

5.1 Experimental investigation of high temperature phase equilibria

Initial comparison with existing thermodynamic databases (as can be seen in **Figure 3-1**) showed that the measured temperatures seem to be in good correlation with the calculations. The numerical values of measured phase transformation temperatures and the corresponding phase transformation reactions in the systems Fe-0.5%Mn-var%S and Fe-2%Mn-var%S are listed in **Table 5-1**.

Figure 5-1 shows the offset-corrected DSC signal in the low temperature range of selected alloys. The Curie temperature, T_{Curie} , is detectable by a small peak in the DSC signal and between 764 °C and 768 °C in the system Fe-0.5%Mn-var%S and between 745 °C and 751 °C in the system Fe-2%Mn-var%S. T_{Curie} slightly increases with rising amount of S. Further, with increasing content of Mn, the Curie temperature drops to lower values. During the low-temperature BCC-FCC phase transformation, the DSC signal is very small due to the minor heat change. Therefore, only the end of the phase transformation $T_{\alpha \rightarrow \gamma}^{\text{end}}$ can be evaluated by a peak in the DSC signal. Similar to T_{Curie} , the end of the BCC-FCC phase transformation $T_{\alpha \rightarrow \gamma}^{\text{end}}$ increases with higher amounts of S and decreases, the higher the Mn content is. In the Fe-S

binary sub-system, the phase transformation temperature remains constant until a mole fraction of S of approximately 0.5. [6] In contrary to that, the BCC-FCC phase transformation in the binary Fe-Mn sub-system decreases drastically with increasing amount of Mn in the Fe-rich side of the phase diagram. [86] This phenomenon can also be seen when comparing **Figure 5-1 a)** and **b)**.

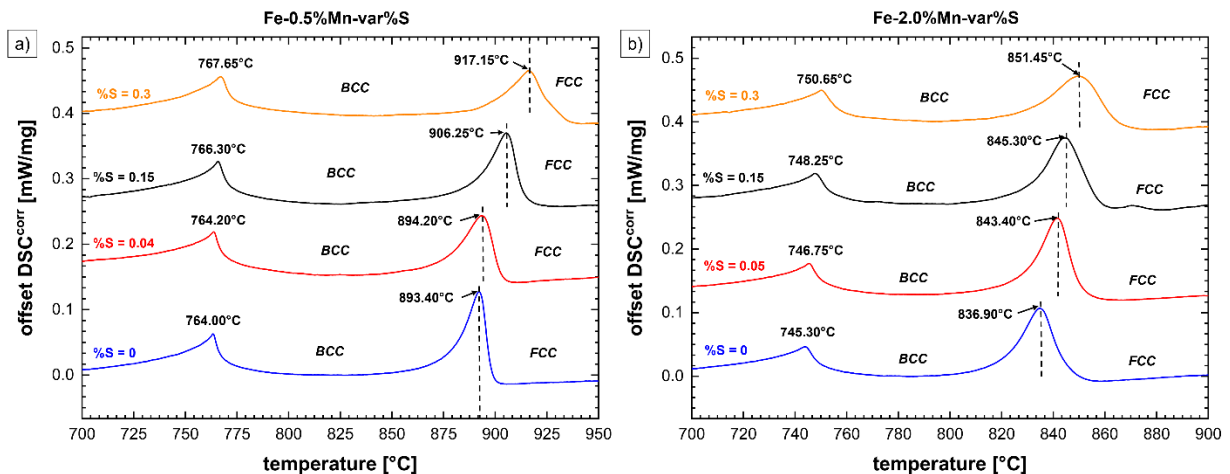


Figure 5-1: DSC signals of various samples in the system a) Fe-0.5%Mn-var%S between 700 °C and 950 °C and b) Fe-2%Mn-var%S between 700 °C and 900 °C showing Curie-temperature and low-temperature BCC-FCC phase transformation.

Figure 5-2 displays the DSC signals in the temperature region of the FCC-BCC transformation for both systems above 1370 °C and 1400 °C, respectively. In this case it is possible to evaluate the start and end of the phase transformation, $T_{\gamma \rightarrow \delta}^{\text{start}}$ and $T_{\gamma \rightarrow \delta}^{\text{end}}$ respectively. $T_{\gamma \rightarrow \delta}^{\text{start}}$ is marked by the first strong deviation of the baseline of the DSC, whereas $T_{\gamma \rightarrow \delta}^{\text{end}}$ is characterized by a very small “nose” on the descending signal line. The start temperature $T_{\gamma \rightarrow \delta}^{\text{start}}$ of the phase transition decreases drastically with increasing amount of S while it is increased with higher Mn contents. A similar result can be seen for the end of the phase transformation, $T_{\gamma \rightarrow \delta}^{\text{end}}$. Slight deviations from the trend may result from varying trace element contents in the sample alloys.

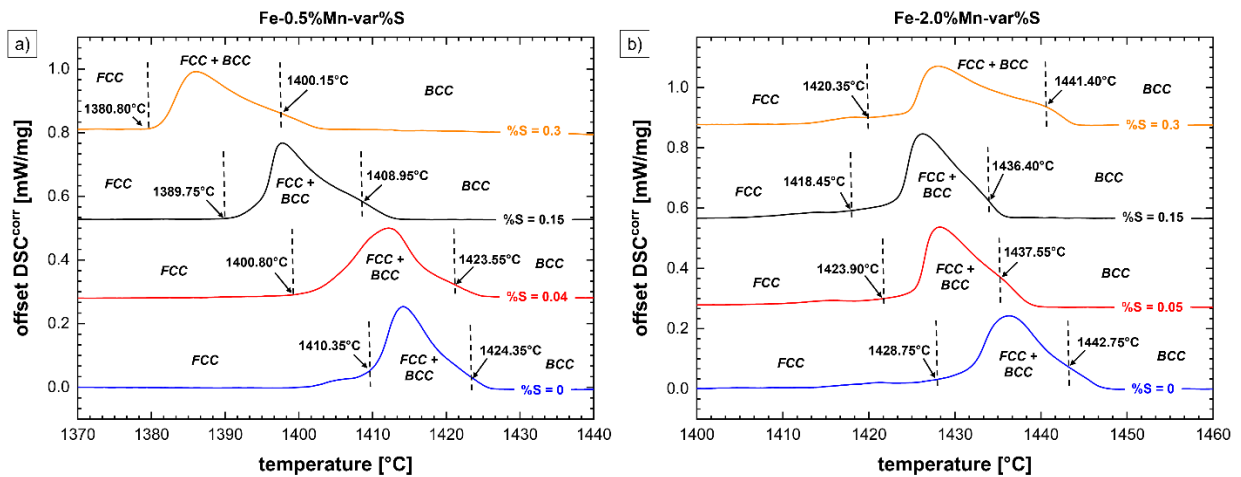


Figure 5-2: DSC signals of various samples in the system a) Fe-0.5%Mn-var%S between 1370 °C and 1440 °C and b) Fe-2%Mn-var%S between 1400 °C and 1460 °C showing start and end temperature of the high-temperature FCC-BCC phase transformation.

At temperatures above 1440 °C, several phase transformations occur. **Figure 5-3 a) - c)** shows the DSC signals at higher temperatures with all corresponding phase transformations measured. The solidus temperature T_{solid} can be detected by the first strong deviation of the baseline of the DSC signal. With increasing amount of S, T_{solid} decreases drastically in the system Fe-0.5%Mn-var%S. In contrary to that, the slope of T_{solid} in the Fe-2%Mn-var%S system is steep until approximately 0.015 wt.-% S and is very flat with increasing amount of S.

If sufficient amounts of Mn and S are present in the alloys, (Mn,Fe)S forms during heating and cooling of the steel. During DSC, the dissolution of (Mn,Fe)S can be detected by an emerging signal and was found to be the peak of the curve. A plausibility check has been carried out using TOA and more information can be found in the previous **Chapter 3.3**. The corresponding DSC signals are shown in **Figure 5-3 a) - c)**. The temperature at which (Mn,Fe)S dissolves is denoted as $T_{\text{MnS}}^{\text{end}}$ ($\text{BCC} + (\text{Mn,Fe})\text{S} + \text{Liquid} \leftrightarrow \text{BCC} + \text{Liquid}$) and is evaluated in the same manner as other phase transformation temperatures. In the system Fe-0.5%Mn-var%S, the temperature $T_{\text{MnS}}^{\text{end}}$ is about 30 °C lower than in the system Fe-2%Mn-var%S whereas in both systems, $T_{\text{MnS}}^{\text{end}}$ has constant values over the increasing S content within the standard deviation of the trials.

The melting temperature $T_{\text{liquid}}^{\delta}$ is detected by a peak of the DSC signal and is found to be decreasing with increasing amounts of S and Mn. During solidification, BCC is the primary phase for all alloys used in this study and no austenite occurs.

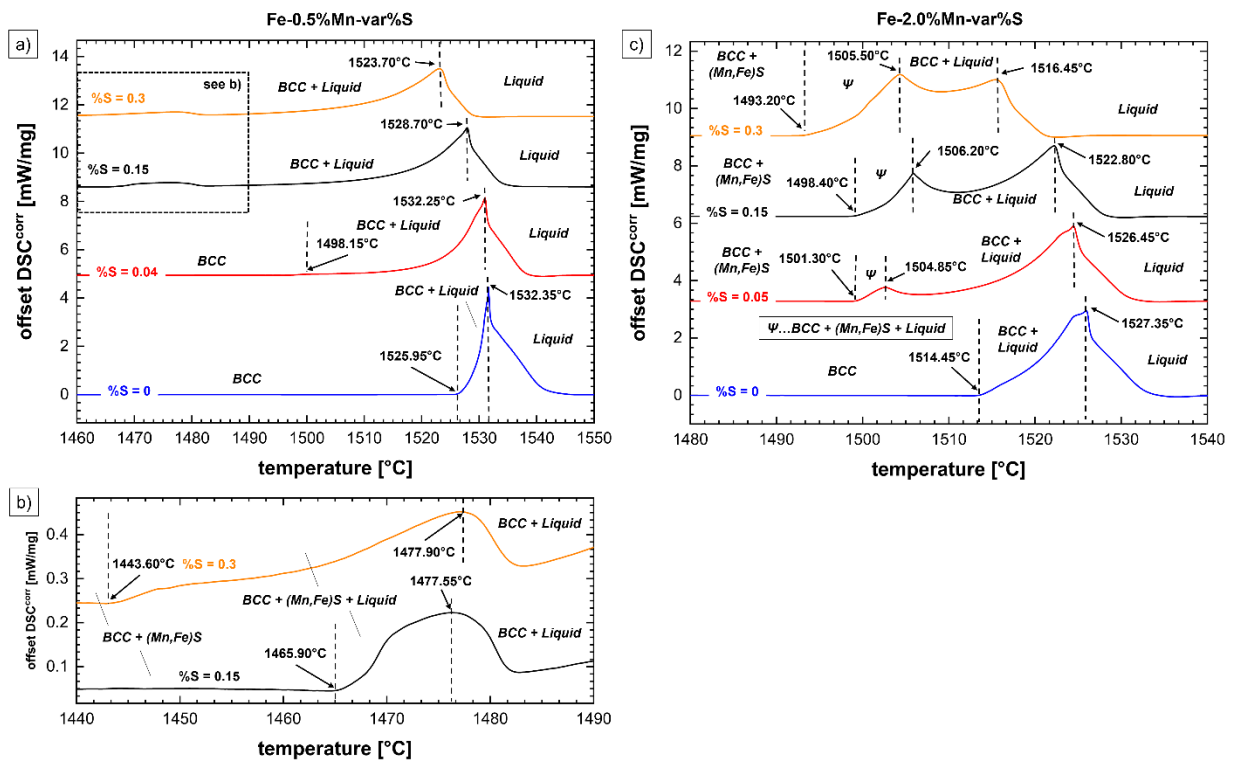


Figure 5-3: DSC signals of various samples in the systems a) Fe-0.5%Mn-var%S between 1460 °C and 1550 °C, b) Fe-0.5%Mn-var%S between 1440 °C and 1490 °C and c) Fe-2%Mn-var%S between 1480 °C and 1540 °C showing solidus temperature, dissolution temperature of (Mn,Fe)S and melting temperature.

Table 5-1: Phase transformation temperatures obtained by DSC for the systems Fe-0.5%Mn-var%S and Fe-2%Mn-var%S (n.p.: no phase transformation according to DSC).

System	Alloy	S	C	Mn	T _{Curie} [°C]	T _{α→γ} ^{end} [°C]	T _{γ→δ} ^{start} [°C]	T _{γ→δ} ^{end} [°C]	T _{solid} [°C]	T _{MnS} ^{end} [°C]	T _{liquid} ^δ [°C]
		[wt.-%]			/	α + γ → γ	γ → γ + δ	γ + δ → δ	δ → L + δ	/	L + δ → L
Fe-0.5%Mn-var%S	A-I	0.0021	0.0197	0.52	764.00	893.40	1410.35	1424.35	1525.95	<i>n.p.</i>	1532.35
	A-II	0.0121	0.0148	0.52	764.35	898.05	1400.70	1420.15	1520.25	<i>n.p.</i>	1534.45
	A-III	0.0261	0.0132	0.51	764.70	901.70	1397.40	1414.95	1511.45	<i>n.p.</i>	1533.65
	A-IV	0.0417	0.0195	0.51	764.20	894.20	1400.80	1423.55	1498.15	<i>n.p.</i>	1532.25
	A-V	0.0944	0.0203	0.51	766.05	901.95	1392.15	1411.85	1473.45	1478.30	1531.05
	A-VI	0.1523	0.0130	0.50	766.30	906.25	1389.75	1408.95	1465.90	1477.55	1528.70
	A-VII	0.1930	0.0175	0.48	766.45	906.45	1389.40	1409.65	1460.15	1476.20	1526.95
	A-VIII	0.2370	0.0162	0.47	767.25	908.90	1386.45	1408.10	1451.90	1476.40	1525.40
	A-IX	0.3047	0.0125	0.47	767.65	917.15	1380.80	1400.15	1443.60	1477.90	1523.70
Fe-2.0%Mn-var%S	B-I	0.0025	0.0191	1.98	745.30	836.90	1428.75	1442.75	1514.45	<i>n.p.</i>	1527.35
	B-II	0.0082	0.0190	1.97	746.15	841.90	1426.10	1443.10	1510.90	<i>n.p.</i>	1528.15
	B-III	0.0145	0.0201	1.97	745.90	840.45	1427.65	1441.75	1506.60	<i>n.p.</i>	1527.40
	B-IV	0.0514	0.0155	1.94	746.75	843.40	1423.90	1437.55	1501.30	1504.85	1526.45
	B-V	0.1487	0.0178	1.93	748.25	845.30	1418.45	1436.40	1498.40	1506.20	1522.80
	B-VI	0.2053	0.0219	1.90	749.35	848.75	1423.45	1442.45	1495.15	1504.60	1519.80
	B-VII	0.3077	0.0209	1.88	750.65	851.45	1420.35	1441.40	1493.20	1505.50	1516.45

5.2 Optimizations in the systems Fe-Mn, Fe-Mn-C and Fe-Mn-S

In **Chapter 2.3**, several thermodynamic assessments of the systems Fe-Mn, Fe-Mn-C and Fe-Mn-S are discussed. From these publications, thermodynamic databases can be created using the published model parameters. Although there are numerous databases available, in some systems, there is still a need for thermodynamic re-modeling and optimization. In the present study, the binary system Fe-Mn and the ternary systems Fe-Mn-C and Fe-Mn-S are modeled based on own measurements at the Chair of Ferrous Metallurgy conducted by Presoly [114] (Fe-Mn and Fe-Mn-C) and in the present work (Fe-Mn-S), consideration of extensive literature data. The systems Fe-Mn and Fe-Mn-C are of high priority in the present work, as the accuracy of the binary Fe-Mn system largely affects the calculations of all ternary systems (Fe-Mn-C, Fe-Mn-S). Further, a non-negligible content of trace Carbon is detected in the samples of the ternary system Fe-Mn-S. Therefore, the modeling of this system has to be carried out under attention of the trace C content and the modeling of the System Fe-Mn-C is required.

Parameters in the systems Fe-Mn, Fe-Mn-C and Fe-Mn-S are varied until the discrepancies between experimental data and calculation are minimized. As the previous descriptions of these systems are already in good accordance with the experimental data obtained from this study, only slight changes have been carried out. The most significant changes are made in the binary system Fe-Mn and Fe-Mn-C. **Table 5-2** compares parameters of existing models, which are used as a start value, with optimized parameters for the present work. In total, four parameters are optimized in the binary system (Liquid, FCC, BCC, CBCC) and two in the ternary system Fe-Mn-C (Liquid, FCC). The combination of the optimized parameters with other, already existing parameters, pose a model with good agreement of experimental data and calculation. The complete database for the quaternary Fe-Mn-C-S system is given in the appendix.

Table 5-2: Comparison between previous (start) parameters and optimized parameters. Start parameters are taken from Kim and Kang [3]

Phase	Start parameter [3] [J/mol]	Optimized parameter [J/mol]
Liquid	$\Delta g_{\text{FeMn}} = -1338.9 + 0.17T$ $+ 418.4X_{\text{FeFe}} - 334.7X_{\text{MnMn}}$	$\Delta g_{\text{FeMn}} = -1380.72 + 0.134T$ $+ 753.62X_{\text{FeFe}} - 586.15X_{\text{MnMn}}$
	$\Delta g_{\text{Fe,Mn(C)}} = -8368 + 9623X_{\text{MnMn}}$	$\Delta g_{\text{Fe,Mn(C)}} = -8368$
FCC	$L_{\text{Fe,Mn:Va}} = -7762 + 3.87T$ $- 259(y'_{\text{Fe}} - y'_{\text{Mn}})$	$L_{\text{Fe,Mn:Va}} = -5020.8 + 1.883T$
	$L_{\text{Fe,Mn:C}} = -836.8$	$L_{\text{Fe,Mn:C}} = 0$
BCC	$L_{\text{Fe,Mn:Va}} = -2759 + 1.24T$	$L_{\text{Fe,Mn:Va}} = -4184 - 1.715T$
CBCC	$L_{\text{Fe,Mn:Va}} = -10184$	$L_{\text{Fe,Mn:Va}} = -9414$

5.2.1 The binary system Fe-Mn and the ternary system Fe-Mn-C

In a recent investigation at the Chair of Ferrous Metallurgy (Montanuniversität Leoben), the Fe-Mn system was experimentally reassessed up to 40 wt.-% Mn using Differential Thermal Analysis (DTA). [114] It is highest priority of the present work to improve the calculation results for those data in consistency with observations from the literature. However, the trace carbon content in the laboratory samples is comparably high (~ 0.017 wt.-%). Therefore, the investigation of Presoly [114] (Fe-Mn) has to be seen as ternary system Fe-Mn-C with very low amount of carbon, further denoted as Fe-Mn-C^{low}. Nevertheless, because of the low amount of carbon, optimizations in this system give very reasonable conclusions about the binary Fe-Mn system.

Thermodynamic properties of the binary Fe-Mn melt (without C) are shown in **Figure 5-4 a)** and **b)**. The calculated integral enthalpy of mixing of liquid Fe-Mn alloys at 1600 °C is in good accordance with literature data, although it must be noted that the experimental data obviously scatters. The calculations of Huang [85] and Kim and Kang [3] are exactly the same, although the description of the Fe-Mn liquid phase of Huang is based on a Bragg-Williams regular

solution model, whereas Kim and Kang used the MQM. The calculated activity of liquid Mn in the Fe-Mn melt is in acceptable agreement with literature data. Again, experimental data scatters strongly. Compared to the integral enthalpy of mixing, the difference in the activity compared with the results of Huang [85], Witusiewicz [67] or Kim and Kang [3] is not significant.

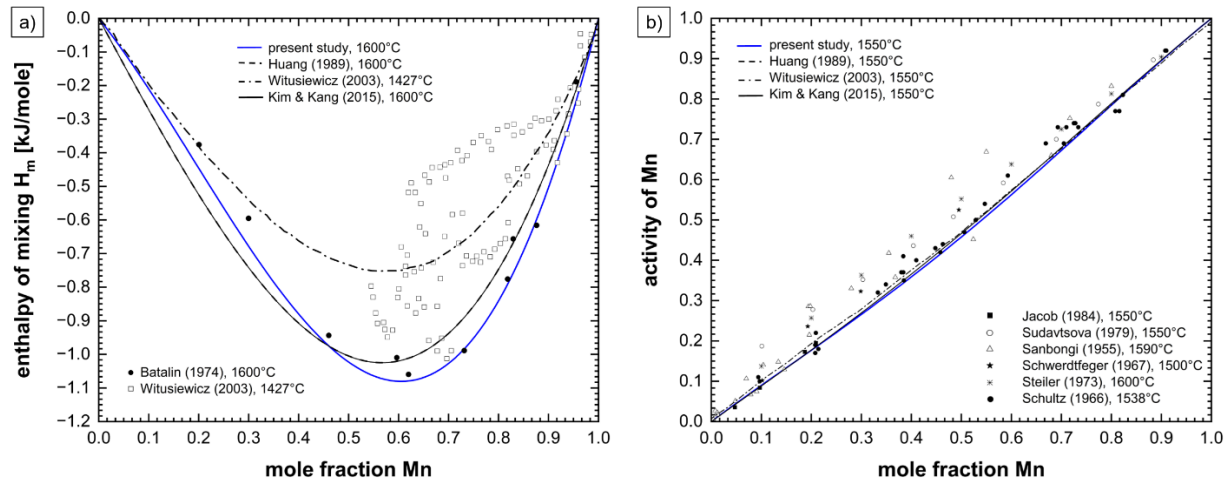


Figure 5-4: Calculated thermodynamic properties in the binary system Fe-Mn compared to the database of Huang [85], Witusiewicz et al. [67], Kim and Kang [3], shown by a) the integral enthalpy of mixing at 1600 °C compared to experimental data from references [50] and [67] and b) the activity of Mn at 1550 °C compared to experimental data from references [57]–[62]. Calculations performed with FactSage 8.2 [10].

Figure 5-5 shows the calculated Fe-Mn-C^{low} system considering 0.017 wt.-% C in the temperature range of 0 °C to 1700 °C. The system is in good agreement with experimental data from literature over the total temperature range. Slight deviations might result from measurements performed several decades ago and slight differences in the chemical compositions.

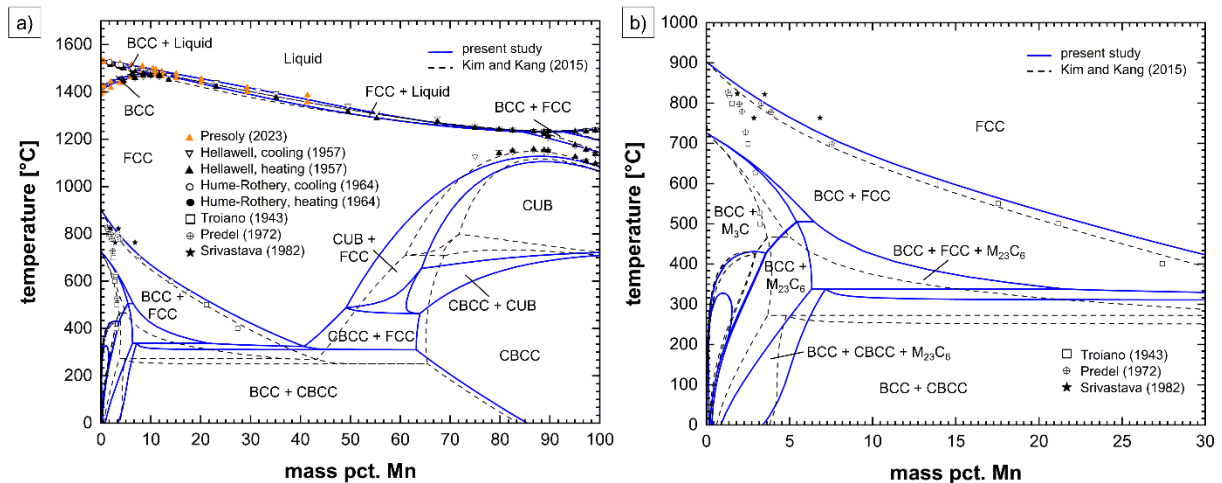


Figure 5-5: The system Fe-var%Mn-0.017%C a) up to 100 wt.-% Mn and 1700 °C and b) up to 30 wt.-% Mn and 1000 °C compared to the database of Kim and Kang [3] and experimental data from Presoly [114] (DTA) and from references [47]–[49],[63],[64]. Calculation performed with FactSage 8.2 [10].

Figure 5-6 shows the ternary system Fe-Mn-C^{low} at elevated temperatures with up to 100 wt.-% Mn. The calculation is compared to a previous model by Kim and Kang [3] as well as literature data from Hellawell and Hume-Rothery [48]. Compared to the previous database, a higher liquidus temperature up to 60 wt.-% Mn is measured. Therefore, the parameter for the ternary and binary liquid phase in the MQM is set less negative to destabilize the liquid phase. The calculation is now in better agreement with experimental data due to optimizations of the Liquid, BCC and FCC parameter of the system Fe-Mn. Slight optimizations are made in the Fe-rich corner in the two-phase region between FCC and BCC, assuming the BCC phase to be more stable.

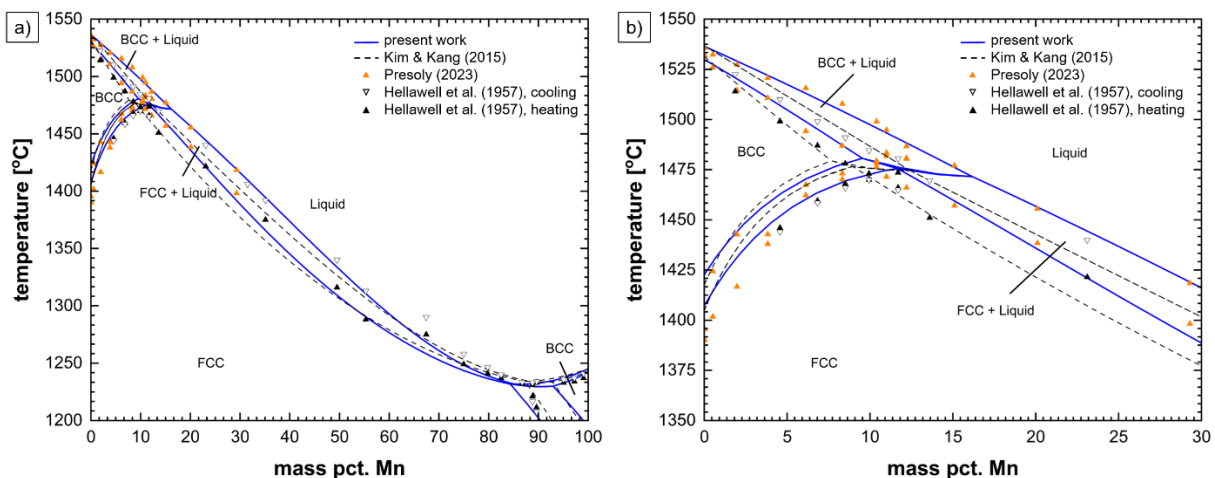


Figure 5-6: Phase diagram of the system Fe-Mn-C^{low} at high temperatures with a trace C content of 0.017 wt.-% C a) up to 100 wt.-% Mn and b) up to 30 wt.-% Mn compared to the calculation of Kim

and Kang [3] and experimental data from Presoly [114] (DTA) and reference [48]. Calculation performed with FactSage 8.2 [10].

After optimization in the Fe-Mn-C^{low} system, systems with higher carbon content are re-assessed. **Figure 5-7** shows the phase diagram of Fe-10%Mn with varying carbon content up to 10 wt.-% at higher temperatures. The previous model is already in reasonable accordance with the measured data, although the calculation could not predict the peritectic reaction which occurs at low amount of C. Due to a stabilizing BCC parameter in the CEF, the peritectic region, which is obviously present in these alloys, can now be calculated. Only minor deviations from measured temperatures (± 5 °C) are observed in this case.

The present model is also in good accordance with experimental data at higher Mn contents. **Figure 5-8** shows the system Fe-20%Mn with up to 10 wt.-% C. The model is compared to a previous database by Kim and Kang [3] and experimental data from Presoly [114] and Schürmann and Geissler [80]. Optimizations have been made in the high temperature Fe-rich side in terms of liquidus temperature. According to the calculation and compared to the system Fe-10%Mn-var%C in **Figure 5-7**, no peritectic region is present.

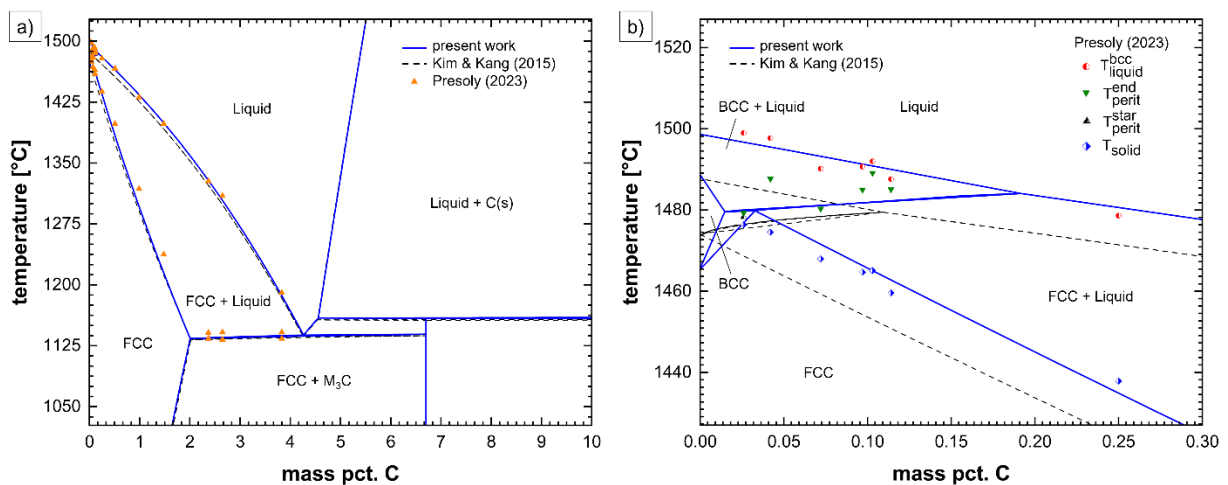


Figure 5-7: Phase diagram of the ternary system Fe-10%Mn-var%C a) up to 10 wt.-% C and b) in the Fe-rich peritectic corner at high temperature compared to the calculation of Kim and Kang [3] and experimental data from Presoly [114] (DTA). Calculation performed with FactSage 8.2 [10].

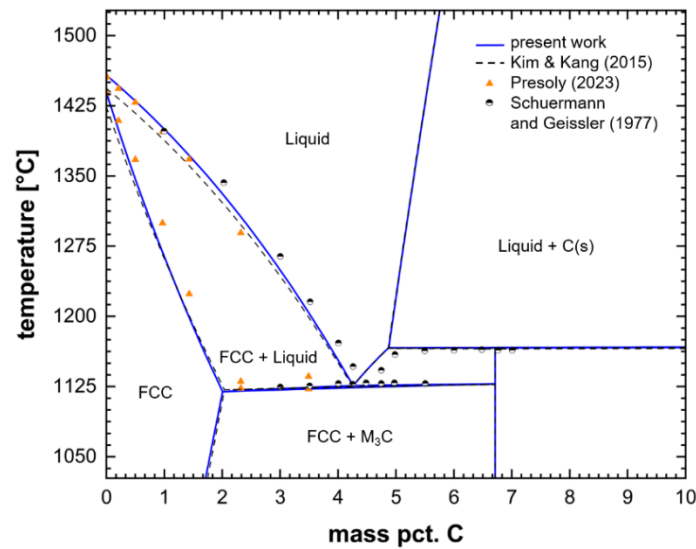


Figure 5-8: Phase diagram of the system Fe-20%Mn-var%C up to 10 wt.-% C compared to the calculation of Kim and Kang [3] and experimental data from Presoly [114] (DTA) and reference [80]. Calculation performed with FactSage 8.2 [10].

The solubility of carbon in liquid and solid alloys is of high relevance for the steel industry and was therefore studied extensively in the literature [34],[69],[71]–[73],[115],[116]. The solubility of carbon in the ternary alloy Fe-Mn-C at saturation of graphite with respect to temperature is shown in **Figure 5-9**. As expected, the solubility of C in the liquid increases, but decreases at higher amount of Fe. For all temperatures, excellent agreement with the experimental data is observed, but a significant improvement to the previous work Kim and Kang [3] is not evident.

Figure 5-10 a) displays the carbon solubility in liquid Fe-Mn-C alloys at 1450 °C with respect to the carbon potential in the atmosphere. The higher the carbon potential in the atmosphere, expressed as partial pressure of carbon monoxide p_{CO} , the higher the solubility of carbon. **Figure 5-10 b)** shows the temperature and carbon potential dependency of the solubility of carbon in liquid Fe-Mn-C alloys. The results of the calculations are in very good agreement with literature data. The results regarding the thermodynamics of solubility of carbon in liquid alloys in **Figure 5-9** and **Figure 5-10** agree with each other.

Iso-activity lines are calculated with the present model and compared to the previous description in **Figure 5-11 a) to c)**. There exists some mismatch between the present calculations and the literature data but the calculations follow the trend of the experimental data. Further, the decrease of activity of manganese by increasing the carbon content can be calculated with the present model. Obviously, also the prediction of Kim and Kang [3] differs in this case from the literature data.

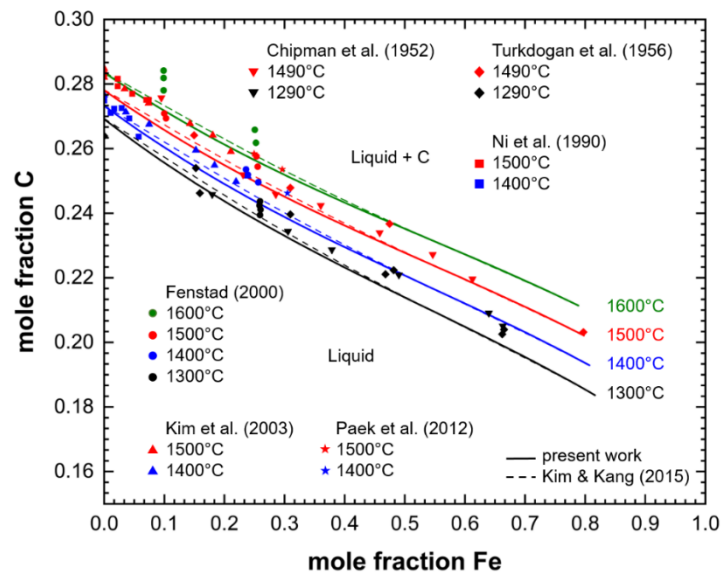


Figure 5-9: Calculated solubility of C in liquid Fe-Mn-C alloy at various temperatures compared to the calculation of Kim and Kang [3] and experimental data from references [69]–[73],[115]. Calculation performed with FactSage 8.2 [10].

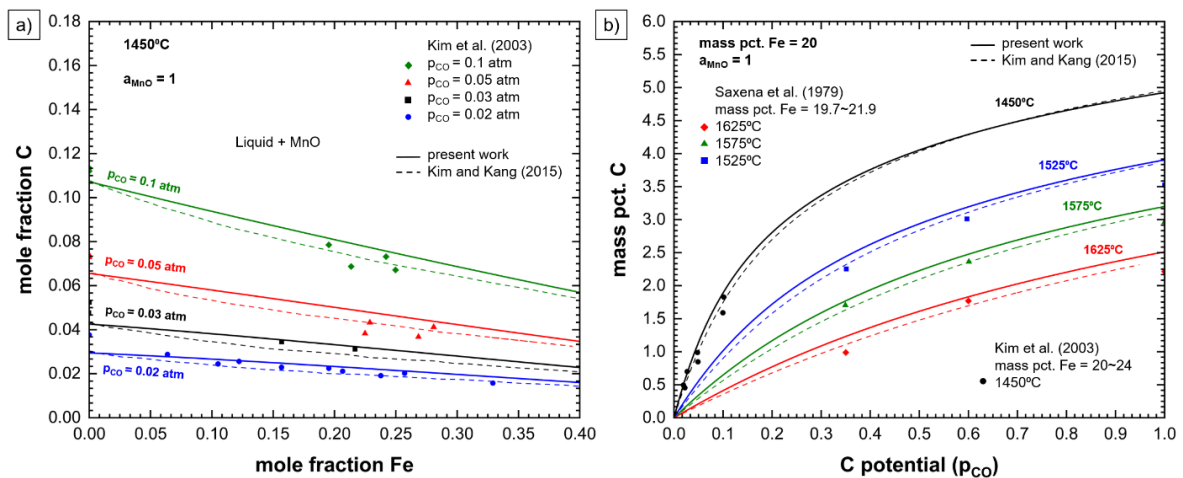


Figure 5-10: Calculated solubility of C in liquid Fe-Mn-C alloy in equilibrium with CO in gaseous phase and saturated with solid MnO a) under various partial pressures at 1450 °C and b) at various temperatures, compared to the calculation of Kim and Kang [3] and experimental data from references [69],[116]. Calculation performed with FactSage 8.2 [10].

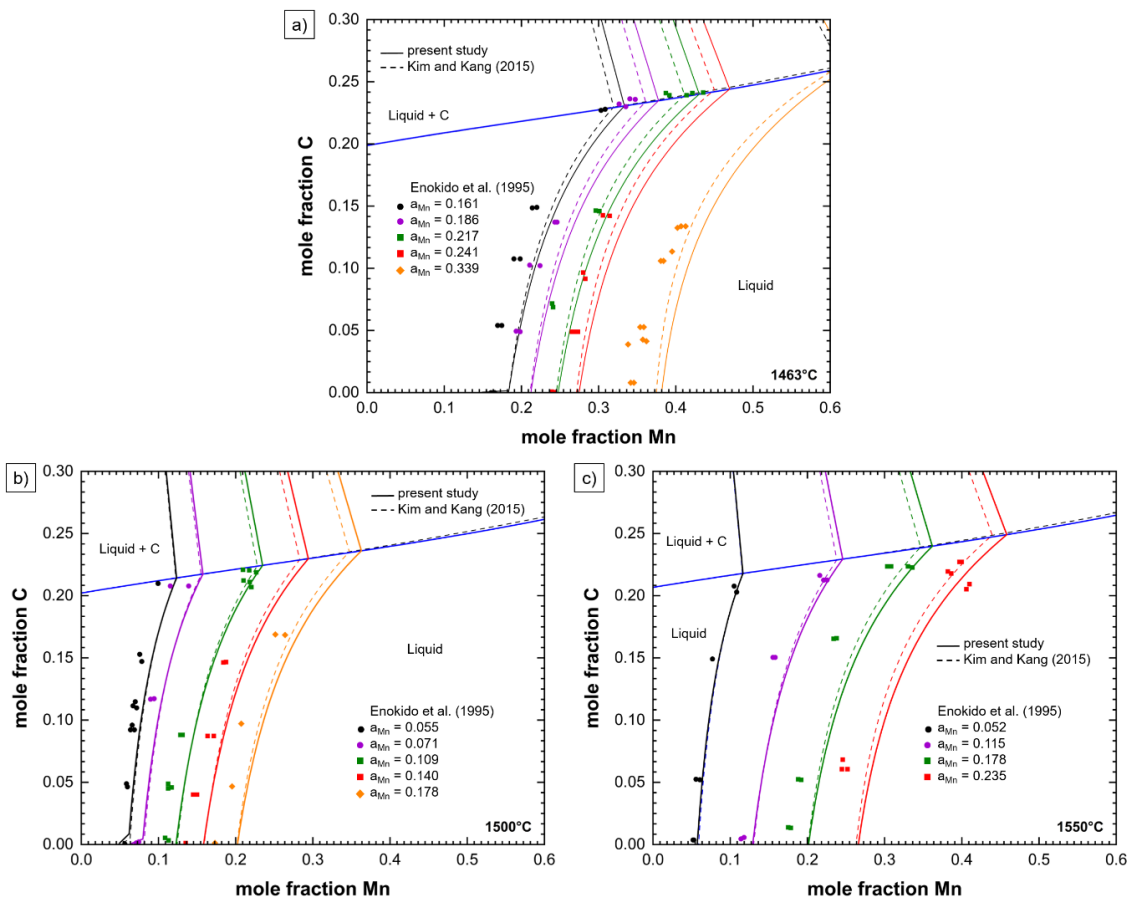


Figure 5-11: Calculated iso-activity lines of Mn in liquid Fe-Mn-C alloy at various temperatures, a) 1463 °C, b) 1500 °C and c) 1550 °C, compared to the calculation of Kim and Kang [3] and experimental data from reference [74]. Calculation performed with FactSage 8.2 [10].

To give a complete overview of the system Fe-Mn-C, also solid solutions, and phases are investigated and compared to literature data. **Figure 5-12** shows phase diagrams in the ternary system Fe-Mn-C at 690 °C, 910 °C and 1050 °C. At these temperatures, carbide phases are stable together with solid solutions of Fe, Mn and C. Comparison to other databases are omitted in this case. The calculations are in good accordance with experimental data from the literature and parameters for carbide phases are not optimized in this model because of their profound description in previous databases. Nevertheless, it must be noted that in the present model, there are some deviations on the left-hand side of the phase diagram in **Figure 5-12 a)** compared to the database of Kim and Kang [3]. Even there are no experimental data available, some further work on the optimization of the description of these parameters might improve the calculations.

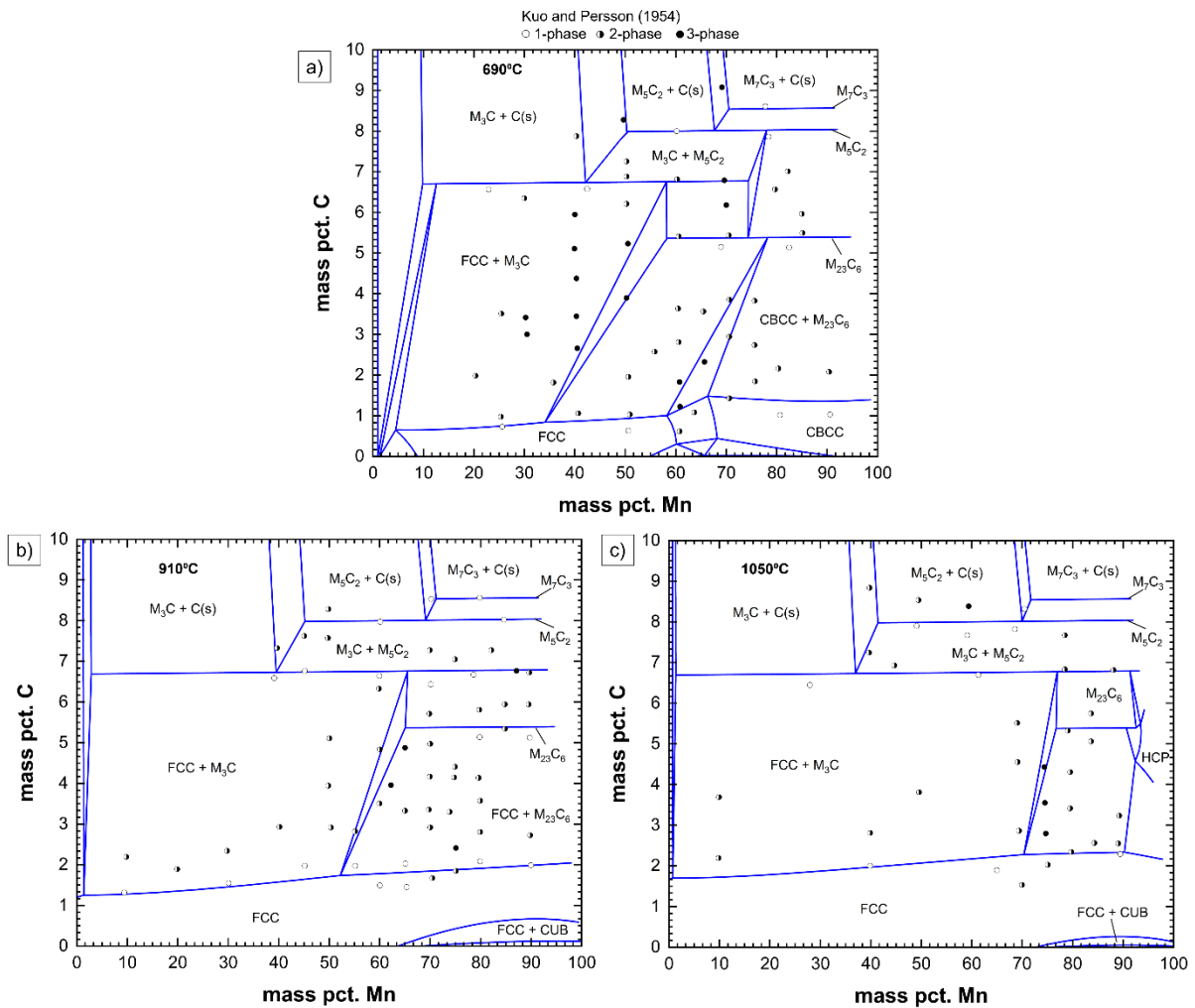


Figure 5-12: Calculated phase diagrams in the system Fe-Mn-C at a) 690 °C, b) 910 °C and c) 1050 °C with stable carbide phases, compared to experimental data from reference [75]. Calculation performed with FactSage 8.2 [10].

5.2.2 The ternary system Fe-Mn-S

The main goal of the present study is the experimental investigation and subsequent thermodynamic assessment of the system Fe-Mn-S. As high trace C contents are present in the laboratory samples, also this system has to be recognized as Fe-Mn-S-C^{low}. Two systems, Fe-0.5%Mn-var%S and Fe-2%Mn-var%S with an average trace Carbon content of 0.0176 wt.-% are investigated by DSC. If C is present in trace levels, the multicomponent calculations for Fe-Mn-S-C^{low} have to be performed with the commercial database FSStel (2022) from FactSage thermochemical software. In case of ternary Fe-Mn-S, as proposed in the literature, the database of Kang [2] was used for comparison.

Figure 5-13 shows the high temperature section of the system Fe-0.5%Mn-var%S-0.0176%C along with experimental data obtained in the present work. The calculation is compared to a model of Kang [2] and it can be seen that the previous model is already in good accordance with the experimental data. Slight changes of the Fe-Mn BCC parameter optimized the calculated solidus temperature. As the 3-phase region FCC-BCC-(Mn,Fe)S is strongly dependent on the C content, it is very important to take C into account for this model.

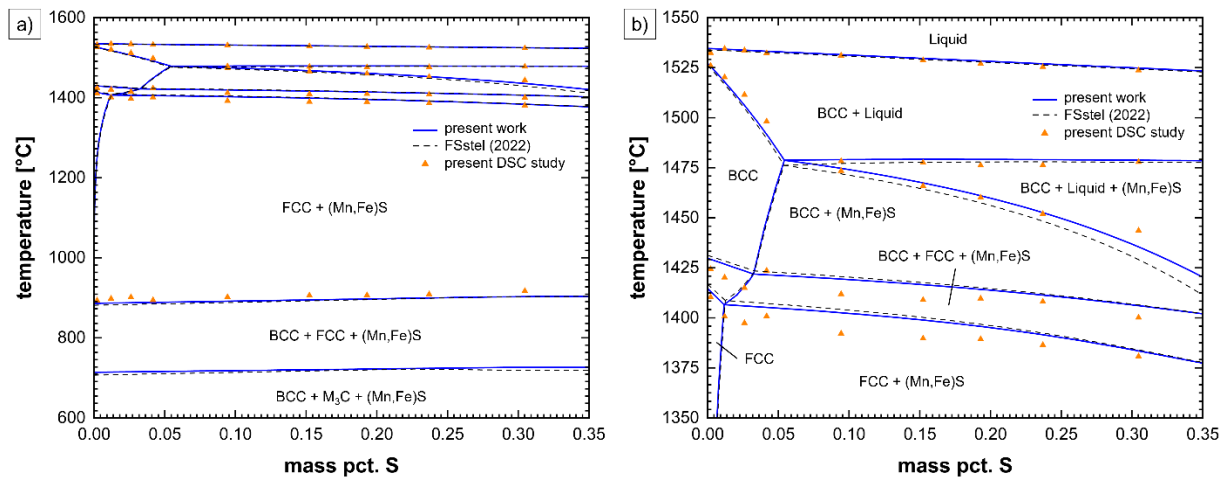


Figure 5-13: Calculated phase diagram of the system Fe-0.5%Mn-var%S-0.0176%C with up to 0.35 wt.-% S compared to the FSstel (2022) database and experimental data from this present study.

Calculation performed with FactSage 8.2 [10].

Figure 5-14 shows the section Fe-2%Mn-var%S-0.0176%C up to 0.35 wt.-% S. Again, the previous model is in good accordance with the measured phase transformation temperatures. Optimizations are made in the Fe-rich corner at high temperatures, slightly increasing the calculated liquidus temperature by making the liquid phase less stable. The 3-phase region BCC-Liquid-(Mn,Fe)S is optimized according to the measured temperatures by making the BCC parameter of the binary system Fe-Mn more stable. Also, the previous model shows strong deviations in the 3-phase region FCC-BCC-(Mn,Fe)S. By optimizing the BCC parameter, this phase field is now in good agreement with the measured data.

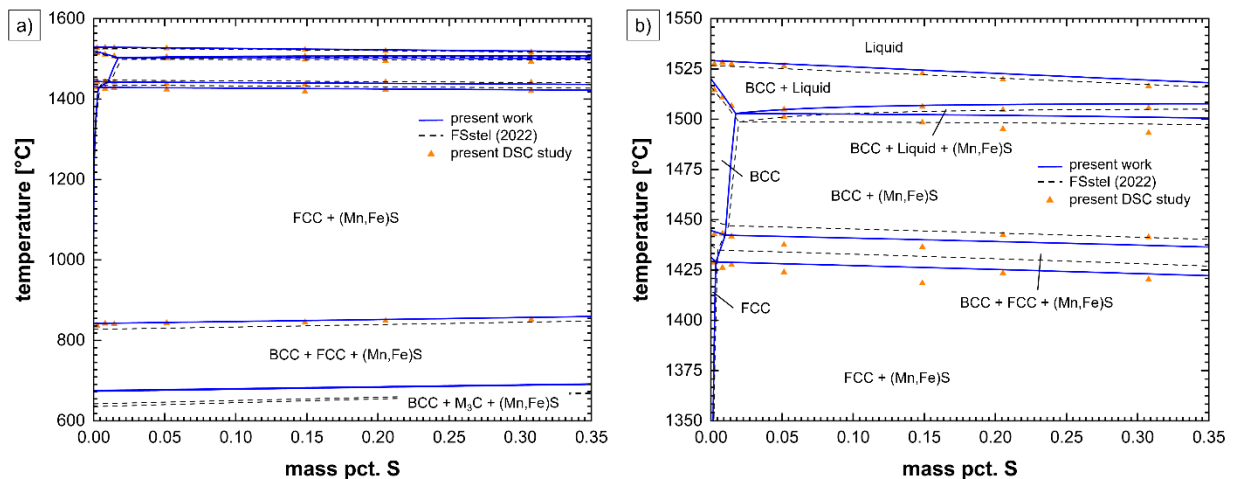


Figure 5-14: Calculated phase diagram of the system Fe-2%Mn-var%S-0.0176%C with up to 0.35 wt.-% S compared to the FSstel (2022) database and experimental data from this present study.

Calculation performed with FactSage 8.2 [10].

However, when it comes to the sections in **Figure 5-13** and **Figure 5-14**, there are some noticeable deviations between the calculations and the experimental data. This error is not only caused by the thermodynamic model, but also by the different C content in the alloys. It is well known that the C content has a huge impact on the BCC-FCC phase equilibria. The sections in **Figure 5-13** and **Figure 5-14** are calculated using average chemical compositions. The exact compositions regarding C, S and Mn can be seen in **Table 3-2** and **Table 3-3**. **Figure 5-15** compares the calculated and the measured FCC-BCC phase equilibria in the sections with 0.5 wt.-% and 2 wt.-% Mn with respect to the exact chemical composition for every alloy. There is a small systematic deviation in both systems, where in most cases the calculated temperatures are higher than the measured temperatures, resulting from the thermodynamic model assuming the phase transformation temperature slightly too high. However, most of the calculations differ less than ± 5 °C, which represents the typical error bar in the DSC analysis.

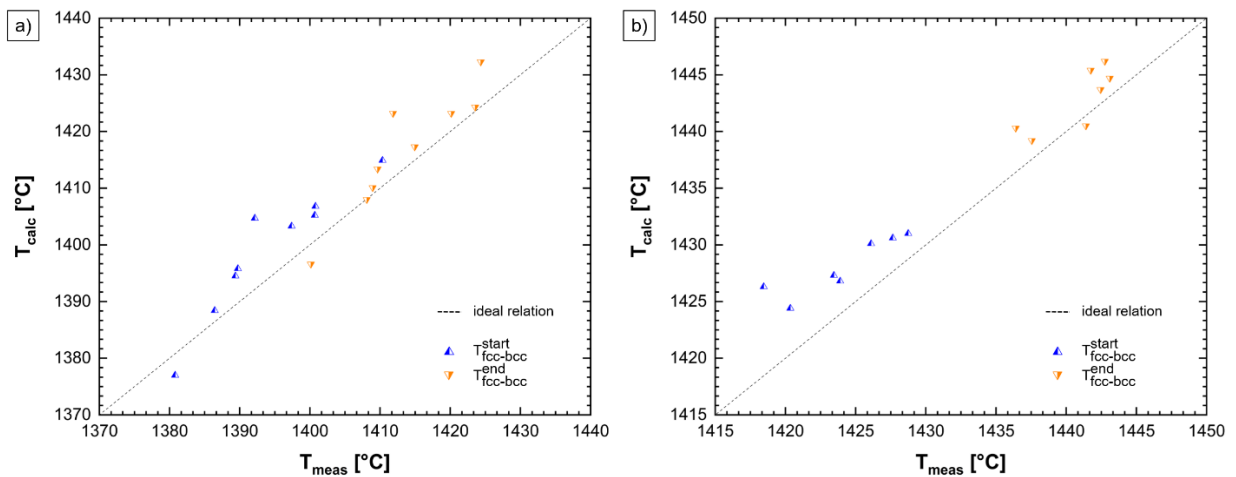


Figure 5-15: Comparison between calculated and measured FCC-BCC phase transformation temperatures in the systems with a) 0.5 wt.-% Mn and b) 2 wt.-% Mn using the exact chemical composition for every sample and the thermodynamic model of the present study.

The ternary system Fe-Mn-S at 1300 °C and 1600 °C is calculated as exemplary shown in **Figure 5-16**. Experimental data is in acceptable agreement with the calculation. **Figure 5-16 b)** shows experimental data by Dashevsky and Kashin [44] in the Mn rich corner of the ternary system.

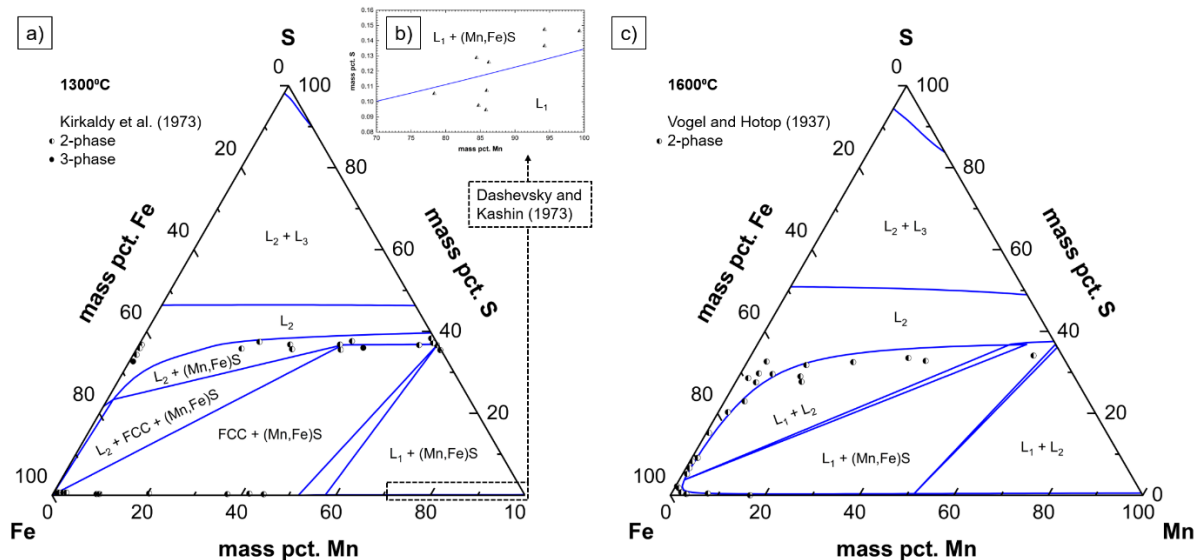


Figure 5-16: Ternary phase diagrams of the system Fe-Mn-S at a) 1300 °C compared to experimental data of reference [41], b) 1300 °C in the Mn-rich corner compared to experimental data of reference [44] and c) 1600 °C compared to experimental data of reference [31]. Calculation performed with FactSage 8.2 [10].

The solubility of S in liquid Fe-Mn-S alloys has been measured by researchers [29]–[34],[117],[118]. **Figure 5-17** displays the equilibrium of liquid Fe-Mn-S melts with gaseous S_2

at various partial pressures at 1600 °C. Under constant S_2 potentials, $p(S_2)$, the solubility of S increases with increasing Mn content. This phenomenon is caused by the strong attraction between Mn and S in liquid Fe. The experimentally obtained data is in reasonable agreement with the calculation. Compared to the calculation of Kang [2], no major improvement or deviation to the present model is obvious.

Figure 5-18 a) to d) demonstrates the solubility of S in liquid Fe-Mn-S alloys at various temperatures between 1550 °C and 1615 °C. The calculation is in good accordance with experimental data and the deviation between the calculations of Kang [2] and the present model is only marginal. Experimental data might scatter due to the experiments and temperature loss during sampling. Nevertheless, some deviations between calculation and experimental data are noticeable in the S-rich corner.

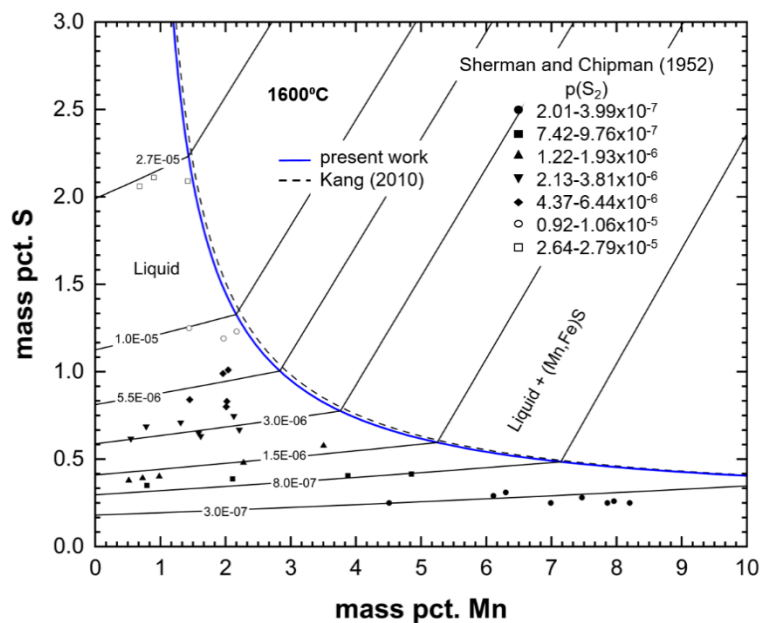


Figure 5-17: Calculated solubility of S in liquid Fe-Mn alloy in equilibrium with S_2 in gas phase at various partial pressures $p(S_2)$ at a temperature of 1600 °C compared to the calculation of Kang [2] and experimental data of reference [34]. Calculation performed with FactSage 8.2 [10].

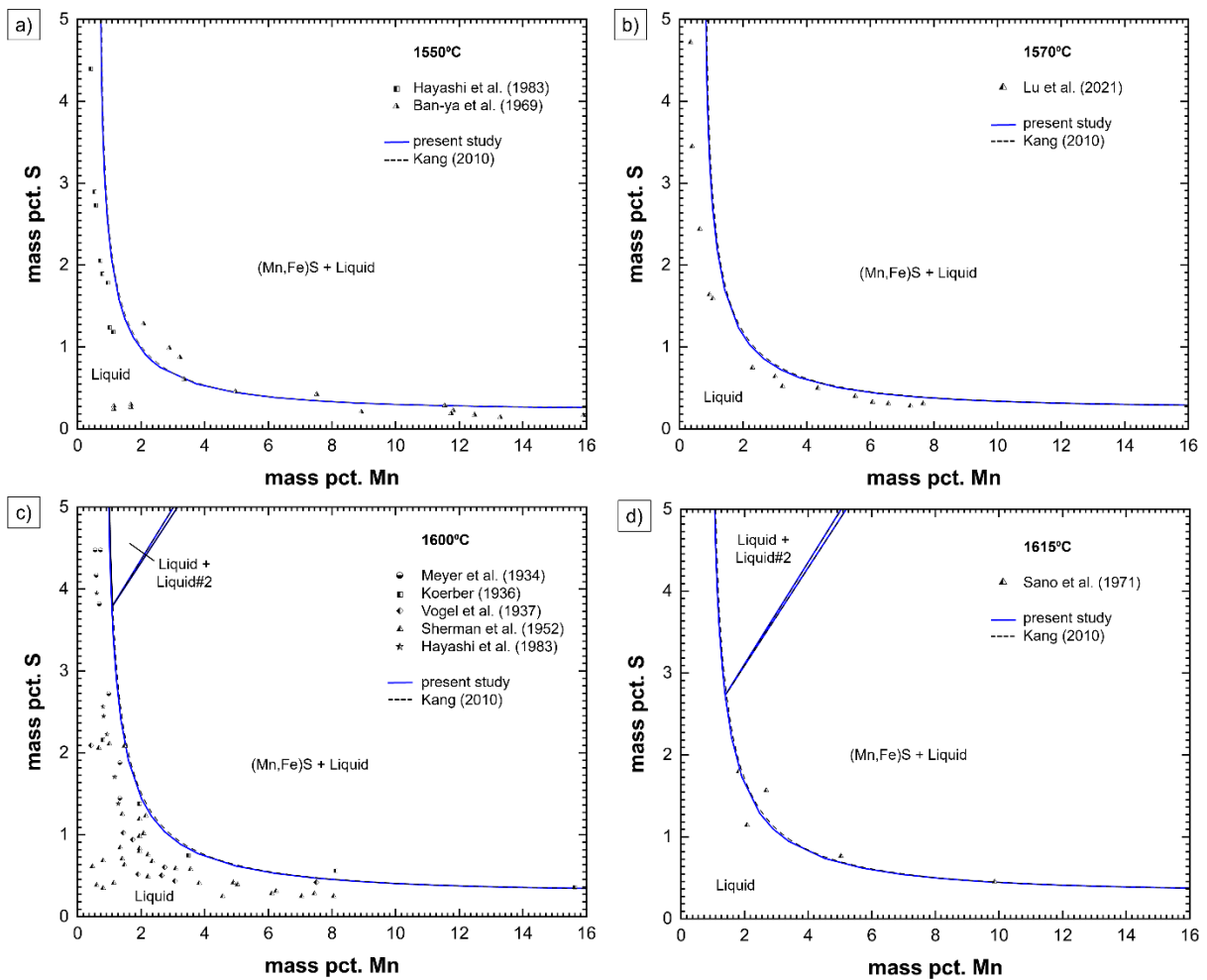


Figure 5-18: Calculated solubility of (Mn,Fe)S in liquid Fe-Mn-S alloys compared to the calculation of Kang [2] at a) 1550 °C compared to experimental data from references [33],[117], b) 1570 °C compared to experimental data from reference [29], c) 1600 °C compared to experimental data from references [31],[32],[34],[117],[118] and d) 1615 °C compared to experimental data from reference [30]. Calculation performed with FactSage 8.2 [10].

For the solid state, measurements of activity of S and the solubility of S have been conducted [12],[30],[35],[119]. **Figure 5-19** demonstrates the calculated activity of gaseous S, expressed as $\log(p(\text{H}_2\text{S})/p(\text{H}_2))$, at various temperatures over solid FCC Fe-Mn alloy. Experimental data is mostly in good agreement with the calculation.

The solubility of S in FCC Fe-Mn alloy decreases with increasing Mn content as the activity of S decreases too. **Figure 5-20** expresses the calculated solubility of S in FCC phase in equilibrium with (Mn,Fe)S phase at various temperatures compared to the calculation of Kang [2]. The calculation is not in perfect agreement with experimental data as those data scatter strongly, but the correct trend of the solubility of S in FCC alloy is evident by the calculation.

Only very slight deviations of the present model and the calculation of Kang [2] are evident in both diagrams.

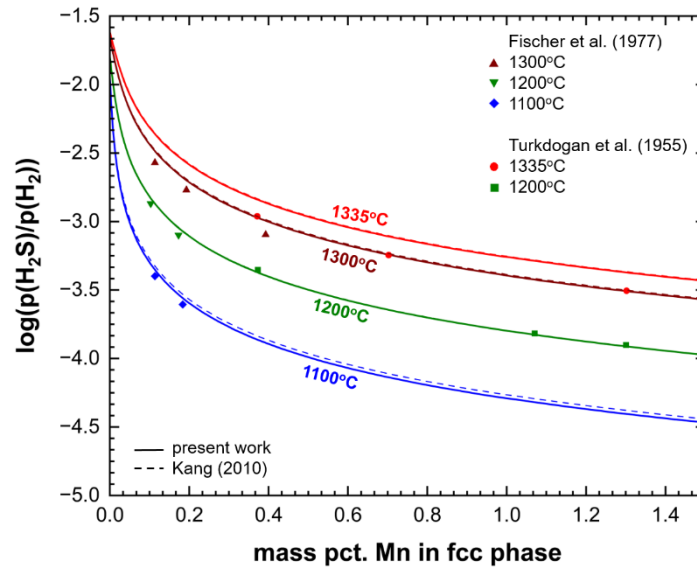


Figure 5-19: Calculated activity of S expressed as ratio $p(\text{H}_2\text{S})/p(\text{H}_2)$ over Mn in FCC phase at different temperatures compared to the calculation of Kang [2] and experimental data from references [12],[35]. Calculation performed with FactSage 8.2 [10].

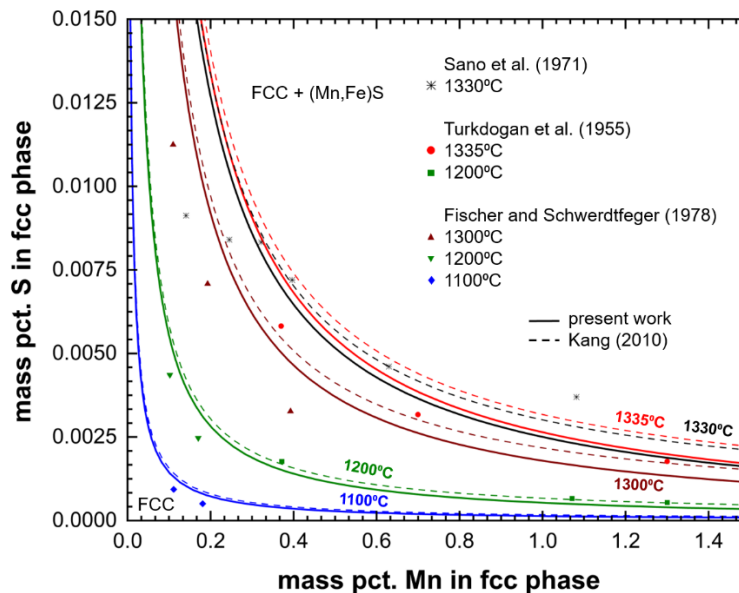


Figure 5-20: Calculated solubility of S in FCC phase in equilibrium with (Mn,Fe)S phase at different temperatures compared to the calculation of Kang [2] and experimental data of references [12],[30],[119]. Calculation performed with FactSage 8.2 [10].

Finally, it is mentioned, that there exist some deviations on the S-rich side of the equilibrium diagrams. The analysis provide evidence that an improved thermodynamic description of the (Fe,Mn)S (Pyrrhotite) phase is necessary to better represent the phase equilibria on the sulfur-rich side. Currently, (Fe,Mn)S is modeled by a two-sublattice approach with Vacancies entering the first sublattice, (Fe,Mn,Va)S. This description may lead to challenges in the Gibbs minimizations. At this state, a simple variation of the parameter in the database does not lead to satisfying results or major changes in the equilibrium diagrams. However, this assessment will be part of future research.

5.3 Derivation of an analytical equilibrium constant for MnS precipitation in liquid and solid phases

The equilibrium between solid/liquid phases and pure MnS phase was studied and parameters for the solubility product were derived based on the present thermodynamic description. The assumption of pure MnS is more practical for solidification calculations and MnS precipitation/dissolution models used in industrial models. In general, the solubility product in wt.-% is formulated as

$$(MnS) = [Mn] + [S] \quad 5-1$$

$$K = \frac{a_{Mn} * a_S}{a_{MnS}} = [wt. -\%Mn] * [wt. -\%S] \quad 5-2$$

$$\log K = -\frac{A}{T} + B \quad 5-3$$

where the activity of MnS, a_{MnS} , is set to 1 and the activities of Mn and S are simplified to their respective compositions in weight percent. Considering the optimized parameters of the present study, the solubility product of MnS can be calculated by performing a non-linear regression of calculated Liquid/MnS equilibria at various temperatures. The solubility product of MnS in equilibrium with liquid is calculated to

$$\log K_{Liquid-MnS} = -\frac{8893.53}{T} + 5.24 \quad 5-4$$

and is valid in the range of 0 to 5 wt.-% Mn and 0 to 2 wt.-% S and between 1573 K and 1973 K (1300 °C – 1700 °C). In the above equation, the value for the temperature must be used in the unit Kelvin. **Figure 5-21 a)** shows the graphical plot of the mathematical relation between temperature and equilibrium constant of the present study compared to references [20],[120]–[123]. **Figure 5-21 b)** compares the calculation performed with thermochemical software to

calculations based on different equations of the solubility product of the equilibrium between liquid phase and MnS at 1823 K. Numerical values of the references are taken from the summary of Bernhard [124] and are shown in **Table 5-3**.

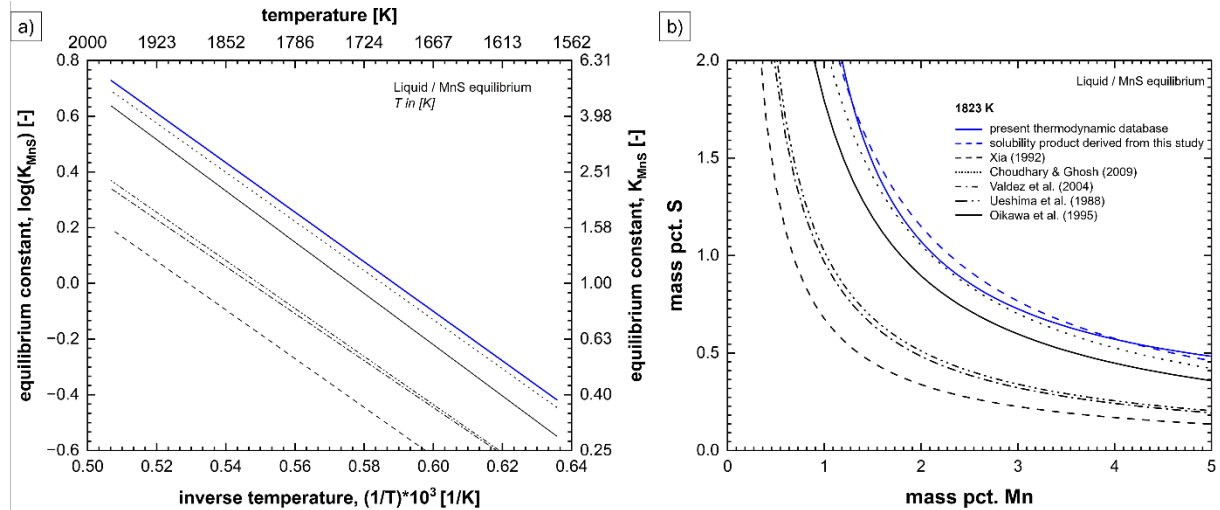


Figure 5-21: a) Relation between temperature and solubility product of the Liquid/MnS equilibrium between 1573 K and 1973 K in the range of 0 to 5 wt.-% Mn and 0 to 2 wt.-% S and b) comparison of the calculation using thermochemical software and the derived equation of the solubility product of MnS at 1823 K, compared to references [20],[120]–[123]. Calculations performed with FactSage 8.2 [10].

Table 5-3: Numerical values for the solubility product of MnS in equilibrium with liquid phase taken from the summary of Bernhard [124].

Author	A	B
present study	8893.53	5.24
Xia [120]	8750	4.63
Choudhary and Ghosh [121]	8817	5.16
Valdez et al. [122]	8431	4.61
Ueshima et al. [123]	8625	4.74
Oikawa et al. [20]	9200	5.30

Numerical values for A and B from literature differ from the calculation of the present study due to probably different experimental data used for deriving the solubility product. However, in general, the literature data match well with the results of the MQM. It is evident from **Figure 5-21** that the derived equation from the MQM leads to the highest solubility product of MnS. The solubility product of Xia et al. [120] is very low compared to other literature data and would mean that MnS precipitates very early during solidification of steel. The derivations of Valdez et al. [122] and Ueshima et al. [123] are very similar and in between the equations of Xia et al. [120] and the present study. The solubility product based on the present study and the equations of Choudhary and Ghosh [121] and Oikawa et al. [20] match to a good extent. These values state that MnS precipitates rather late during the solidification and Mn and S are longer stable. This effect can lead to lower values of the solidus temperatures.

The solubility product of MnS in equilibrium with BCC is calculated to

$$\log K_{BCC-MnS} = -\frac{12041.47}{T} + 5.33 \quad 5-5$$

and is valid in the range of 0 to 2 wt.-% Mn and 0 to 0.2 wt.-% S and between 1573 K and 1823 K (1300 °C – 1550 °C). The solubility product of MnS in equilibrium with FCC is

$$\log K_{FCC-MnS} = -\frac{12147.23}{T} + 5.02 \quad 5-6$$

and is valid in the range of 0 to 2 wt.-% Mn and 0 to 0.1 wt.-% S and between 1373 K and 1723 K (1100 °C – 1450 °C). In both equations, the value for the temperature must be used in the unit Kelvin. **Figure 5-22** and **Figure 5-23** show the graphical plot of the solubility product of MnS in equilibrium with BCC and FCC phase, respectively, as well as the comparison between calculations performed by thermochemical software and derived equations of the solubility product at various temperatures. Like the derived equation of the liquid phase, the values of the solubility product of MnS in solid phases based on the present model are above those of literature. More Mn and S can enrich in the phase and MnS precipitates late.

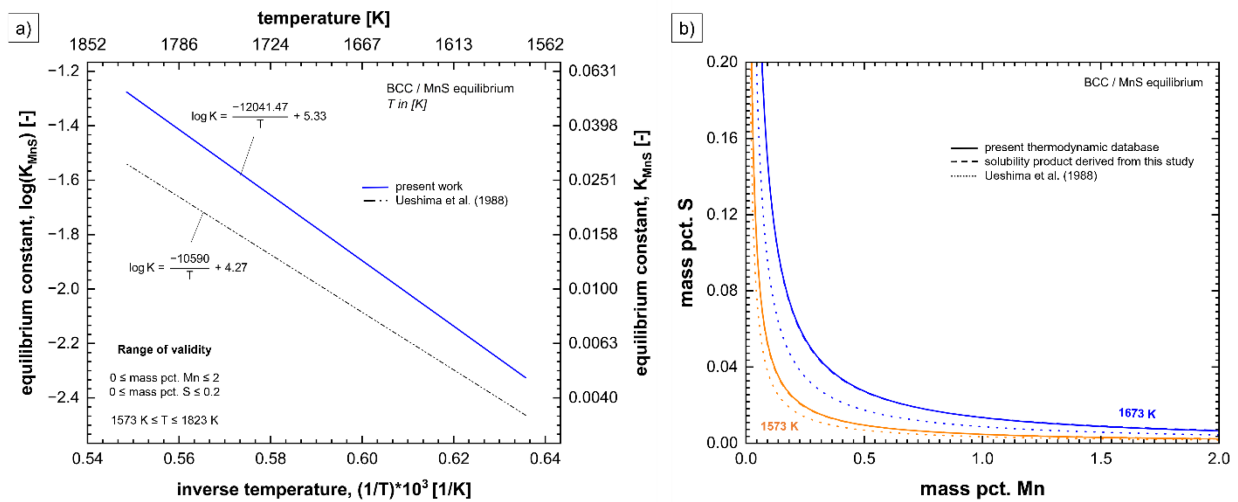


Figure 5-22: a) Relation between temperature and solubility product of the BCC/MnS equilibrium between 1573 K and 1823 K in the range of 0 to 2 wt.-% Mn and 0 to 0.2 wt.-% S and b) comparison of the calculation using thermochemical software and the derived equation of the solubility product of MnS at 1673 K and 1573 K, compared to the calculation of Ueshima et al. [123]. Calculation performed with FactSage 8.2 [10].

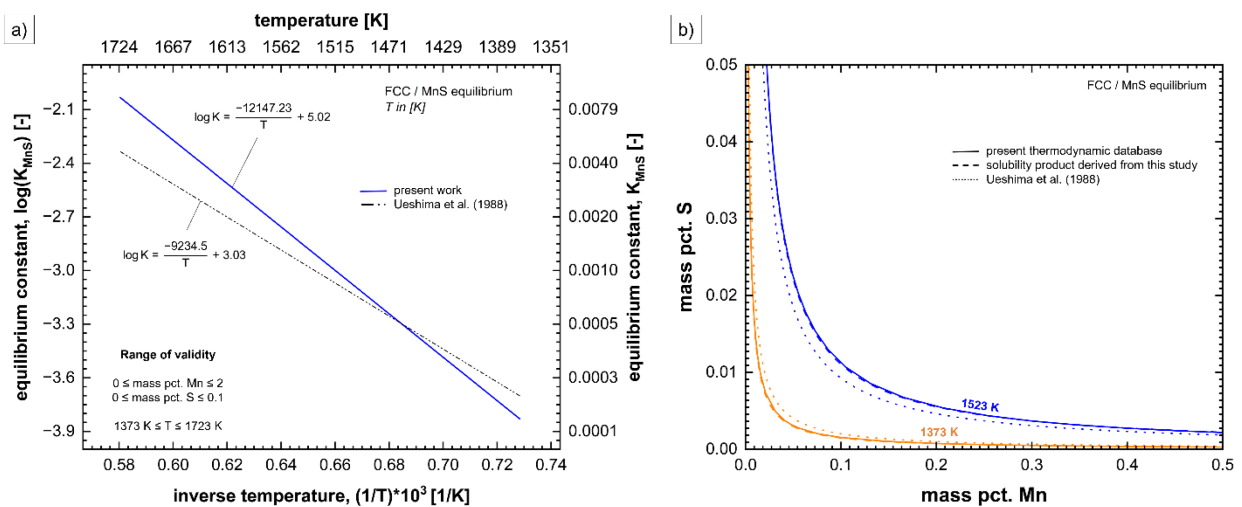


Figure 5-23: a) Relation between temperature and solubility product of the FCC/MnS equilibrium between 1373 K and 1723 K in the range of 0 to 2 wt.-% Mn and 0 to 0.1 wt.-% S and b) comparison of the calculation using thermochemical software and the derived equation of the solubility product of MnS at 1523 K and 1373 K, compared to the calculation of Ueshima et al. [123]. Calculation performed with FactSage 8.2 [10].

6 Conclusion

In modern steelmaking, Mn is known as a versatile and commonly used alloying element for advanced and high strength steel grades. Mn improves strength and work wear resistance, toughness is enhanced at ambient and cryogenic temperatures and ductility is increased for certain steel grades, as for example medium Mn steel. Therefore, Mn is used as an alloying element in steels especially for automotive, heavy, and cryogenic industry. Additionally, Mn is alloyed in steel to bind S as manganese sulfide ((Mn,Fe)S), decreasing the activity of S in steel. S in steel, which is brought in mainly by coke and coal, is considered as harmful and leads to several problems during processing of steel, especially casting and heat treatment. S segregates in interdendritic liquid, leading to hot tearing. Sulfide inclusions, which might be present in solidified steel, decrease ductility and may lead to surface quality issues during bending of continuously cast products. To meet the required quality of continuously cast semi-finished steel products and to increase productivity, online quality prediction tools are currently under development and use in various steel plants. Knowledge about boundary conditions as material properties, casting machine parameters, cooling conditions in mold and secondary cooling as well as precise thermodynamic-kinetic data is crucial.

To improve thermodynamic data of steels in the system Fe-Mn-S, an experimental investigation of the systems Fe-0.5%Mn-var%S and Fe-2%Mn-var%S with up to 0.3 wt.-% S has been performed using Differential Scanning Calorimetry (DSC) in the first part of this study. The goal of those experiments was the investigation of phase transformation temperatures in these systems with emphasis on solidification of steel. Furthermore, temperature-depending stability and dissolution mechanisms of (Mn,Fe)S during heating and cooling of steel were studied. Samples were produced in the high frequency remelting (HFR) process. Optical emission spectroscopy and C/S combustion analysis have been carried out for precise

chemical composition. Samples of 50-60 mg were cut from the HFR samples. DSC analysis with two different heating cycles per alloy has been performed with subsequent critical evaluation of the measured signals. In the low temperature range, the Curie temperature T_{Curie} and the BCC-FCC phase transformation temperature $T_{\alpha \rightarrow \gamma}^{\text{end}}$ have been investigated, whereas in the high temperature range, start and end temperature of FCC-BCC phase transformation, $T_{\gamma \rightarrow \delta}^{\text{start}}$ and $T_{\gamma \rightarrow \delta}^{\text{end}}$, as well as solidus and liquidus temperatures, T_{solid} and $T_{\text{liquid}}^{\delta}$, were measured. In samples containing enough Mn and S, the dissolution of (Mn,Fe)S could be detected as peak in the DSC signal, $T_{\text{MnS}}^{\text{end}}$. A check of the obtained signal using thermo-optical analysis by high-temperature laser scanning confocal microscopy (HT-LSCM) confirmed the measurement of the heat content of the dissolution of (Mn,Fe)S. Hence, thermodynamic mechanisms in Fe-Mn-S steels could be described even more precise.

In the system Fe-0.5%Mn-var%S, T_{Curie} is measured to be between 764 °C and 768 °C and between 745 °C and 751 °C in the system Fe-2%Mn-var%S. T_{Curie} slightly increases with increasing amount of S but decreases at higher contents of Mn. A similar effect can be seen at $T_{\alpha \rightarrow \gamma}^{\text{end}}$, which is also rising with higher amounts of S and decreases at higher contents of Mn and was found to be between 893 °C and 918 °C for the system Fe-0.5%Mn-var%S and between 836 °C and 852 °C for alloys in the system Fe-2%Mn-var%S.

In the high temperature range, $T_{\gamma \rightarrow \delta}^{\text{start}}$ is measured from 1410 °C to 1380 °C and $T_{\gamma \rightarrow \delta}^{\text{end}}$ from 1425 °C to 1400 °C for alloys with 0.5 wt.-% Mn. For alloys with 2 wt.-% Mn, $T_{\gamma \rightarrow \delta}^{\text{start}}$ lies between 1429 °C and 1420 °C whereas $T_{\gamma \rightarrow \delta}^{\text{end}}$ is between 1443 °C and 1441 °C. In both systems, $T_{\gamma \rightarrow \delta}^{\text{start}}$ and $T_{\gamma \rightarrow \delta}^{\text{end}}$ decrease with increasing amounts of S but rises with higher amounts of Mn. T_{solid} also decreases with rising amounts of S and decreases at higher contents of Mn and was found to be between 1526 °C and 1443 °C and between 1515 °C and 1493 °C in the systems Fe-0.5%Mn-var%S and Fe-2%Mn-var%S, respectively. As expected, $T_{\text{liquid}}^{\delta}$ drops to lower values at higher S and Mn content in the alloys (1533 °C and 1523 °C) in the system Fe-0.5%Mn-var%S and between 1528 °C and 1516 °C in the system Fe-2%Mn-var%S.

$T_{\text{MnS}}^{\text{end}}$ can be considered as constant for each system. For alloys containing 0.5 wt.-% Mn, $T_{\text{MnS}}^{\text{end}}$ lies at about 1477 °C. For alloys with 2 wt.-% Mn, $T_{\text{MnS}}^{\text{end}}$ lies at about 1505 °C. The dissolution of (Mn,Fe)S happens at higher temperatures if the amount of Mn is higher.

In the second part of this study, a thermodynamic modeling of the systems Fe-Mn, Fe-Mn-C and Fe-Mn-S was performed. Based on previous studies from the literature a self-consistent thermodynamic database for the Fe-C-Mn-S system was created. The binary system Fe-Mn, which greatly influences the ternary systems (Fe-Mn-C, Fe-Mn-S), was critically re-assessed

using literature data leading to major improvements in the thermodynamic description of this important sub-system. DSC measurements of Fe-Mn and Fe-Mn-C by Presoly [114] those of the present work for Fe-Mn-S were considered for thermodynamic modeling in the binary and ternary systems. The need for optimization was given, as some important phase fields could not be calculated accurately with previous databases.

The thermodynamic optimization was carried out using the Modified Quasichemical Model (MQM) for the liquid phase, enabling the modeling of alloys with strong Short Range Ordering (SRO) tendency, which is the case for metallic alloys with non-metallic melts. The Compound Energy Formalism (CEF) was used for solid solutions, while Stoichiometric Compounds (STC) were directly taken from literature. In the Fe-Mn system, parameters for the liquid, BCC, FCC and CBCC were adjusted, whereas for Fe-Mn-C, the description of liquid and FCC only required minor modifications. The re-assessed Fe-Mn system already improved parts of the ternary system Fe-Mn-S and previous databases were already in good agreement with the DSC measurements. Hence, the Fe-Mn-S parameters as proposed by Kang [2] were kept unchanged. However, it must be noted that the (Fe,Mn)S (Pyrrhotite) parameter needs further optimization, as the selected sublattice structure leads to challenges in the Gibbs minimization process. At this stage, a simple variation of the parameter did not lead to satisfying results. Further work has to deal with a better and more complex description of this phase.

Lastly, a mathematical description of the solubility product of MnS in equilibrium with Liquid, BCC and FCC phase based on the present thermodynamic model in a broad temperature range has been derived and can be used to estimate the dissolution or stability tendency of MnS in the ternary system. The derived models give the following equations:

$$\log K_{Liquid-MnS} = -\frac{8893.53}{T} + 5.24$$

$$\log K_{BCC-MnS} = -\frac{12041.47}{T} + 5.33$$

$$\log K_{FCC-MnS} = -\frac{12147.23}{T} + 5.02$$

Compared to literature data, the values for the solubility product of MnS based on the MQM are calculated higher. In terms of thermodynamics, these higher values anticipate a late precipitation of MnS and a wide stability of Mn and S in the liquid and solid phases.

The present work comprises a database of the quaternary system Fe-C-Mn-S based on high-precision and high-quality DSC and DTA measurements, which provides an excellent basis for future thermodynamic research activities with possible consideration of additional elements for modeling modern high-manganese steel grades. The implementation of the solubility limits into

existing microsegregation models will allow a more accurate prediction of (Mn,Fe)S. The knowledge gained from the series of experiments using thermal analysis can serve as a starting point for further investigations of alloys containing manganese and sulphur in order to gain an even better understanding of the formation and dissolution of (Mn,Fe)S in the future.

Bibliography

- [1] worldsteel Association, 2023: World Steel in Figures. https://worldsteel.org/publications/bookshop/?filter_publication-subject=steel-data-and-statistics, Accessed: 27.10.2023
- [2] Y.-B. Kang, Critical evaluations and thermodynamic optimizations of the Mn–S and the Fe–Mn–S systems. *Calphad* 34 (2010), 2, pp. 232–244. doi:10.1016/j.calphad.2010.03.005
- [3] M.-S. Kim and Y.-B. Kang, Thermodynamic Modeling of the Fe-Mn-C and the Fe-Mn-Al Systems Using the Modified Quasichemical Model for Liquid Phase. *Journal of Phase Equilibria and Diffusion* 36 (2015), 5, pp. 453–470. doi:10.1007/s11669-015-0401-7
- [4] F. Tafwidli and Y.-B. Kang, Thermodynamic Modeling of Fe–C–S Ternary System. *ISIJ International* 57 (2017), 5, pp. 782–790. doi:10.2355/isijinternational.ISIJINT-2016-672
- [5] K. Shubhank and Y.-B. Kang, Critical evaluation and thermodynamic optimization of Fe–Cu, Cu–C, Fe–C binary systems and Fe–Cu–C ternary system. *Calphad* 45 (2014), pp. 127–137. doi:10.1016/j.calphad.2013.12.002
- [6] P. Waldner and A.D. Pelton, Thermodynamic modeling of the Fe-S system. *Journal of Phase Equilibria and Diffusion* 26 (2005), 1, pp. 23–38. doi:10.1007/s11669-005-0055-y
- [7] B. Huchtemann and E. Wulfmeier, Residual elements in engineering steels and their influence on the technological properties. *Stahl und Eisen* 118 (1998), 11, pp. 129–135.
- [8] K. Schwerdtfeger, *Rianflligkeit von Sthlen beim Stranggieen und Warmumformen*. Verlag Stahleisen, Dsseldorf (1994).
- [9] E. Steinmetz and F. Oeters, Metallurgische Grundlagen zum Verhalten des Schwefels in Eisenschmelzen. *Stahl und Eisen* 97 (1977), 8

-
- [10] C.W. Bale, E. Bélisle, P. Chartrand, S.A. Deckerov, G. Eriksson, A.E. Gheribi, K. Hack, I.-H. Jung, Y.-B. Kang, J. Melançon, A.D. Pelton, S. Petersen, C. Robelin, J. Sangster, P. Spencer and M.-A. van Ende, FactSage thermochemical software and databases, 2010–2016. *Calphad* 54 (2016), pp. 35–53. doi:10.1016/j.calphad.2016.05.002
- [11] R. Diederichs and W. Bleck, Modelling of Manganese Sulphide Formation during Solidification, Part I: Description of MnS Formation Parameters. *steel research int.* 77 (2006), 3, pp. 202–209. doi:10.1002/srin.200606375
- [12] E.T. Turkdogan, S. Ignatowicz and J. Pearson, The solubility of sulphur in iron and iron-manganese alloys. *Journal of the Iron and Steel Institute* 180 (1955), pp. 349–354.
- [13] W. Dahl, Werkstoffkundliche Grundlagen zum Verhalten von Schwefel im Stahl. *Stahl und Eisen* 97 (1977), 8, pp. 402–409.
- [14] J.K. Brimacombe, The challenge of quality in continuous casting processes. *Metall Mater Trans A* 30 (1999), 8, pp. 1899–1912. doi:10.1007/s11661-999-0001-4
- [15] B.G. Thomas, J.K. Brimacombe and I.V. Samarasekera, The Formation of Panel Cracks in Steel Ingots: a State-of-the-Art Review. *ISS Transactions* 7 (1986), pp. 7–20.
- [16] M. Bernhard, Influence of Phosphorus on high-temperature phase transformations in steel. Dissertation, Leoben (2021).
- [17] C.E. Sims and F.B. Dahle, Effect of Aluminum on the Properties of Medium Carbon Cast Steel. *Transactions of the American Foundrymen's Association* 46 (1938), pp. 65–132.
- [18] K. Matsubara, On the Behaviours of the Precipitated Sulphide Inclusions in Solid Steel. *ISIJ Int.* 6 (1966), 3, pp. 139–148. doi:10.2355/isijinternational1966.6.139
- [19] Y. Ito, N. Masumitsu and K. Matsubara, Formation of Manganese Sulfide in Steel. *ISIJ Int.* 21 (1981), 7, pp. 477–484. doi:10.2355/isijinternational1966.21.477
- [20] K. Oikawa, H. Ohtani, K. Ishida and T. Nishizawa, The Control of the Morphology of MnS Inclusions in Steel during Solidification. *ISIJ Int.* 35 (1995), 4, pp. 402–408. doi:10.2355/isijinternational.35.402
- [21] A.T. Dinsdale, SGTE data for pure elements. *Calphad* 15 (1991), 4, pp. 317–425. doi:10.1016/0364-5916(91)90030-N
- [22] V. Raghavan, C-Fe-S (Carbon-Iron-Sulfur). *Journal of Phase Equilibria* 19 (1998), 3, pp. 262–263. doi:10.1361/105497198770336794
- [23] V. Raghavan, C-Fe-Mn (Carbon-Iron-Manganese). *Journal of Phase Equilibria* 15 (1994), 4, pp. 421–424.

- [24] V. Raghavan, Fe-Mn-S (Iron-Manganese-Sulfur). *Journal of Phase Equilibria and Diffusion* 32 (2011), 2, pp. 147–151. doi:10.1007/s11669-010-9826-1
- [25] H. Okamoto, The C-Fe (carbon-iron) system. *JPE* 13 (1992), 5, pp. 543–565. doi:10.1007/BF02665767
- [26] H. Okamoto, Mn-S (Manganese-Sulfur). *Journal of Phase Equilibria and Diffusion* 32 (2011), 1, pp. 78. doi:10.1007/s11669-010-9810-9
- [27] E.A. Brandes and R.F. Flint, The Fe–Mn (Iron-Manganese) system. *Bulletin of Alloy Phase Diagrams* 2 (1981), 1, pp. 106. doi:10.1007/BF02873718
- [28] S. Lin, H. Yang, Y. Su, K. Chang, C. Yang and S. Lin, CALPHAD-assisted morphology control of manganese sulfide inclusions in free-cutting steels. *Journal of Alloys and Compounds* 779 (2019), pp. 844–855. doi:10.1016/j.jallcom.2018.11.290
- [29] Y. Lu and T. Miki, Thermodynamics of Molten MnS–FeS and CrS–FeS System at 1843 K. *ISIJ Int.* 61 (2021), 9, pp. 2345–2354. doi:10.2355/isijinternational.isijint-2020-740
- [30] N. Sano, M. Iwata, H. Hosoda and Y. Matsushita, Phase Relations of Fe-Mn-S System at 1330° and 1615°C. *Tetsu-to-Hagane* 57 (1971), 13, pp. 1984–1989. doi:10.2355/tetsutohagane1955.57.13_1984
- [31] R. Vogel and W. Hotop, Das Zustandsschaubild Eisen-Eisensulfid-Mangansulfid-Mangan. *Archiv für das Eisenhüttenwesen* 11 (1937), 1, pp. 41–54. doi:10.1002/srin.193700988
- [32] O. Meyer and F. Schulte, Das Gleichgewicht $\text{FeS} + \text{Mn} \rightleftharpoons \text{MnS} + \text{Fe}$ bei hohen Temperaturen. *Archiv für das Eisenhüttenwesen* 8 (1934), 5, pp. 187–195. doi:10.1002/srin.193400128
- [33] S. Ban-ya and J. Chipman, Sulfur in Liquid Iron Alloys. PT. 2. Effects of Alloying Elements. *Trans. Metall. Soc. AIME* (1969), 245, pp. 133–143.
- [34] C.W. Sherman and J. Chipman, Activity of Sulphur in Liquid Iron and Steel. *JOM* 4 (1952), 6, pp. 597–602. doi:10.1007/BF03397725
- [35] M. Fischer and K. Schwerdtfeger, Thermodynamics of the system Fe-Mn-S: Part I. activities in Iron sulfide-manganese Sulfide Solid Solutions in the Temperature Range 1100 to 1400°C. *Metall Mater Trans B* 8 (1977), 2, pp. 467–470. doi:10.1007/BF02696934
- [36] G.S. Mann and L.H. Vlack, FeS-MnS phase relationships in the presence of excess iron. *Metall Mater Trans B* 7 (1976), 3, pp. 469–475. doi:10.1007/BF02652718
- [37] Y. Ito, N. Yonezawa and K. Matsubara, Eutectic Conjugation in Fe-Mn-S System. *Tetsu-to-Hagane* 65 (1979), 3, pp. 391–398. doi:10.2355/tetsutohagane1955.65.3_391

- [38] E. Schürmann and H.J. Strösser, Untersuchung der Schmelzgleichgewichte im Teildiagramm Eisen-Eisensulfid-Mangan-Mangansulfid des Systems Eisen-Mangan-Schwefel. *Archiv für das Eisenhüttenwesen* 46 (1975), 12, pp. 761–766. doi:10.1002/srin.197503721
- [39] H. Nakao, Thermodynamic and Kinetic Study of the Iron-Manganese-Sulfur System at 1300°C. Hamilton (1967).
- [40] P.N. Smith, The Constitution and Kinetics of the System Fe-Mn-S Between 1200° and 1800°C. Dissertation, Hamilton (1970).
- [41] J.S. Kirkaldy, H. Nakao, I.S.R. Clark and P.N. Smith, An investigation of the phase constitution of Fe-Mn-S in the vicinity of 1300°C. Paper I. *Canadian Metallurgical Quarterly* 12 (1973), 1, pp. 45–51. doi:10.1179/cmqr.1973.12.1.45
- [42] J.P. Coughlin, High-temperature Heat Contents of Manganous Sulfide, Ferrous Sulfide and Pyrite (1950).
- [43] R. Kiessling and C. Westman, Sulphide Inclusions and Synthetic sulphides of the Mn, Me-S type. *J. Iron Steel Inst.* (1966), 204, pp. 377–379.
- [44] V. Dashevsky and V. Kashin, Solubility and activity of Sulfur in Manganese and Manganese Alloys. *Izv. Akad. Nauk SSSR Met* (1973), 5, pp. 85–88.
- [45] G.S. Mann, Phase Equilibria of Iron and Manganese with Sulfur, Selenium and Tellurium. Dissertation, Michigan (1974).
- [46] H. Wada, DSC studies on reactions of the elements with sulfur. *Solid State Ionics* 172 (2004), 1-4, pp. 421–424. doi:10.1016/j.ssi.2004.03.027
- [47] A.R. Troiano and F.T. McGuire, A study of the iron-rich iron-manganese alloys. *Trans. ASM* (1943), 31, pp. 340–359.
- [48] A. Hellawell and W. Hume-Rothery, The constitution of alloys of iron and manganese with transition elements of the first long period. *Phil. Trans. R. Soc. Lond. A* 249 (1957), 968, pp. 417–459. doi:10.1098/rsta.1957.0004
- [49] W. Hume-Rothery and R.A. Buckley, Liquidus Solidus relations in the system iron-manganese. *J. Iron Steel Inst* 202 (1964), pp. 534.
- [50] G.I. Batalin, N.N. Minenko and V.S. Sudavtsova, Enthalpy of Mixing and Thermodynamic Properties of Liquid Alloys of Iron with Manganese, Cobalt, and Nickel. *Russ. Metall.* 5 (1974), pp. 82–86.

- [51] J.F. Butler, C.L. McCabe and H.W. Paxton, Thermodynamic Activities in the Fe-Mn-C System. Transactions of the Metallurgical Society of AIME 3 (1961), 221, pp. 479–484.
- [52] Y. Endoh and Y. Ishikawa, Antiferromagnetism of γ -Iron-Manganese Alloys. J. Phys. Soc. Jpn. 30 (1971), 6, pp. 1614–1627. doi:10.1143/JPSJ.30.1614
- [53] Y. Ishikawa and Y. Endoh, Antiferromagnetism of γ -FeMn Alloys. II. Neutron Diffraction and Mössbauer Effect Studies. J. Phys. Soc. Jpn. 23 (1967), 2, pp. 205–213. doi:10.1143/JPSJ.23.205
- [54] T. Hashimoto and Y. Ishikawa, Antiferromagnetism of γ -FeMn Alloys. III. Specific Heat and Thermoelectric Power Studies. J. Phys. Soc. Jpn. 23 (1967), 2, pp. 213–223. doi:10.1143/JPSJ.23.213
- [55] H. Umebayashi and Y. Ishikawa, Antiferromagnetism of γ Fe-Mn Alloys. J. Phys. Soc. Jpn. 21 (1966), 7, pp. 1281–1294. doi:10.1143/JPSJ.21.1281
- [56] M. Hillert, T. Wada and H. Wada, The Alpha-Gamma Equilibrium in Fe-Mn, Fe-Mo, Fe-Ni, Fe-Sb, Fe-Sn and Fe-W Systems. Iron Steel Inst J 205 (1967), 5, pp. 539–546.
- [57] K. Sanbongi and M. Ohtani, On the Activities of Coexisting Elements in Molten Iron. III. The Activity of Mn in Molten Fe-Mn Alloy. Science Reports of the Research Institutes, Tohoku University 7 (1955), pp. 204–209. doi:10.50974/00041784
- [58] C.W. Schultz, N. Riazance and S.L. Payne, Activity of Manganese in Liquid Iron-manganese Alloys (1966), U.S. Department of the Interior, Bureau of Mines.
- [59] K. Schwerdtfeger, Measurements of Oxygen Activity in γ -iron, Iron-Silicon, Manganese and Iron-Manganese Melts Using Solid Electrolyte Galvanic Cell. Trans. Metall. Soc. AIME 239 (1967), pp. 1276–1280.
- [60] J.-M. Steiler, P. Riboud, M. Onilon and M. Olette, Determination de l'activité thermodynamique des constituants du systems Fe-Mn liquide par une metode d'entraînement. C.R. Acad. Sc. Paris 277 (1973), C, pp. 1207–1210.
- [61] V.S. Sudavtsova, G.I. Batalin and V. Bandur, Thermodynamic Properties of Alloys of the Fe-Mn System in Liquid State. Ukr. Khim. Zh. 45 (1979), 8, pp. 718–721.
- [62] K.T. Jacob, J.P. Hajra and M. Iwase, Activities of Mn in solid and liquid Fe-Mn alloys. Archiv für das Eisenhüttenwesen 55 (1984), 9, pp. 421–426. doi:10.1002/srin.198405368
- [63] B. Predel and W. Gust, Ausscheidungsreaktionen im System Eisen-Mangan. Archiv für das Eisenhüttenwesen 43 (1972), 9, pp. 721–726. doi:10.1002/srin.197204454

- [64] K.K. Srivastava and J.S. Kirkaldy, The alpha-gamma phase boundaries and the T₀ line for Fe-Mn alloys. *Metallurgical Transactions A* 13 (1982), 12, pp. 2113–2119. doi:10.1007/BF02648381
- [65] R. Kubitz, G. McHugh and F.H. Hayes, Calorimetric and Torsion Effusion Studies of Solid Fe-Mn Alloys, in: *Dep. Metall. Mat. Sci* (1987), Univ. Manchester & UMIST Britain.
- [66] S. Cotes, M. Sade and A.F. Guillermet, Fcc/Hcp martensitic transformation in the Fe-Mn system: Experimental study and thermodynamic analysis of phase stability. *Metallurgical Transactions A* 26 (1995), 8, pp. 1957–1969. doi:10.1007/BF02670667
- [67] V.T. Witusiewicz, F. Sommer and E.J. Mittemeijer, Enthalpy of formation and heat capacity of Fe-Mn alloys. *Metall Mater Trans B* 34 (2003), 2, pp. 209–223. doi:10.1007/s11663-003-0008-y
- [68] R. Benz, Thermodynamics of the Fe-Mn-C system from solid state EMF measurements. *Metall Mater Trans B* 5 (1974), pp. 2217–2224. doi:10.1007/BF02643936
- [69] E.-J. Kim, B.-D. You and J.-J. Pak, Thermodynamics of Carbon in Liquid Manganese and Ferromanganese Alloys. *Metall Mater Trans B* 34 (2003), 1, pp. 51–59. doi:10.1007/s11663-003-0054-5
- [70] J. Chipman, R. Alfred, L. Gott, R. Small, D. Wilson, C. Thomson and D. Gue, The solubility of carbon in molten iron and in iron-silicon and iron-manganese alloys. *Trans ASM* (1952), 44, pp. 1215–1232.
- [71] E.T. Turkdogan, R. Hancock, S. Herlitz and J. Dentan, Thermodynamics of carbon dissolved in iron alloys. *J. Iron Steel Inst.* (1956), 183, pp. 69–72.
- [72] R. Ni, Z. Ma and S. Wei, Thermodynamics of Mn-Fe-C and Mn-Si-C system. *Steel Research* 61 (1990), 3, pp. 113–116. doi:10.1002/srin.199000313
- [73] M.-K. Paek, W.-K. Lee, J. Jin, J.-M. Jang and J.-J. Pak, Thermodynamic Interactions Among Carbon, Silicon and Iron in Carbon Saturated Manganese Melts. *Korean J. Met.Mater.* 50 (2012), 1, pp. 45–51. doi:10.3365/KJMM.2012.50.1.045
- [74] H. Enokido, A. Moro-Oka and E. Ichise, Thermo-chemical Activities of Liquid Fe-Mn-C Alloy. *Tetsu-to-Hagane* 81 (1995), 6, pp. 619–624. doi:10.2355/tetsutohagane1955.81.6_619
- [75] K. Kuo and L. Persson, A contribution to the constitution of the ternary system Fe-Mn-C at 1050C, 910C, and 690C. *J. Iron Steel Inst.* 178 (1954), pp. 39–44.

- [76] W. Koch and H. Keller, Equilibrium investigations in the system iron-manganese-carbon as an example for the use of separating methods for establishing and checking constitutional diagrams. *Archiv für das Eisenhüttenwesen* 35 (1964), pp. 1173–1180.
- [77] T. Nishizawa, An experimental study of the Fe-Mn-C and Fe-Cr-C systems at 1000C. *Scand. J. Metall.* 6 (1977), pp. 74–78.
- [78] R. Benz, J.F. Elliott and J. Chipman, Thermodynamics of the solid phases in the system Fe–Mn–C. *Metall Trans* 4 (1973), 8, pp. 1975–1986. doi:10.1007/BF02665426
- [79] R. Gurry, J. Christakos and L. Darken, Size, manganese content, and curie point of carbides extracted from manganese steel. *Trans. ASM* 53 (1961), pp. 187–198.
- [80] F. Schürmann and I. Geissler, Schmelzgleichgewichte des Dreistoffsystems Eisen-Mangan-Kohlenstoff. *Giessereiforschung* (1977), 29, pp. 153–159.
- [81] E. Chen and S. Wang, Thermodynamic Properties of Mn-C Melts. *Journal of Iron and Steel Research, International* 15 (2008), 2, pp. 1–6. doi:10.1016/S1006-706X(08)60021-7
- [82] G.I. Sil'man, Phase Diagram of Alloys of the Fe-C-Mn System and some Structural Effects in this System. *Metal Science and Heat Treatment* 47 (2005), 1-2, pp. 48–52.
- [83] A. Tanaka, Activities of Manganese in Mn–Fe–C, Mn–Si–C and Mn–Fe–Si–C Melts at 1673 K. *Trans. JIM* 21 (1980), 1, pp. 27–33. doi:10.2320/matertrans1960.21.27
- [84] T. Wada, H. Wada, J.F. Elliott and J. Chipman, Thermodynamics of the fcc Fe-Mn-C and Fe-Si-C alloys. *Metall Trans* 3 (1972), 6, pp. 1657–1662. doi:10.1007/BF02643059
- [85] W. Huang, An assessment of the Fe-Mn system. *Calphad* 13 (1989), 3, pp. 243–252. doi:10.1016/0364-5916(89)90004-7
- [86] V.T. Witusiewicz, F. Sommer and E.J. Mittemeijer, Reevaluation of the Fe-Mn Phase Diagram. *Journal of Phase Equilibria and Diffusion* 25 (2004), 4, pp. 346–354. doi:10.1361/15477030420115
- [87] W. Huang, A thermodynamic assessment of the Fe-Mn-C system. *Metall Trans A* 21 (1990), 8, pp. 2115–2123. doi:10.1007/BF02647870
- [88] D. Djurovic, B. Hallstedt, J. von Appen and R. Dronskowski, Thermodynamic assessment of the Fe–Mn–C system. *Calphad* 35 (2011), pp. 479–491. doi:10.1016/j.calphad.2011.08.002
- [89] J. Miettinen and B. Hallstedt, Thermodynamic assessment of the Fe-FeS-MnS-Mn system. *Calphad* 22 (1998), 2, pp. 257–273. doi:10.1016/S0364-5916(98)00027-3
- [90] D. Dilner, H. Mao and M. Selleby, Thermodynamic assessment of the Mn–S and Fe–Mn–S systems. *Calphad* 48 (2015), pp. 95–105. doi:10.1016/j.calphad.2014.11.004

- [91] Arthur D. Pelton and Youn-Bae Kang, Modeling short-range ordering in solutions. *International Journal of Materials Research* 98 (2007), 10, pp. 907–917. doi:10.3139/146.101554
- [92] A.D. Pelton, *Phase Diagrams and Thermodynamic Modeling of Solutions*. Amsterdam (2019), Elsevier.
- [93] A.D. Pelton, S.A. Degterov, G. Eriksson, C. Robelin and Y. Dessureault, The modified quasichemical model I—Binary solutions. *Metall Mater Trans B* 31 (2000), 4, pp. 651–659. doi:10.1007/s11663-000-0103-2
- [94] M. Bernhard, P. Presoly, N. Fuchs, C. Bernhard and Y.-B. Kang, Experimental Study of High Temperature Phase Equilibria in the Iron-Rich Part of the Fe-P and Fe-C-P Systems. *Metallurgical Transactions A* 51 (2020), 10, pp. 5351–5364. doi:10.1007/s11661-020-05912-z
- [95] M. Bernhard, N. Fuchs, P. Presoly, P. Angerer, B. Friessnegger and C. Bernhard, Characterization of the γ -loop in the Fe-P system by coupling DSC and HT-LSCM with complementary in-situ experimental techniques. *Materials Characterization* 174 (2021), pp. 111030. doi:10.1016/j.matchar.2021.111030
- [96] Linn High Temp GmbH, LIFUMAT-M-MODEL. <https://www.linn-high-temp.de/products/induction-heating/sample-preparation-for-spectroscopy/remelting/details/lifumat-m-model.html>, Accessed: 17.12.2023
- [97] W.F. Hemminger and H.K. Cammenga, *Methoden der Thermischen Analyse: Anleitungen für die chemische Laboratoriumspraxis*. Heidelberg (1989), Springer.
- [98] G. Höhne, W. Hemminger and H.-J. Flammersheim, *Differential scanning calorimetry. 2., rev. and enlarged ed.* (2003), Berlin [u.a.] Springer.
- [99] Netzsch Gerätebau GmbH, DSC 404 F1 Pegasus: Hochtemperatur DSC. <https://analyzing-testing.netzsch.com/de/produkte-und-loesungen/dynamische-differenzkalorimetrie-dsc-differenz-thermoanalyse-dta/dsc-404-f1-pegasus>, Accessed: 25.05.2023
- [100] P. Presoly, R. Pierer and C. Bernhard, Identification of Defect Prone Peritectic Steel Grades by Analyzing High-Temperature Phase Transformations. *Metall Mater Trans A* 44 (2013), 12, pp. 5377–5388. doi:10.1007/s11661-013-1671-5
- [101] M. Liu, M. Bernhard, M. Kawuloková, J. Walek, M. Kern, S. Zlá, P. Presoly, B. Smetana, M. Tkadlečková, G. Xu, Y.-B. Kang and C. Bernhard, Decomposition of γ -Fe in 0.4C–1.8Si–2.8Mn–0.5Al steel during a continuous cooling process: A comparative study using in-situ HT-

LSCM, DSC and dilatometry. *Journal of Materials Research and Technology* 24 (2023), pp. 3534–3547. doi:10.1016/j.jmrt.2023.04.009

[102] L. Drozdová, B. Smetana, P. Presoly, V. Novák, M. Machů, M. Bernhard, H. Francová, S. Zlá, L. Řeháčková and C. Bernhard, Investigation of Fe–C–Cr and Fe–C–Cr–Ni-based systems with the use of DTA and HT-LSCM methods. *Journal of Thermal Analysis and Calorimetry* 142 (2020), 2, pp. 535–546. doi:10.1007/s10973-020-10305-w

[103] H. Lukas, S.G. Fries and B. Sundman, *Computational Thermodynamics: The Calphad Method*. Cambridge (2011), Cambridge University Press.

[104] G. Cacciamani, An Introduction to the CALPHAD method and the Compound Energy Formalism (CEF). *Tecnologia em Metalurgia Materiais e Mineração* 13 (2016), pp. 16–24. doi:10.4322/2176-1523.1048

[105] M. Bernhard, W.-B. Park and Y.-B. Kang, Phase equilibria and thermodynamic modeling of the Sn–S, Ag–S, and Sb–S systems. *Calphad* 83 (2023), pp. 102622. doi:10.1016/j.calphad.2023.102622

[106] P. Chartrand and A.D. Pelton, On the choice of “Geometric” thermodynamic models. *J Phs Eqil and Diff* 21 (2000), 2, pp. 141–147. doi:10.1361/105497100770340192

[107] M. Hillert, The compound energy formalism. *Journal of Alloys and Compounds* 320 (2001), 2, pp. 161–176. doi:10.1016/S0925-8388(00)01481-X

[108] B. Sundman and J. Ågren, A regular solution model for phases with several components and sublattices, suitable for computer applications. *Journal of Physics and Chemistry of Solids* 42 (1981), 4, pp. 297–301. doi:10.1016/0022-3697(81)90144-X

[109] N. Saunders and A.P. Miodownik, *CALPHAD calculation of phase diagrams: A comprehensive guide* (1998), Oxford [u.a.] Pergamon.

[110] M. Bernhard, Y.-B. Kang, Peter Presoly, A.E. Gheribi and C. Bernhard, Critical evaluation and thermodynamic modeling of the Fe–P and Fe–C–P system. *Calphad* 70 (2020), pp. 101795. doi:10.1016/j.calphad.2020.101795

[111] O. Redlich and A.T. Kister, Algebraic representation of thermodynamic properties and the classification of solutions. *Industrial and Engineering Chemistry* 40 (1948), 2, pp. 345–348.

[112] M. Hillert, Empirical methods of predicting and representing thermodynamic properties of ternary solution phases. *Calphad* 4 (1980), 1, pp. 1–12. doi:10.1016/0364-5916(80)90016-

4

- [113] M. Hillert and M. Jarl, A model for alloying in ferromagnetic metals. *Calphad* 2 (1978), 3, pp. 227–238. doi:10.1016/0364-5916(78)90011-1
- [114] P. Presoly, Thermal Analysis of the systems Fe-Mn and Fe-Mn-C at high Mn contents using DSC and DTA. Leoben, 2023.
- [115] J. Fenstad, Liquidus relations and thermochemistry within the system Fe-Mn-C-O. PhD thesis (2000).
- [116] S. Saxena and H. Midtgaard, SINTEF Report. No. STF 34F79017, Trondheim, Norway (1979).
- [117] S. Hayashi, Y. Iguchi, J. Hirao and T. Uno, The Equilibrium between Liquid Slag and Liquid Iron in Fe-Mn-O-S System. *DENKI-SEIKO* 54 (1983), 1, pp. 5–12. doi:10.4262/denkiseiko.54.5
- [118] F. Koerber, Zur Metallurgie der Eisenbegleiter. *Stahl Eisen* 56 (1936), pp. 433–444.
- [119] M. Fischer and K. Schwerdtfeger, Thermodynamics of the System Fe-Mn-S: Part II. Solubility of Sulfur and Manganese in γ -Iron Coexisting with Sulfide in the Temperature Range 1100 to 1300°C. *MTB* 9 (1978), 4, pp. 631–634. doi:10.1007/BF03257211
- [120] G. Xia, Untersuchungen über das mechanische Verhalten von erstarrendem Stahl unter stranggußähnlichen Bedingungen. Dissertation, Leoben (1992).
- [121] S.K. Choudhary and A. Ghosh, Mathematical Model for Prediction of Composition of Inclusions Formed during Solidification of Liquid Steel. *ISIJ Int.* 49 (2009), 12, pp. 1819–1827. doi:10.2355/isijinternational.49.1819
- [122] M.E. Valdez, Y. Wang and S. Sridhar, In-Situ Observation of the Formation of MnS during Solidification of High Sulphur Steels. *Steel Research* 75 (2004), 4, pp. 247–256. doi:10.1002/srin.200405952
- [123] Y. Ueshima, K. Isobe, S. Mizoguchi, H. Maede and H. Kajioka, Analysis of the Rate of Crystallization and Precipitation of MnS in the Resulphurized Free-cutting Steel. *Tetsu-to-Hagane* 74 (1988), 3, pp. 465–472. doi:10.2355/tetsutohagane1955.74.3_465
- [124] M. Bernhard, Bewertung und Anpassung eines analytischen Mikroseigerungsmodells über SSCT Versuche an Ultra Low Carbon und Low Carbon Stählen. Bachelor thesis, Leoben (2015).
- [125] Min-Kyu Paek, Jong-Jin Pak and Youn-Bae Kang, Phase equilibria and thermodynamics of Mn–C, Mn–Si, Si–C binary systems and Mn–Si–C ternary system by critical evaluation,

combined with experiment and thermodynamic modeling. *Calphad* 46 (2014), pp. 92–102. doi:10.1016/j.calphad.2014.02.007

[126] P. Gustafson, A thermodynamic evaluation of the Fe-C system. *Scand. J. Metall.* (1985), 14, pp. 259–267.

[127] D. Djurovic, B. Hallstedt, J. von Appen and R. Dronskowski, Thermodynamic assessment of the Mn–C system. *Calphad* 34 (2010), 3, pp. 279–285. doi:10.1016/j.calphad.2010.05.002

[128] B. Hallstedt, D. Djurovic, J. von Appen, R. Dronskowski, A. Dick, F. Körmann, T. Hickel and J. Neugebauer, Thermodynamic properties of cementite (Fe₃C). *Calphad* 34 (2010), 1, pp. 129–133. doi:10.1016/j.calphad.2010.01.004

A Appendix

A.1 Chemical analysis of the sample material

Table A-1: complete chemical analysis of the sample alloys

System	Alloy	S ^(a)	C ^(a)	Mn ^(b)	Si ^(b)	P ^(b)	Al ^(b)	Cr ^(b)	Ni ^(b)	Mo ^(b)	Cu ^(b)	N ^(b)	Sn ^(b)	As ^(b)	B ^(b)	Sb ^(b)	Co ^(b)
		[wt.-%] ; ^(a) C/S Combustion Analysis; ^(b) Optical Emission Spectroscopy for all alloys: Ti ^(b) <0.001; V ^(b) <0.001; Nb ^(b) <0.002; Zr ^(b) <0.002; Ca ^(b) <0.0002; W ^(b) <0.01; Ta ^(b) <0.01															
Fe-0.5%Mn-var%S	A-I	0.0021	0.0197	0.52	0.004	0.0022	0.024	0.01	0.007	0.003	0.009	0.0034	<.002	<.002	0.0003	<.002	0.002
	A-II	0.0121	0.0148	0.52	0.003	0.0021	0.028	0.01	0.007	0.003	0.009	0.0032	<.002	0.002	<.0002	<.002	0.002
	A-III	0.0261	0.0132	0.51	0.004	0.0021	0.034	0.01	0.007	0.003	0.009	0.0032	<.002	<.002	0.0002	<.002	0.002
	A-IV	0.0417	0.0195	0.51	0.003	<.002	0.026	0.009	0.007	0.002	0.009	0.0036	<.002	<.002	0.0003	<.002	0.002
	A-V	0.0944	0.0203	0.51	0.004	0.0022	0.025	0.01	0.007	0.002	0.009	0.0042	<.002	<.002	0.0008	<.002	0.002
	A-VI	0.1523	0.0130	0.50	0.004	<.002	0.025	0.009	0.007	0.002	0.009	0.0038	<.002	<.002	0.001	<.002	0.002
	A-VII	0.1930	0.0175	0.48	0.004	<.002	0.03	0.009	0.007	0.002	0.009	0.0035	<.002	<.002	0.0011	<.002	<.002
	A-VIII	0.2370	0.0162	0.47	0.004	<.002	0.03	0.009	0.007	0.001	0.009	0.004	<.002	<.002	0.0018	<.002	<.002
	A-IX	0.3047	0.0125	0.47	0.004	<.002	0.027	0.009	0.007	0.002	0.009	0.0029	<.002	<.002	0.0017	<.002	<.002
Fe-2.0%Mn-var%S	B-I	0.0025	0.0191	1.98	0.005	0.0023	0.028	0.01	0.008	0.004	0.009	0.0031	<.002	<.002	<.0002	<.002	0.002
	B-II	0.0082	0.0190	1.97	0.005	0.0023	0.036	0.01	0.008	0.004	0.009	0.0031	<.002	<.002	<.0002	<.002	0.002
	B-III	0.0145	0.0201	1.97	0.006	0.0022	0.027	0.01	0.008	0.004	0.009	0.0035	<.002	<.002	<.0002	<.002	0.002
	B-IV	0.0514	0.0155	1.94	0.005	0.0021	0.037	0.01	0.008	0.004	0.009	0.0035	<.002	<.002	0.0004	<.002	0.002
	B-V	0.1487	0.0178	1.93	0.005	<.002	0.02	0.01	0.007	0.003	0.009	0.0046	<.002	<.002	0.0012	<.002	0.002
	B-VI	0.2053	0.0219	1.90	0.006	<.002	0.031	0.01	0.007	0.003	0.009	0.0036	<.002	<.002	0.0015	<.002	<.002
	B-VII	0.3077	0.0209	1.88	0.005	<.002	0.021	0.01	0.007	0.003	0.009	0.0037	<.002	<.002	0.0025	<.002	<.002

A.2 Model parameters

Table A-2: thermodynamic model parameters for the system Fe-Mn-C

Phase (model)	Model parameter [J]	Publication
Liquid (Fe,Mn,C)	$Z_{Fe,Fe}^{Fe} = Z_{MnMn}^{Mn} = Z_{CC}^C = Z_{FeMn}^{Fe} = Z_{FeMn}^{Mn} = Z_{FeC}^C = Z_{MnC}^C = 6$	[3]
	$Z_{FeC}^{Fe} = Z_{MnC}^{Mn} = 3$	
	$\Delta g_{FeMn} = -1380.72 + 0.134T + 753.62X_{FeFe} - 586.15X_{MnMn}$	9
	$\Delta g_{FeC} = -30459.5 + 3.138T - 1129.7X_{FeFe}$	[5]
	$\Delta g_{MnC} = -42677 + 4.502T + (2092 + 1.751T)X_{MnMn}$	[125]
	$\Delta g_{Fe,Mn(C)} = -8368$	9
	<i>"Toop-like" interpolation with C as the asymmetric component</i>	
FCC (Fe,Mn) ₁ (C,Va) ₁	$G_{Fe:Va} = GFCCFE, G_{Mn:Va} = GFCCMN, G_{Fe:C} = GFCCFE + GHSERCC + 77207 - 15.88T$ [126]	
	$G_{Mn:C} = GHSERMN + GHSERCC + 13.66T$ [127]	
	$L_{Fe,Mn:Va} = -5020.8 + 1.883T$	9
	$L_{Fe,C:Va} = -34671$	[126]
	$L_{Mn,C:Va} = -21388.6 - 23012(y_C'' - y_{Va}'')$	[125]
	$L_{Fe,Mn:C} = 0$	9
	$T_{cFe:Va} = -201, T_{cMn:Va} = -1620, \beta_{Fe:Va} = -2.1, \beta_{Mn:Va} = -1.86$	[85]
$T_{cFe,Mn:Va} = -2282 - 2068(y_{Fe}' - y_{Mn}') $		
BCC (Fe,Mn) ₁ (C,Va) ₃	$G_{Fe:Va} = GHSERFE, G_{Mn:Va} = GBCCMN, G_{Fe:C} = GHSERFE + 3 GHSERCC + 322050 + 75.67T$ [126]	
	$G_{Mn:C} = GHSERMN + 3 GHSERCC + 10000 + 30T$ [127]	
	$L_{Fe,Mn:Va} = -4184 - 1.715T$	9
	$L_{Fe,C:Va} = -190T$	[126]
	$L_{Mn,C:Va} = 0$	[125]
	$T_{cFe:Va} = 1043, T_{cMn:Va} = -580, \beta_{Fe:Va} = 2.22, \beta_{Mn:Va} = -0.27$	[85]
$T_{cFe,Mn:Va} = 123$		

CBCC (Fe,Mn) ₁ (C,Va) ₁	$G_{Fe:Va}=GHSEFE+4745$ [85], $G_{Mn:Va}=GHSEMN$, $G_{Fe:C}=GHSEFE+GHSECC+50000$ [3]	
	$G_{Mn:C}=GHSEMN+GHSECC+5000+22.47T$ [127]	
	$L_{Fe,Mn:Va}=-9414$	ϑ
	$L_{Fe,C:Va}=-34671$	[87]
	$L_{Mn,C:Va}=-50208$	[125]
CUB (Fe,Mn) ₁ (C,Va) ₁	$G_{Fe:Va}=GHSEFE+3745$ [85], $G_{Mn:Va}=GCUBMN$, $G_{Fe:C}=GHSEFE+GHSECC+90000$ [87]	
	$G_{Mn:C}=GHSEMN+GHSECC+2607$ [127]	
	$L_{Fe,Mn:Va}=-11518+2.82T$	[85]
	$L_{Fe,C:Va}=-34671$	[87]
	$L_{Mn,C:Va}=-10460$	[125]
HCP (Fe,Mn) ₁ (C,Va) _{0.5}	$G_{Fe:Va}=GHCPFE$, $G_{Mn:Va}=GHCPMN$ [21], $G_{Fe:C}=GFCCFE+0.5$ GHSECC+48512.5-8.78T [3]	
	$G_{Mn:C}=GHSEMN+0.5$ GHSECC-9000-1.07T [127]	
	$L_{Fe,Mn:Va}=-5748+3.87T+273(y'_{Fe}-y'_{Mn})$	[88]
	$L_{Fe,C:Va}=-17335$	[88]
	$L_{Mn,C:Va}=-2092-3.14T-5230(y''_C-y''_{Va})$	[125]
	$L_{Fe,Mn:C}=18828-47.36T-33472(y'_{Fe}-y'_{Mn})$	[3]
M ₃ C (Fe,Mn) ₃ (C) ₁	$G_{Fe:C}=GCEMFE$ [128], $G_{Mn:C}=3$ GHSEMN+GHSECCF-32000-4.1T [125]	
	$L_{Fe,Mn:C}=-3347.2-2510.4(y'_{Fe}-y'_{Mn})$	[3]
M ₅ C ₂ (Fe,Mn) ₅ (C) ₂	$G_{Fe:C}=\frac{5}{3}GCEMFE+\frac{1}{3}GHSECC+14100-7.35T$ [3]	
	$G_{Mn:C}=5$ GHSEMN+2 GHSECC-62302-5T [125]	
	$L_{Fe,Mn:C}=-5020.8$	[3]
M ₇ C ₃ (Fe,Mn) ₇ (C) ₃	$G_{Fe:C}=\frac{7}{3}GCEMFE+\frac{2}{3}GHSECC+30000-15.45T$ [3]	
	$G_{Mn:C}=7$ GHSEMN+3 GHSECC-62302-5T [125]	
	$L_{Fe,Mn:C}=-7893.53+6.46T$	[3]
M ₂₃ C ₆ (Fe,Mn) ₂₀ (Fe,Mn) ₃ (C) ₆	$G_{Fe:Fe:C}=\frac{23}{3}GCEMFE-\frac{5}{3}GHSECC+15000$ [3]	
	$G_{Mn:Mn:C}=23GHSEMN+6GHSECC-245501-2.44T$ [125]	
	$L_{Fe,Mn:C}=-79496$	[3]

ϑ: optimized model parameter by author

Table A-3: thermodynamic model parameters for the system Fe-Mn-S

Phase (model)	Model parameter [J]	Publication
	$Z_{FeFe}^{Fe} = Z_{FeMn}^{Fe} = Z_{MnMn}^{Mn} = Z_{MnFe}^{Mn} = Z_{SS}^S = 6$	[2]
	$Z_{FeS}^{Fe} = Z_{SFe}^S = Z_{MnS}^{Mn} = Z_{SMn}^S = 2$	
Liquid (Fe,Mn,S)	$\Delta g_{FeS} = -104888.1 + 0.338T + (35043.32 - 9.88T)X_{FeFe} + 23972.27X_{FeFe}^2 + 30436.82X_{FeFe}^3$ $+ 8626.26X_{SS} + (72954.29 - 26.178T)X_{SS}^2 + 25106X_{SS}^3$	[6]
	$\Delta g_{FeMn} = -1380.72 + 0.134T + 753.62X_{FeFe} - 586.15X_{MnMn}$	9
	$\Delta g_{MnS} = -236396 + 16.744T + (78322 - 12.552T)X_{MnMn} + 16736X_{MnMn}^2 + 31380X_{SS}^2$	[2]
	$\Delta g_{Fe,S(Mn)} = 10460$	[2]
FCC (Fe,Mn,S) ₁ (Va) ₁	$G_{Fe:Va} = GFCCFE, G_{Mn:Va} = GFCCMN, G_{S:Va} = GHSERSS + 66082.63 + 9.6095T$ [6], $L_{Fe,S:Va} = -59070.736 - 34.612T$ $L_{Fe,Mn:Va} = -5020.8 + 1.883T$ $T_{cFe:Va} = -201, T_{cMn:Va} = -1620, \beta_{Fe:Va} = -2.1, \beta_{Mn:Va} = -1.86$ $T_{cFe,Mn:Va} = -2282 - 2068(y'_{Fe} - y'_{Mn})$	[6] 9 [85]
BCC (Fe,Mn,S) ₁ (Va) ₃	$G_{Fe:Va} = GHSEFFE, G_{Mn:Va} = GBCCMN, G_{S:Va} = GHSERSS + 24954.78 - 14.3233T$ [6], $L_{Fe,S:Va} = -31041.003 - 10.66T$ $L_{Fe,Mn:Va} = -4184 - 1.715T$ $T_{cFe:Va} = 1043, T_{cMn:Va} = -580, \beta_{Fe:Va} = 2.22, \beta_{Mn:Va} = -0.27$ $T_{cFe,Mn:Va} = 123$	[6] 9 [85]
(Fe,Mn)S	$G_{FeS}^0 = -626769.18 + 14055.83T - 2437.14 \ln T + 4.951T^2 - 0.001928T^3 + 20561935T^{-1}; (298.15 < T < 420 \text{ K})$ [6]	
(Fe,Va,Mn) [S]	$G_{FeS}^0 = -118134.699 + 342.176T - 60 \ln T; (420 < T < 3000 \text{ K})$ [6] $G_{MnS}^0 = -227939.7765 + 241.372 - 47.698 \ln T - 0.003766T^2; (T < 1928 \text{ K})$ [2]	
	$L_{Fe,S:Va} = -225830.67 + 26.359T$	[6]
(Mn,Fe)S	$G_{FeS}^0 = -626769.18 + 14055.83T - 2437.14 \ln T + 4.951T^2 - 0.001928T^3 + 20561935T^{-1}; (298.15 < T < 420 \text{ K})$ [6]	
(Mn,Fe) [S]	$G_{FeS}^0 = -118134.699 + 342.176T - 60 \ln T; (420 < T < 3000 \text{ K})$ [6] $G_{MnS}^0 = -227939.7765 + 241.372 - 47.698 \ln T - 0.003766T^2; (T < 1928 \text{ K})$ [2]	
	$L_{Fe,Mn:S,Va} = 7531.2 - 0.4184T$	[2]

9: optimized model parameter by author

Table A-4: thermodynamic model parameters for the systems Fe-C-S and S-C

Phase (model)	Model parameter [J]	Publication
Liquid (Fe,C,S)	$Z_{\text{FeFe}}^{\text{Fe}} = Z_{\text{CC}}^{\text{C}} = Z_{\text{SS}}^{\text{S}} = Z_{\text{FeC}}^{\text{C}} = Z_{\text{CS}}^{\text{C}} = Z_{\text{CS}}^{\text{S}} = 6$	[4]
	$Z_{\text{FeC}}^{\text{Fe}} = 3$	
	$Z_{\text{FeS}}^{\text{S}} = Z_{\text{FeS}}^{\text{Fe}} = 2$	
FCC (S,Va) ₁ (C,Va) ₁	$L_{\text{FeCS}} = -167360X_{\text{S}} + 167360X_{\text{Fe}} + 209200X_{\text{C}}$	[4]
	Bragg-Williams model [103]	
	"Toop-like" interpolation with Fe as the asymmetric component	
BCC (S,Va) ₁ (C,Va) ₃	$G_{\text{S:C}} = \text{GHSERSS} + \text{GHSERCC}$	[4]
	$G_{\text{S:C}} = \text{GHSERSS} + 3 \text{GHSERCC}$	[4]

Curriculum Vitae

† Robert Littringer

* February 10th, 1997



Education

Montanuniversitaet Leoben (Austria) Master program – Ferrous Metallurgy and Metal Forming	07/2022 – 03/2024
Pohang University of Science and Technology (Republic of Korea) Exchange graduate student – Ferrous Metallurgy	08/2023 – 12/2023
Montanuniversitaet Leoben (Austria) Bachelor program – Metallurgy	10/2016 – 07/2023
BRG/BORG Schloss Traunsee (Austria) High School Diploma	09/2007 – 06/2015

Internships and job experiences

Chair of Ferrous Metallurgy, Montanuniversitaet Leoben (Austria) Scientific Student Staff (Metallographic laboratory)	10/2022 – 06/2023 10/2021 – 06/2022 09/2020 – 06/2021
voestalpine Stahl Donawitz GmbH (Austria) Production Internship (Blast furnace)	07/2022 – 09/2022 08/2021 – 09/2021
Primetals Technologies Austria GmbH (Austria) Internship Research and Development (Continuous Casting Machine)	07/2021 08/2019

Memberships and social commitment

Student's Union of Montanuniversitaet Leoben Student representative (study program Metallurgy)	07/2021 – 06/2023
University Senate of Montanuniversitaet Leoben Vice-Chairman	09/2018 – 06/2022
Student's Union of Montanuniversitaet Leoben Chairman	09/2018 – 09/2020